



ulm university universität
uulm



Annual Report 2009

Institute of Optoelectronics

Cover photo:

Arrays of vertical-cavity surface-emitting lasers with integrated surface reliefs for transverse mode control. The devices are employed for microparticle manipulation (related to the article on p. 35).

Contents

Articles

Frequency-Doubled Semiconductor Disk Lasers for Blue Watt-Level Emission . . .	3
Advanced Strain Compensation in MBE-Grown Semiconductor Disk Lasers . . .	11
Design of a Short Integrated VECSEL Resonator	17
High-Order-Mode VCSEL With 12 mW Output Power	21
VCSEL/PIN PD Transceiver Chips	27
Heat-Sink Modules: Performance Enhancement for VCSEL Chips	35
CW Characteristics of MEMS Atomic Clock VCSELs	41
Self Separation Process for Full 2"-GaN Wafers in HVPE	47
HVPE a-plane GaN on Misoriented Substrates	55
Inverse GaInN/GaN Pyramid LED	63
Sample Support Development for In-Situ Ultra-HRTEM Electrical Investigations	71
Coaxial GaN/InGaN/GaN Nano-Heterostructures	77
Processing of Semipolar and Nonpolar InGaN-Based Laser Diodes	85
Growth of High Quality AlGaIn Using In-Situ Deposited SiN	91

Lists of Publications

Ph.D. Theses	101
Diploma and Master Theses	102
Semester Projects	103
Talks	104
Publications and Conference Contributions	110





- | | | |
|---------------------|---------------------------|---------------------------|
| 1: Frank Lipski | 9: Frank Demaria | 17: Rainer Michalzik |
| 2: Mohamed Fikry | 10: Wolfgang Schwarz | 18: Stephan Schwaiger |
| 3: Peter Unger | 11: Alexander Kern | 19: Ahmed Al-Samaneh |
| 4: Ferdinand Scholz | 12: Abdel-Sattar Gadallah | 20: Eva Schmid |
| 5: Gerlinde Meixner | 13: Fernando Rinaldi | 21: Benedikt Westenfelder |
| 6: Josef Theisz | 14: Ihab Kardosh | 22: Dietmar Wahl |
| 7: Thomas Wunderer | 15: Rainer Blood | 23: Kamran Forghani |
| 8: Ilona Argut | 16: Jürgen Mähnß | 24: Robert Leute |

Missing in the picture:

Anna Bergmann, Christine Bunk, Karl Joachim Ebeling, Sükran Kilic,
Hildegard Mack, Susanne Menzel, Rudolf Rösch

Ulm University Institute of Optoelectronics

Albert-Einstein-Allee 45, 89081 Ulm, Germany
 URL: <http://www.uni-ulm.de/opto>
 Fax: +49-731/50-260 49
 Phone: +49-731/50-

Head of Institute

Prof. Dr. Peter Unger -2 60 54 peter.unger@uni-ulm.de

Deputy Head

Prof. Dr. Ferdinand Scholz -2 60 52 ferdinand.scholz@uni-ulm.de

President of Ulm University

Prof. Dr. Karl Joachim Ebeling -2 60 51 karl.ebeling@uni-ulm.de

Senior Research Assistant

PD Dr.-Ing. Rainer Michalzik -2 60 48 rainer.michalzik@uni-ulm.de

Cleanroom Management

Dr.-Ing. Jürgen Mähnsß -2 60 53 juergen.maehnss@uni-ulm.de

Secretaries

Christine Bunk -2 60 50 christine.bunk@uni-ulm.de

Sükran Kilic -2 60 59 suekran.kilic@uni-ulm.de

Hildegard Mack -2 60 60 hildegard.mack@uni-ulm.de

Eva Schmid -2 60 50 eva.schmid@uni-ulm.de

Research Staff

M.Sc. Ahmed Al-Samaneh -2 60 37 ahmed.al-samaneh@uni-ulm.de

Dipl.-Ing. Anna Bergmann -2 60 38 anna.bergmann@uni-ulm.de

Dr.-Ing. Frank Demaria -2 60 46 frank.demaria@uni-ulm.de

M.Sc. Mohamed Fikry -2 61 95 mohamed.fikry@uni-ulm.de

M.Sc. Kamran Forghani -2 60 39 kamran.forghani@uni-ulm.de

M.Sc. Abdel-Sattar Gadallah* -2 60 36 abdel-sattar.gadallah@uni-ulm.de

Dipl.-Ing. Ihab Kardosh -2 60 35 ihab.kardosh@uni-ulm.de

Dipl.-Ing. Alexander Kern -2 60 37 alexander.kern@uni-ulm.de

Dipl.-Phys. Robert Leute -2 60 56 robert.leute@uni-ulm.de

Dipl.-Phys. Frank Lipski -2 60 39 frank.lipski@uni-ulm.de

Dr.-Ing. Fernando Rinaldi -2 60 46 fernando.rinaldi@uni-ulm.de

Dipl.-Phys. Stephan Schwaiger -2 60 56 stephan.schwaiger@uni-ulm.de

Dipl.-Ing. Wolfgang Schwarz -2 60 38 wolfgang.schwarz@uni-ulm.de

Dipl.-Ing. Sarad Bahadur Thapa* -2 61 95 sarad.thapa@uni-ulm.de

Dipl.-Phys. Dietmar Wahl -2 60 37 dietmar.wahl@uni-ulm.de

Dipl.-Phys. Benedikt Westenfelder -2 64 54 benedikt.westenfelder@uni-ulm.de

Dipl.-Ing. Thomas Wunderer -2 64 54 thomas.wunderer@uni-ulm.de

Technical Staff

Ilona Argut	-2 60 56	<code>ilona.argut@uni-ulm.de</code>
Rainer Blood	-2 60 44	<code>rainer.blood@uni-ulm.de</code>
Gerlinde Meixner	-2 60 41	<code>gerlinde.meixner@uni-ulm.de</code>
Susanne Menzel	-2 60 41	<code>susanne.menzel@uni-ulm.de</code>
Rudolf Rösch	-2 60 57	<code>rudolf.roesch@uni-ulm.de</code>
Josef Theisz	-2 60 30	<code>josef.theisz@uni-ulm.de</code>

* Member has left the institute meanwhile

Preface

The year 2009 was another successful one for the Institute of Optoelectronics. Research concentrated on vertical-cavity surface-emitting lasers (VCSELs), optical interconnect systems, GaN-based electronic and optoelectronic devices, and semiconductor disk lasers.

The VCSELs and Optical Interconnects Group has focused its efforts on the fabrication and analysis of GaAs-based specialty VCSELs emitting higher-order transverse modes, the design of bidirectional transceiver chips integrating a VCSEL and a PIN-type photodiode, the optimization of polarization-stable surface grating VCSELs for atomic clock applications, and the demonstration of VCSEL-based sensing and particle manipulation in microfluidic chips.

Besides other ongoing activities, the GaN Group continued to concentrate on studies of non- and semipolar structures for highly efficient longer wavelength light emitters. The cooperation in our respective transregional research group “PolarCoN” could be further enhanced. In the frame of these activities, we have organized a summer school in September where more than 50 scientists from the research group and from other renowned institutions world-wide enjoyed the great hospitality of the scientific center “Schloss Reisingen” for fruitful scientific discussions. With the participation in the DFG project SALVE (“Sub Angstrom Low Voltage Electron Microscopy”) led by the TEM group of Ulm University, we have set a first step in the field of graphene research.

In the High-Power Semiconductor Laser Group, an optically-pumped semiconductor disk laser with intracavity second-harmonic generation in a novel folded-cavity resonator configuration has been realized, emitting 1.6 W of continuous output power at a wavelength of 460 nm. The incident pump power was 11 W at a wavelength of 808 nm, which results in a record overall power conversion efficiency of 14.5%.

In Feb. 2009, Anna Bergmann’s Diploma Thesis on VCSEL-integrated optical trapping modules was awarded by the VDE. Johannes Michael Ostermann received the Dulger Prize 2009 of the Heidelberger Akademie der Wissenschaften for his work on polarization-stable VCSELs.

On November 14, the Institute of Optoelectronics celebrated its 20-year anniversary. All 120 alumni of the Institute were invited to an anniversary celebration party and 67 of them came to Ulm, some with spouses and children. Another highlight of last year’s activities was the 14th European Workshop on MOVPE organized by our Institute in June, where more than 200 scientists presented and discussed their brand-new results, excellently hosted by the Edwin-Scharff Congress Center Neu-Ulm.

Rainer Michalzik
Ferdinand Scholz
Peter Unger

Ulm, March 2010

Intra-Cavity Second-Harmonic Generation of Blue 460 nm Watt-Level Emission from Optically Pumped Semiconductor Disk Lasers

Frank Demaria and Alexander Hein

Experimental results with second-harmonic 460 nm-wavelength emission are presented. A profound analytical description of the intra-cavity beam shaping properties of the resonator based on the ABCD-law provides an effective design tool for the construction of appropriate resonator setups. Also described is the layer design of the optically pumped laser chip in which the fundamental radiation is generated. Overall conversion efficiencies up to 14.5 % and a maximum power of 1.6 W are demonstrated.

1. Introduction

High performance laser display applications require blue color light sources with a wavelength of 450–460 nm. Moreover, for this wavelengths a satisfying illuminance of reasonable large areas can only be provided by lasers with at least several hundred milliwatts of optical output power. Although laser diodes based on gallium nitride which are operating at wavelengths around 405 nm are suitable and frequently used laser sources for optical data storage, it still appears uncertain whether this approach leads to optical displays with the desired qualities. Here an alternative approach is described. The experimental results which are acquired by optically pumped semiconductor disk lasers in combination with intra-cavity second-harmonic-generation meet the mentioned demands.

2. Experimental Setup

Figure 1 shows a standard folded-cavity configuration which is commonly used for intra-cavity second-harmonic-generation (SHG) [1, 2]. In order to prevent absorption of the second harmonic in the semiconductor material, the critically phase-matched nonlinear crystal is localized in the outer resonator arm opposite to the laser chip. A 5 mm-long $3 \times 3 \text{ mm}^2$ cross-section bismuth borate crystal (BiB_3O_3 , BiBo) is used. The folding mirror and the external end mirror are designed to provide maximum reflectivity for the 920 nm fundamental radiation, but much lower reflectivity for the second harmonic with 460 nm wavelength. Wavelength stabilization, narrowing and tuning is realized by a 2 mm-thick birefringent quartz plate which is inserted under Brewster angle [3, 4]. The laser chip is mounted on a copper heat sink whose temperature is stabilized at a value of 0°C by a Peltier cooler. Pump radiation from a fiber-coupled diode-laser is irradiated under an inclination angle of 30° with respect to the surface normal and focused to a spot-size of approximately $310 \mu\text{m} \times 270 \mu\text{m}$. The pump wavelength varies from 801 nm at threshold to 803 nm at the maximum pump power.

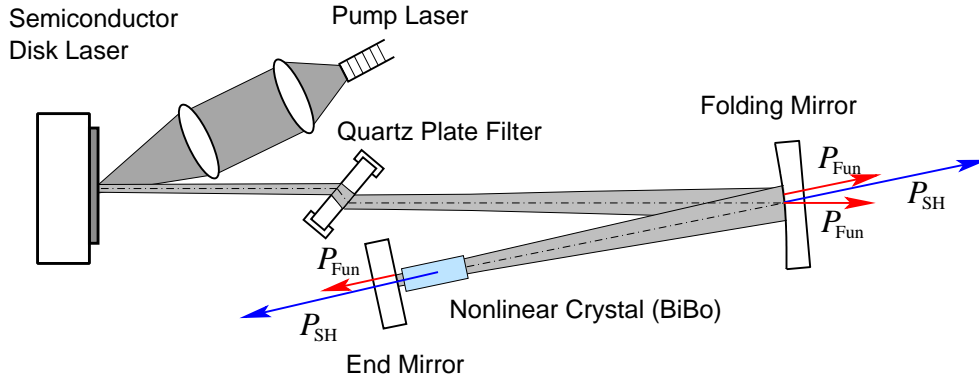


Fig. 1: Setup for second harmonic generation in a folded cavity configuration.

2.1 Analysis of beam and resonator

The design of a stable and effective resonator configuration is a challenging task. To provide high fundamental laser radiation, the laser chip has to be excited within a reasonable large area with diameters of several hundred micrometers. This defines the beam diameter of the laser mode at that position. On the other hand, the beam diameter in the outer resonator arm, where the nonlinear crystal is inserted, should be much smaller to achieve effective SHG. The distances between the mirrors should not be too big in order to get an applicable and compact laser source with low aperture losses. Too small distances are also not desired in an easy to handle experimental setup with macroscopic components. Fortunately, with only few simplifying assumptions, a profound and clear analytical description of the resonator's beam shaping properties becomes possible. The influence of the laser chip on the beam propagation is neglected as well as the SHG crystal and the quartz-plate filter. According to fig. 2, the resonator's geometry can be described

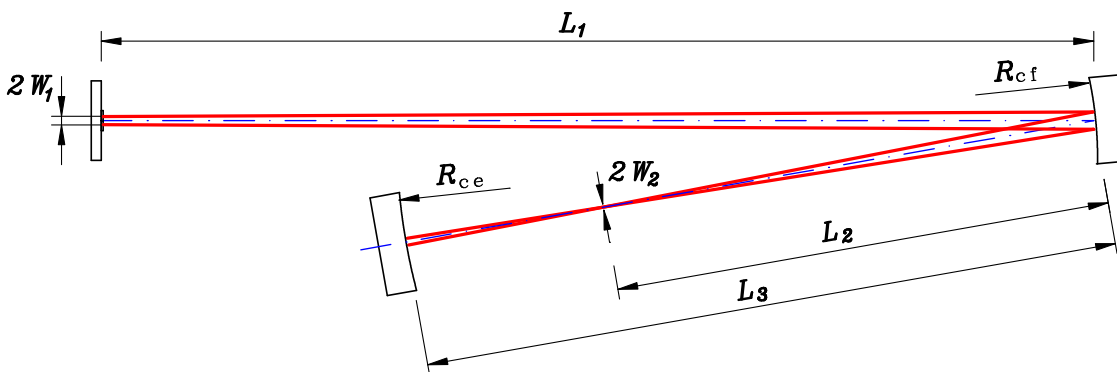


Fig. 2: Simplified geometry and parameters of the single-folded optical resonator setup with curved external mirrors.

by the distances L_1 , L_3 and the radii of curvature R_{cf} , R_{ce} of the folding mirror and the end mirror. These parameters alone determine whether the resonator is stable or unstable. The approach for the theoretical description is the following. For a nondiffraction-limited optical beam, which is made up by a superposition of Laguerre–Gauss resonator modes, an effective radius of curvature of the phase fronts can be defined [7]. Stability of a lin-

ear resonator requires that the beam's effective radius of curvature at the end mirrors is identical with the radius of curvature of the end mirrors. One of them is the rear reflector of the laser chip. It is supposed to be plane. Thus, it is obvious that a beam waist is established inside the laser chip at the position of the rear reflector. Its diameter is assumed as $2W_1$. The second end mirror is the external end mirror which is realized by a multi-layer dielectrically-coated 0.5 inch-diameter glass substrate. The folding mirror is made up the same. For the shown configuration with a concave external end mirror, an external beam waist with the diameter $2W_2$ is located inside the outer resonator arm at a distance L_2 from the folding mirror. If a plane end mirror is used, the external beam waist is located at the surface of this mirror and L_3 becomes identical with L_2 .

Paraxial ray analysis allows the simple description of the focussing characteristic of the mirrors by the focal length $f = R_c/2$ and the ray transfer matrix formalism [8]. Finally, the resonator's characteristic $ABCD$ -matrix, given by the product of its single elementary transfer matrices has to be applied to the $ABCD$ -law in order to derive analytical formula within the parametric description of Gaussian beams. The generalization to nondiffraction-limited beams with the wavelength λ and the beam waist radius W is implemented by the diffraction number M^2 and the definition of the Rayleigh range as

$$z_R = \frac{\pi W^2}{M^2 \lambda} \quad (1)$$

[9]. Different Rayleigh ranges for the two resonator arms have to be considered. The Rayleigh ranges and beam waist positions are unambiguously determined by the resonators geometry. For a resonator with plane end mirrors ($L_2 = L_3$) and a folding mirror with a focal length $f_f = R_{cf}/2$ the spot-size reduction ratio

$$V = \frac{W_1}{W_2} \quad (2)$$

is given by

$$V = \sqrt{\frac{L_1 - f_f}{L_2 - f_f}} \quad (3)$$

and the chip-sided Rayleigh range by

$$z_{R1} = V \sqrt{f_f^2 - (L_1 - f_f)(L_2 - f_f)}. \quad (4)$$

For the more general case of a concave external end mirror with $f_e = R_{ce}/2$, the expression

$$z_{R1}^2 = [f_f^2 - (L_1 - f_f)(L_3 - f_f)] \frac{2f_e(L_1 - f_f) + f_f^2 - (L_1 - f_f)(L_3 - f_f)}{2f_e(L_3 - f_f) - (L_3 - f_f)^2} \quad (5)$$

can be derived for the Rayleigh range [10]. In this case, the distance of the external beam waist from the folding mirror is determined by

$$L_2 = f_f \frac{z_{R1}^2 + L_1(L_1 - f_f)}{z_{R1}^2 + (L_1 - f_f)^2} \quad (6)$$

and the spot-size reduction ratio can be calculated by expression (3) which is valid also for this case. Unlike the Rayleigh ranges and the spot sizes of the ideal Gaussian beam ($M^2 = 1$), the beam waists of the real beam with $M^2 > 1$ are underdetermined according to (1). Actually, it can be observed that the value of M^2 strongly depends on the spot-size of the pump beam on the laser chip for a given resonator configuration. That way an optimization of the overlap of the lateral beam intensity and the gain distribution of the laser chip takes place. The spot-size of the resulting beam is at any position M times larger than the embedded fundamental Gaussian mode which is generated by the same resonator. However, one restriction has to be considered. The beam waist diameters of the laser mode fit the size of the pumped area as long as they are significantly larger than the fundamental mode.

Best experimental results, concerning SHG output powers, have been achieved with a folding mirror with $R_{cf} = 50$ mm radius of curvature and an end mirror with $R_{ce} = 1000$ mm, the latter could have been replaced by a plane mirror in principle. For each sample L_1 and L_3 have been adjusted to achieve maximum SHG output powers within the ranges 85–93 mm and 33–38 mm. The calculated parameters of the laser mode for such configurations can be taken from Fig. 3. The solid lines in the upper diagram show the mode diameters of the fundamental Gaussian mode on the laser chip. A pump-spot diameter with the same value leads to nearly fundamental mode operation. A larger pump spot leads to higher order modes which result in a larger effective diameter $2W_1$ of the laser mode and a higher M^2 value, which is illustrated as an example by the dashed line for $M^2 = 1.8$. The correlated external beam-waist diameter $2W_2$ and the reduction ratio V can be taken from the diagrams below. The bottom diagram shows the distance of the external beam-waist position from the end mirror which is negligible because of the high value of R_{ce} . Before the SHG-crystal is inserted, the resonator was adjusted to achieve stable and efficient fundamental laser operation. In this state, experimental investigations in which the diffraction number of the emitted beam is measured by a beam analyzer show very good agreement with theory. After the 5 mm long crystal is inserted, the external mirror has to be moved approximately 2 mm to enlarge the value of L_3 . The enlargement is related to a shift of the (virtual) beam waist position. It can be quantified in a more detailed theoretical description that considers the length of the crystal and its effective refractive index. The same applies to L_1 and the birefringent filter.

2.2 Layer design of the disk laser chips

If the resonator is the framework of the laser setup, then the disk laser chip should be considered as the key component. Chips with different characteristic features have been investigated. All structures are realized with a carefully elaborated layer design to provide high efficiencies and high optical output powers [5, 6].

Figure 4 shows a graphical representation of the top region of the investigated structure #1 with 6 single quantum wells. Its composition consists of a dielectric surface layer, a resonant periodic gain structure and the rear double-band Bragg reflector (DBBR). The DBBR is designed to provide high reflectivity not only for the fundamental lasing wavelength but also for the incident pump light. Thus, it has to be considered that the

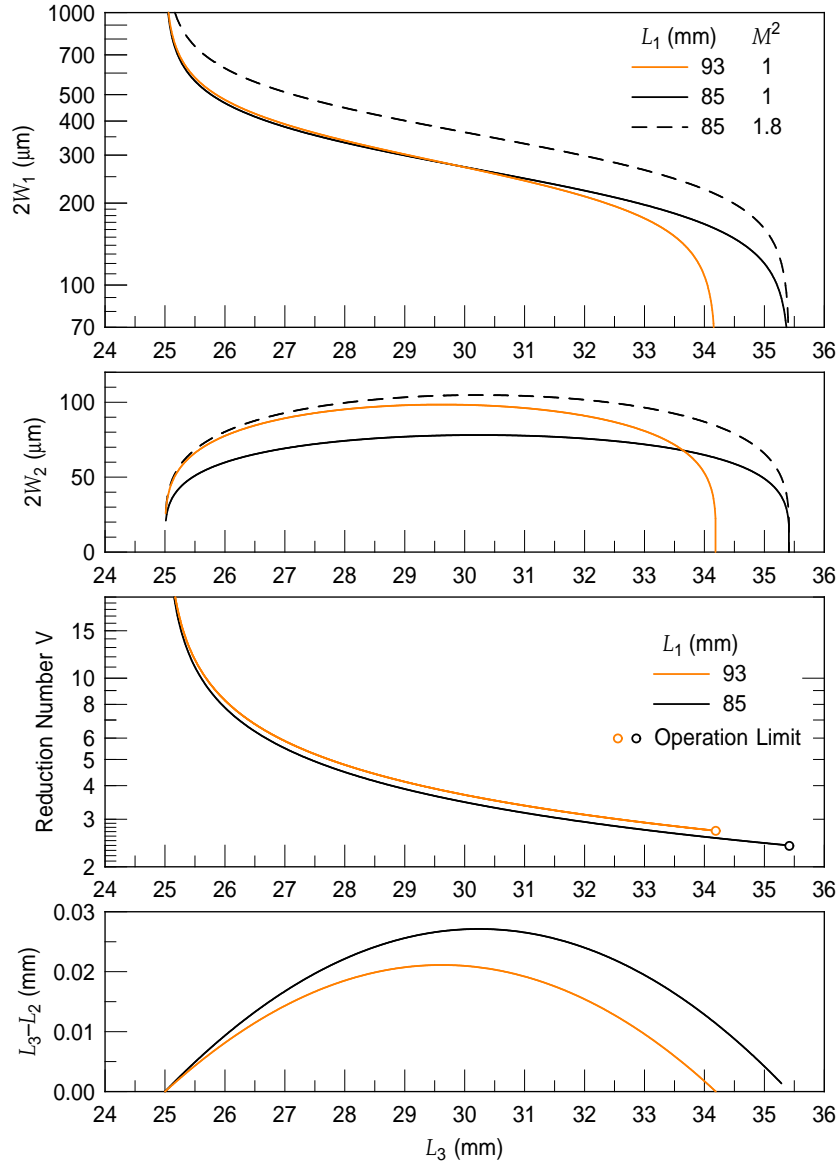


Fig. 3: Calculated relations of the resonator's geometrical parameters for a folding mirror with $R_{cf} = 50$ mm and an end mirror with $R_{ce} = 1000$ mm. From top to bottom: laser-mode spot size on the chip, spot size of the external focus, spot-size reduction ratio, distance of external focus from the end mirror.

longitudinal field distribution of the pump light inside the structure is much more dominated by a standing wave than by an exponential decrease that results from absorption. The 84 nm-thick TiO_2 surface layer with a refractive index of 2.381 for the pump wavelength is designed to lower the surface reflectivity to a value of 5.4% for an unpolarized beam which is irradiated under 30° . That way, maximum absorbance values around 95% can be achieved. Furthermore, the contrast of the refractive indexes is much higher at the interface to air than at the interface to the semiconductor layers. Therefore a maximum of the resonant pump field is located at this position and a minimum nearby the interface to the semiconductor structure inside the absorbing 5 nm-thick GaAs anti-oxidation

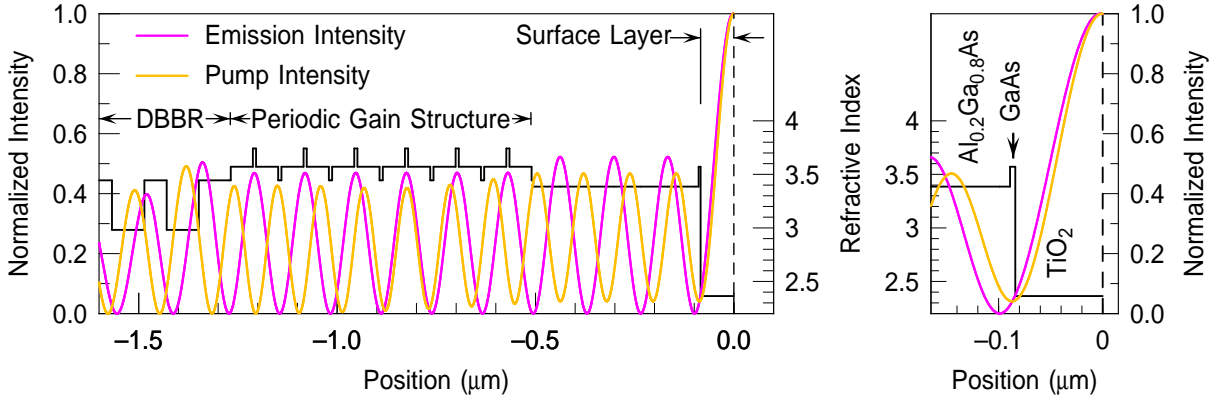


Fig. 4: Top region of structure #1, visualized by the index of refraction, beginning from the surface layer to the first layers of the DBBR (left). Also shown are both calculated electric field intensities for the emission wavelength $\lambda_e = 920$ nm and the pump wavelength $\lambda_e = 803$ nm with an angle of incidence $\theta_i = 30^\circ$. In detail shown is the junction between the dielectric surface layer and the underlying semiconductor layers where nodes of the electric field intensities are located (right).

layer. This layer is necessary to protect the underlying aluminum containing material during the fabrication process. The gain structure is formed by a periodic sequence of several 8 nm-thick $\text{In}_{0.08}\text{Ga}_{0.92}\text{As}$ quantum wells which are surrounded by GaAs barriers. Number and type of the quantum wells of the different samples are given in table 1. The

Table 1: Characteristical features of the laser-chip samples.

Sample	Quantum wells	Distance from wafer center
#1a	6 single	8 mm
#1b	6 single	8.5 mm
#2	8 double	2 mm

periods of quantum wells with their surrounding barriers are separated by $\text{GaAs}_{0.71}\text{P}_{0.29}$ strain compensation layers [3,11] which also act as a carrier diffusion barrier. The double quantum wells of structure #2 contain a 10 nm-thick intermediate GaAs barrier.

3. Second-Harmonic Output Characteristics

Figure 5 shows an overview of the output characteristics for three laser chips with the best performance. The output powers were limited by the cooling capacity of the Peltier thermoelectric device that was used for temperature stabilization. For all measurements, the orientation of the critical phase matched crystal was adjusted for maximum output power at the highest pump power. The best performance is achieved with sample #1a, a structure with 6 single quantum wells. At an incident pump radiation of 11 W a SHG output power of 1.6 W is measured which results in an overall conversion efficiency of

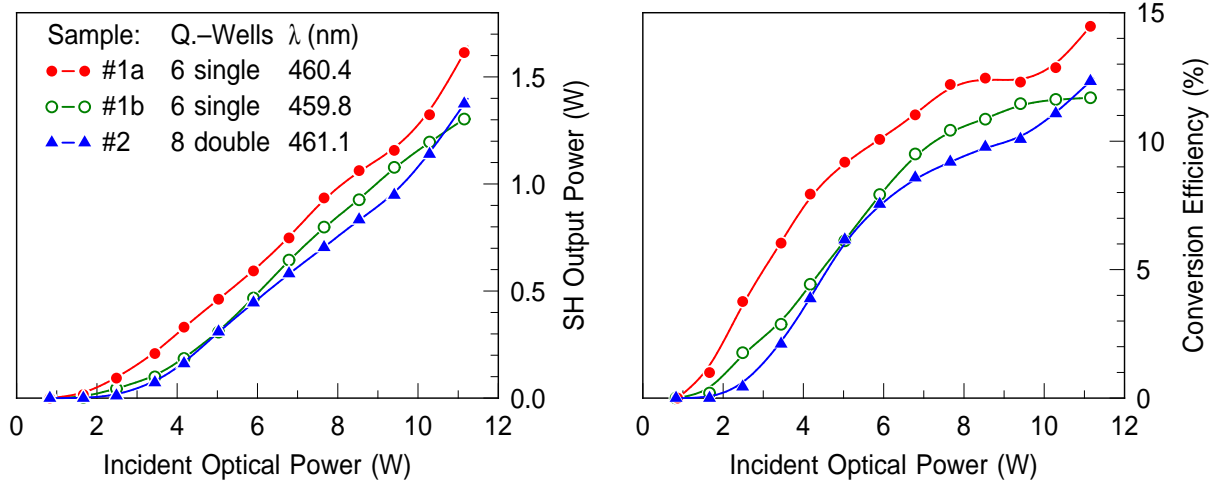


Fig. 5: Second harmonic output power characteristics (left) and the corresponding overall conversion efficiency (right).

14.5%. The fundamental radiation was filtered out with an optical band-edge filter. A 10 dB spectral linewidth of about 2.6 nm is typically observed as shown in the spectrum in fig. 6.

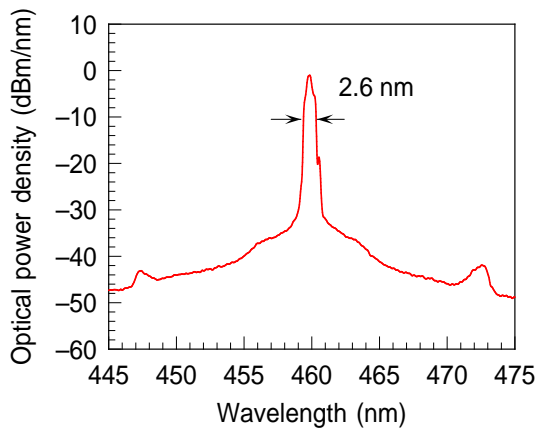


Fig. 6: Typical spectrum of the second harmonic taken from sample #1b. The linewidth at the 10 dB drop is 2.6 nm.

4. Conclusion and Outlook

The described combination of an optically pumped semiconductor disk laser with a nonlinear crystal in a folded resonator may appear complex and extensive. It has been demonstrated however, that the utilization of properly designed and fabricated laser chips in an adequate resonator configuration leads to a blue laser source with unique properties. The given analytical equations which realistically describe the beam shaping properties of the resonator are quite useful for the dimensioning of stable resonator configurations for efficient intra-cavity second-harmonic-generation. The maximum output power was limited by thermal roll over arising from insufficient heat removal. Only simple copper heat spreaders and customized peltier coolers have been utilized for the experiments. Because

of its nonlinear nature, the generation of the second harmonic becomes more efficient with increasing intensity of the fundamental radiation. It seems that the utilization of diamond heat spreaders with much better thermal conductivity and Peltier devices with higher cooling capacity can lead to even brighter, multi-watt level laser sources.

References

- [1] M. Fallahi, L. Fan, Y. Kaneda, C. Hassenius, J. Hader, H. Li, J. Moloney, B. Kunert, W. Stolz, S. Koch, J. Murray, and R. Bedford, "5-W yellow laser by intracavity frequency doubling of high-power vertical-external-cavity surface-emitting laser", *IEEE Photon. Technol. Lett.*, vol. 20, no. 20, pp. 1700–1702, 2008.
- [2] J.Y. Kim, S. Cho, S.-J. Lim, J. Yoo, G.B. Kim, K.-S. Kim, J. Lee, S.-M Lee, T. Kim, and Y. Park, "Efficient blue lasers based on gain structure optimizing of vertical-external-cavity surface-emitting laser with second harmonic generation", *J. Appl. Phys.*, vol. 101, no. 3, pp. 033103-1–4, 2007.
- [3] J.W. Evans, "The birefringent filter", *J. Opt. Soc. Am.*, vol. 39, no. 3, p. 229, 1949.
- [4] M. Jacquemet, M. Domenech, G. Lucas-Leclin, P. Georges, J. Dion, M. Strassner, I. Sagnes, and A. Garnache, "Single-frequency cw vertical external cavity surface emitting semiconductor laser at 1003 nm and 501 nm by intracavity frequency doubling", *Appl. Phys. B*, vol. 86, pp. 503–510, 2007.
- [5] F. Demaria, S. Lorch, S. Menzel, M. C. Riedl, F. Rinaldi, R. Rösch, and P. Unger, "Design of highly efficient high-power optically pumped semiconductor disk lasers", *IEEE J. Select. Topics Quantum Electron.*, vol. 15, no. 3, pp. 973–977, 2009.
- [6] F. Demaria, "Layer Design of Highly Efficient Optically Pumped Semiconductor Disk Lasers", *Annual Report 2008*, pp. 41–48. Ulm University, Institute of Optoelectronics.
- [7] A. E. Siegman, "Defining the Effective Radius of Curvature for a Nonideal Optical Beam", *IEEE J. Quantum Electron.*, vol. 27, no. 5, pp. 1146–1148, 1991.
- [8] H. Kogelnik and T. Li, "Laser beams and resonators", *Appl. Opt.*, vol. 5, no. 10, pp. 1550–1567, 1966.
- [9] P. A. Bélanger, "Beam propagation and the ABCD ray matrices", *Opt. Lett.*, vol. 16, no. 14, pp. 196–198, 1991.
- [10] F. Demaria, *Schicht und Resonatordesign von Halbleiterscheibenlasern*. Ph.D. thesis, Ulm University, Ulm, Germany, 2008.
- [11] F. Rinaldi, "Advanced Strain Compensation in MBE Grown Semiconductor Disk Lasers", *Annual Report 2009*, pp. 11–15. Ulm University, Institute of Optoelectronics.
- [12] F. Rinaldi, *MBE Growth and Characterization of Multilayer Structures for Vertically Emitting Laser Devices*. Ph.D. thesis, URL: <http://vts.uni-ulm.de/doc.asp?id=6667>, Ulm University, Ulm, 2008.

Advanced Strain Compensation in MBE-Grown Semiconductor Disk Lasers

Fernando Rinaldi and Susanne Menzel

Strain compensation in disk lasers is described in detail in this article. The analyzed structures are pseudomorphically grown by MBE (molecular beam epitaxy) on GaAs substrates and are designed for an emission wavelength of 920 nm. It is shown that strain compensation is needed to produce reliable laser devices and two different strain compensation strategies are compared.

1. Introduction

Nowadays semiconductor disk lasers are of great importance in virtue of their high output power. In fact, it is common to fabricate devices having an output power of several watts [1, 2]. Furthermore, the free access of the resonator allows intracavity SHG (second harmonic generation) using nonlinear crystals. In this way, the range of emission wavelengths that can be realized using different compound semiconductors is furthermore expanded.

It is clear that such high emission power stretches the semiconductor material close to its stability limit, and different techniques should be used to improve the device performances. One of this methods is the strain compensation, that allows to grow complex disk laser structures that are able to achieve higher output power without showing any degradation.

2. Typical Disk Laser Structures

The structure of the considered disk lasers is basically composed of two parts. The first part is the DBR (distributed Bragg reflector), which is made of an alternating sequence of AlAs/Al_{0.20}Ga_{0.80}As layers, these two materials have the highest refractive index contrast that guarantees no fundamental absorption for the 808 nm pump light. The second part is the active region, which consists of multiple In_{0.08}Ga_{0.92}As/GaAs QWs (quantum wells) separated by GaAs and Al_{0.20}Ga_{0.80}As layers with the respective functions of absorbing the pump light radiation and providing carrier confinement. In order to improve this absorption, a special layer design consisting of a double periodic sequence of layers is employed. In this case the reflectivity spectrum of the resulting DBR exhibits two stop bands, one is used for the emission wavelength, the second one for the pump light.

The MBE pseudomorphic growth of the multilayers, performed on GaAs (001) substrates starts with the active region, and is followed by the DBBR (double band Bragg reflector). This structure is then mounted, in reversed order, on a heat sink and then the substrate is chemically removed. More details about the design, processing, and characterization of the resulting disk laser chips can be found in [2, 3].

3. Disk Laser Strain Compensation

Four samples (*a, b, c, and d*) are considered in the following sections. The described structures are compressively strained because not only the $\text{In}_{0.08}\text{Ga}_{0.92}\text{As}$ alloy of the 8 nm thick QWs exhibits an in-plane strain ϵ of -0.57% , but also the almost unstrained AlAs contributes with an in-plane strain of -0.15% . It results that the multilayer tends to introduce dislocations on the $[110]$ and $[\bar{1}10]$ directions in order to partially relax the structure. Following [4, 5] one can try to suppress the formation of the misfit dislocations alternating the sign of the strain, in order to minimize the term S defined as

$$S = \left| \sum_i^N \epsilon_i C_i d_i \right| \quad \text{with} \quad C_i = \frac{c_{11i}^2 + c_{11i}c_{12i} - 2c_{12i}^2}{c_{11i}}, \quad (1)$$

where the index i refers to the i th layer of thickness d_i and c_{11i} and c_{12i} are the relative elastic constants in the assumption of cubic crystal material. The reduction of S can be obtained using $\text{GaAs}_{1-y}\text{P}_y$, because this alloy can easily replace $\text{Al}_{0.20}\text{Ga}_{0.80}\text{As}$ in part of the structure. In fact, for values of y between 0.2 and 0.3, $\text{GaAs}_{1-y}\text{P}_y$ has a band structure and also a refractive index that properly fit to that purpose [6] just by adjusting the optical thickness.

4. Characterization of the Samples

Different methods are used to characterize the samples. First of all, HRXRD (high resolution x-ray diffraction) measurement are performed on the as grown samples. In fact, symmetric $\omega - 2\theta$ scans relative to the (002) and (004) Bragg reflections provide important informations about the grown structure. For example the (002) allows the accurate investigation of the AlAs/ $\text{Al}_{0.20}\text{Ga}_{0.80}\text{As}$ due to the high contrast of the scattering factors given by the presence of aluminum, and, on the other hand, the (004) reflection is more intense and it is more sensitive to strain [7]. HRXRD allows to measure the exact thickness and concentration of the layers in the structure. In particular, the phosphorus concentration of the strain compensating layers and the indium concentration in the QWs can be determined. An example is given in Fig. 1, where the measured and simulated HRXRD spectra relative to the sample *d* are shown. The simulation is performed considering that for the MBE growth just 4 independent parameters are needed to generate the complex structure [3]. In particular from the (004) spectrum the phosphorus concentration of the GaAsP layer and indium concentration of the QWs can be determined. Using these informations, the strain status of the sample and the value of S can be indirectly calculated. On the other hand, S can be more directly found just by measuring the radius of curvature R of the as grown sample and by using the Stoney's formula. In fact, the curvature of a crystalline multilayer belonging to the cubic system system can be calculated using the relation

$$\kappa = \frac{1}{R} \simeq \frac{6}{C_{\text{sub}}d_{\text{sub}}^2} \sum_i m_i C_i d_i \simeq -\frac{6}{C_{\text{sub}}d_{\text{sub}}^2} \sum_i \epsilon_i C_i d_i, \quad (2)$$

where m_i is the lattice mismatch of the i th layer. The formula above shows that the measurement of the radius of curvature for substrate of fixed thickness (for the used

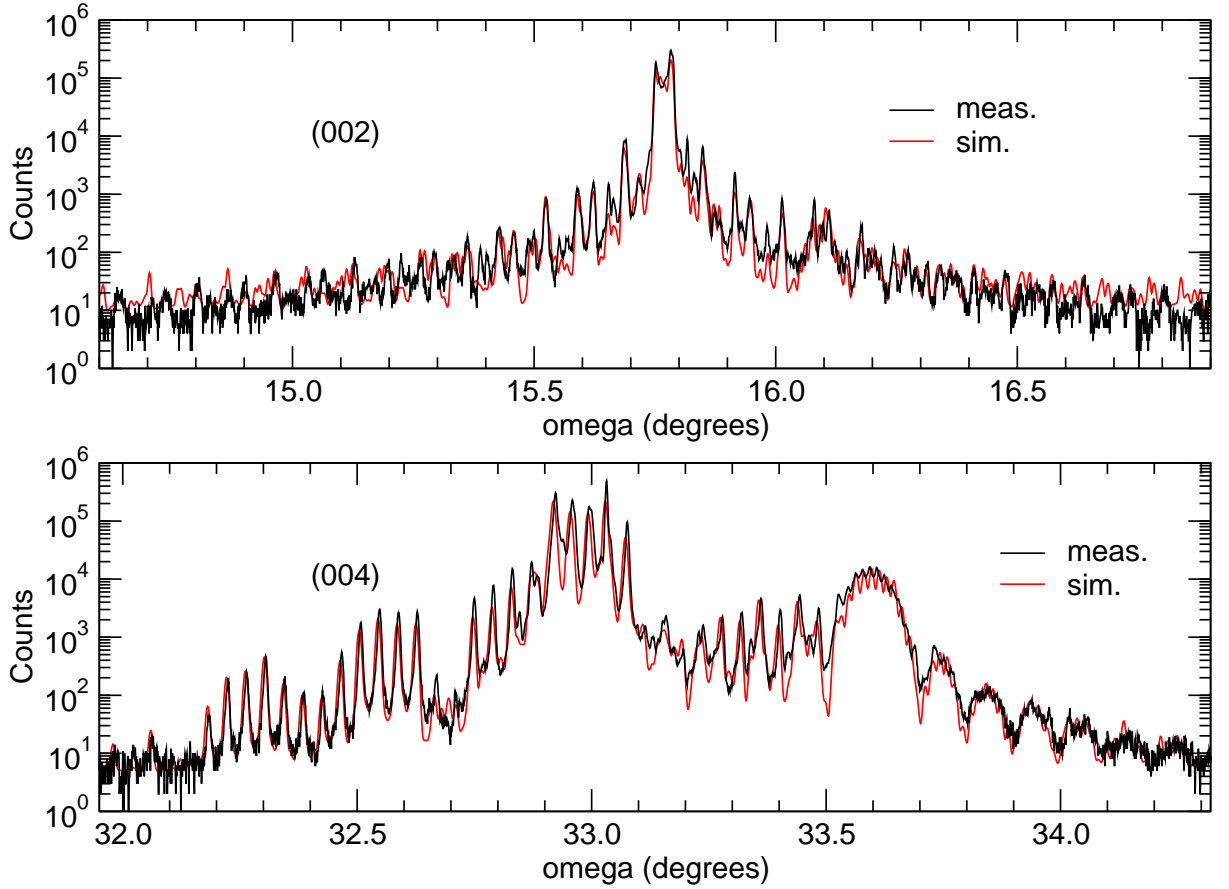


Fig. 1: Symmetric (002) and (004) spectra of the sample *d*. Just 4 independent parameters are needed to describe the complex structure. The phosphorus concentration in the GaAsP layer is 21 %, the indium concentration in the QWs is 8 %.

GaAs substrates ($d_{\text{sub}} = 350 \mu\text{m}$) is directly connected to the strain compensation term S . The curvature κ can be easily obtained experimentally using, for example, HRXRD [3, 8], where the angle ω of the substrate diffraction peak, in this case the (004) Bragg reflection, is determined on different sample points lying at different x positions on the intersection line between the sample surface and the diffraction plane. The radius of curvature can be calculated considering the ratio between the increments of Δx and $\Delta\omega$.

As final characterization, the effect of strain compensation on the structure can be visualized by illuminating the prepared laser chip with the 808 nm pump laser light and recording the infrared picture. As can be seen in Fig. 2, orthogonal sets of dark lines are visible on the samples *a* and *b*. The strong suppression of the photoluminescence localized in these lines can be directly observed and it is clearly detrimental for the laser function. In fact, not only a lower efficiency is recorded, but also a shorter device lifetime.

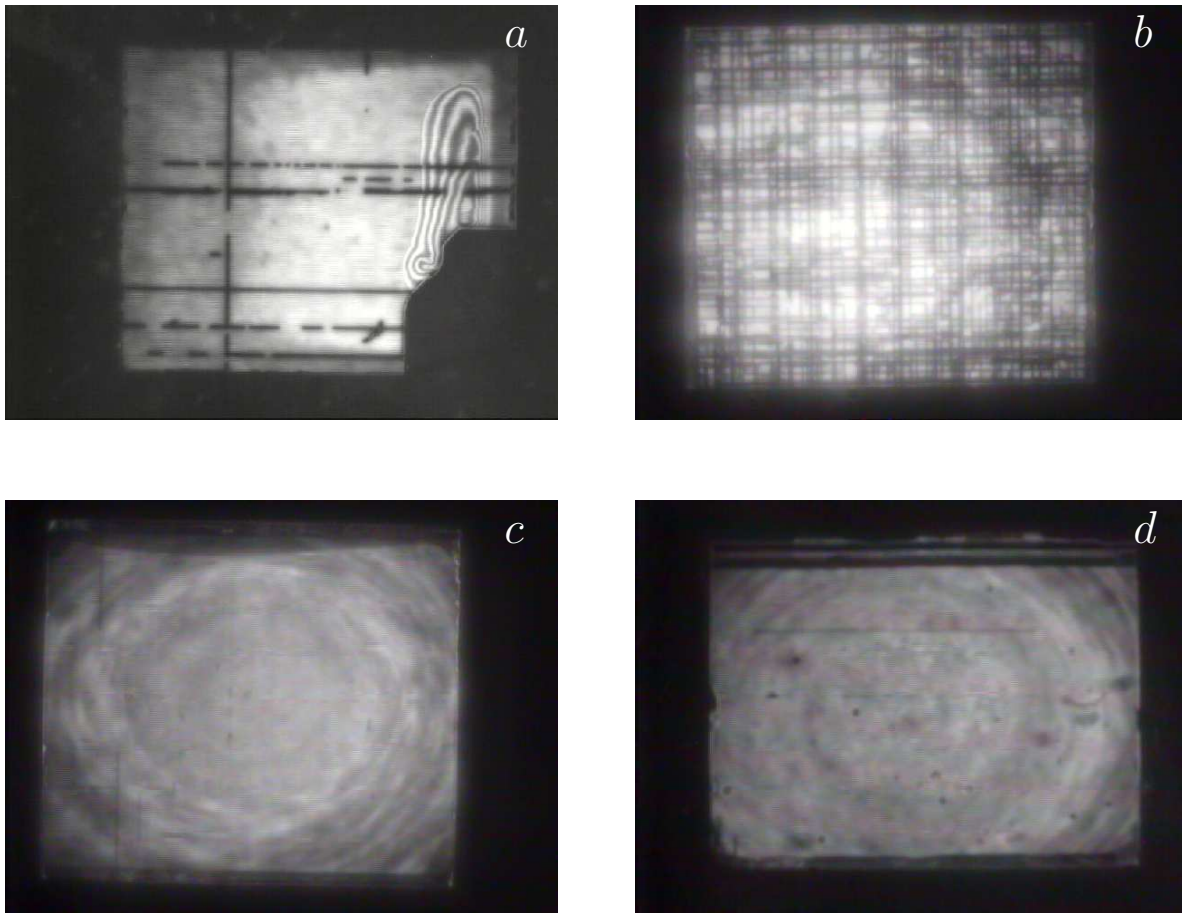


Fig. 2: Infrared pictures of the samples *a*, *b*, *c*, *d* described in the text. The probes are illuminated with 808 nm light and the dark lines are easily recognizable in an orthogonal pattern. The dimension of each chip is approximately $1\text{ mm} \times 1.5\text{ mm}$.

5. Discussion

The significant features of the considered four samples are presented in Table 1. The sample *a* and *b* are not strain compensated. The two samples differ in the number of QWs and also in the value of the middle concentration of the aluminum alloy in the DBBR. In fact, while in the sample *a* the aluminum alloy concentration of the $4.2\text{ }\mu\text{m}$ thick reflector is 68% in the sample *b* this value is raised to 75%. As consequence the sample *b* is more compressively strained than the sample *a*, as can also be seen by the strong differences in radius of curvature. The abundance of dark lines results in a low efficiency and a reduced lifetime of the device. On the other hand, the samples *c* and *d* show even less dark lines than the sample *a*, even though they incorporate both DBBR with higher aluminum content. The last two samples are in fact strain compensated.

In sample *c*, the strain compensation layers consist in six 8 nm thick $\text{GaAs}_{0.71}\text{P}_{0.29}$ situated regularly between the QWs. Instead in sample *d*, several $\text{GaAs}_{0.79}\text{P}_{0.21}$ layers having a total thickness of approximately 600 nm, are placed not only between the QWs but also in the DBBR. Considering that the two devices exhibit comparable performances,

Table 1: Summary of data of the 4 samples described in the text.

Sample	Number of QWs	DBBR Al fraction (%)	Radius of curvature (m)	Phosphorus fraction in GaAsP alloy (%)
<i>a</i>	6	69	6.3	0
<i>b</i>	12	75	3.2	0
<i>c</i>	6	75	3.8	29
<i>d</i>	16	72	7.0	21

of more than 5 W output power at 920 nm under an absorbed pump power of 11 and 12 W respectively, one can conclude that the strain arisen from DBBR does not play an important role even though stores most of the elastic energy in the structure. In fact the the radius of curvature of the structure *c* containing a not strain compensated DBBR is much shorter than the one of structure *d* containing a partially strain compensated one.

6. Conclusion

One can prove that even with relatively weak strained $\text{In}_{0.08}\text{Ga}_{0.92}\text{As}$ QWs, that are required for 920 nm emission, disk laser chips take advantage from the introduction of strain compensating layers in the structure, especially when DBBR having an higher content of aluminum are utilized. Almost no dark lines are observed when two different strain compensation scheme are used for devices that show comparable performances. For this reason, more detailed studies are needed to clarify which approach is more convenient in order to further improve the devices.

As conclusion, it is important to emphasize the good efficiency of the strain compensated samples. As example, sample *c* exhibits an output power of 5.4 W at 920 nm for an absorbed 808 nm pump power of 11.0 W and applying SHG achieves 1.6 W at 460 nm [9].

References

- [1] M. Kuznetsov, F. Hakimi, R. Sprague, and A. Moradian, "Design and characteristics of high-power (>0.5-W cw) diode-pumped vertical-external-cavity surface-emitting semiconductor laser with circular TEM_{00} beams", *IEEE J. Select. Topics Quantum Electron.*, vol. 5, no. 3, pp. 561–573, 1999.
- [2] F. Demaria, *Schicht- und Resonatordesign von Halbleiterscheibenlasern*. Ph.D. thesis, Ulm University, Ulm, 2008.
- [3] F. Rinaldi, *MBE Growth and Characterization of Multilayer Structures for Vertically Emitting Laser Devices*. Ph.D. thesis, URL: <http://vts.uni-ulm.de/doc.asp?id=6667>, Ulm University, Ulm, 2008.

- [4] W.D. Nix, “Mechanical properties of thin films”, *Metallurgical Transactions A*, vol. 20A, pp. 2217–2245, 1989.
- [5] L.D. Landau and E.M. Lifshitz, *Theory of Elasticity*, Pergamon Press, 1986.
- [6] G.D. Clark, Jr. and N. Holonyak, Jr., “Optical properties of gallium arsenide-phosphide”, *Phys. Rev.*, vol. 156, no. 3, pp. 913–924, 1966.
- [7] P.F. Fewster, *X-Ray Scattering from Semiconductors*, Imperial College Press, 2000.
- [8] V. Holý, U. Pietsch, and T. Baumbach, *High-Resolution X-Ray Scattering from Thin Films and Multilayers*, Springer, 1999.
- [9] F. Demaria and A. Hein, “Intra-cavity second-harmonic generation of blue 460 nm watt-level emission from optically pumped semiconductor disk lasers”, *Annual Report 2009*, pp. 3–10. Ulm University, Institute of Optoelectronics.

Design of a Short Integrated VECSEL Resonator

Wolfgang Schwarz

In this report, the design of a short vertical extended cavity surface-emitting laser (VECSEL) is outlined. The propagation of the beam in the structure is described by a linear ABCD-matrix approach. The necessary radius of curvature of the output coupler is calculated. Finally, proper coupling of the emitted beam into a multimode fiber is considered.

1. Introduction

For some applications it is beneficial to integrate a vertical-cavity surface-emitting laser (VCSEL) with an external curved mirror. Here, the external mirror defines the transverse mode structure and enhances the optical field in the extended resonator.

The investigated resonator structure is schematically depicted in Fig. 1. The VCSEL consists of an active zone with a multiple quantum well structure embedded between two Bragg reflectors (DBRs). The DBRs are implemented as a thinner p-doped mirror (p-DBR) and a thicker n-doped mirror (n-DBR). A buried layer of doped AlAs above the active region is selectively oxidized. Thereby transverse optical guiding is provided. Furthermore the circular oxide aperture restricts the axial current flow to the center of the active zone. This results in sufficient transverse overlap of the laser mode and the carrier injection profile. VCSELs can be operated in a single transverse mode along with stable polarization by introducing a mode-selective loss mechanism relying on the surface grating relief technique [1].

The emission wavelength of the VCSEL is defined by the Bragg wavelength of the DBRs and by the effective length of the inner cavity. Both are adjusted for a wavelength of 850 nm. Chemical wet-etching of the p-DBR and the active zone results in a circular mesa. On top of the latter, an annular metal contact is deposited. The substrate is electrically interfaced with a planar metal contact. The VCSEL is mounted underneath a microfluidic channel, with the p-DBR facing up. The channel is fabricated from polymethyl methacrylate (PMMA). By hot embossing, a concave-shaped surface is created. This surface defines the output coupler of the laser and therefore it is coated with a dielectric DBR. Above the output coupler, an optical fiber can be plugged into a circular recess which is embossed into the PMMA. By this means, the emitted light is coupled straight into the fiber.

An aqueous solution with refractive index $n = 1.33$ perfuses the channel. The channel height is 30 μm . A 30 μm thick glass cover lid ($n = 1.51$) is bonded to the channel walls and seals the channel against leakage.

2. Resonator Model

The presented resonator structure implies a three-mirror system: two plane DBRs forming the internal resonator within the VCSEL and the curved DBR in the extended resonator. An appropriate beam analysis for such a resonator structure can be made by utilizing the ABCD-matrix law. Here a Gaussian beam is assumed. Thus the analysis is restricted to optical fields propagating close to the optical axis. This propagation as well as refraction and reflection are described by a matrix

$$M_i = \begin{pmatrix} A_i & B_i \\ C_i & D_i \end{pmatrix}. \quad (1)$$

The index i refers to the i -th layer or interface in the structure. For simple propagation in a homogeneous layer, the elements are $A_i = 1$, $B_i = d$, $C_i = 0$, and $D_i = 1$, with d being the layer thickness. In case of a beam propagating from a medium with refractive index n_i to a medium with refractive index n_{i+1} , the elements in M_i are $A_i = 1$, $B_i = 0$, $C_i = n_i/(R_i n_{i+1})$, and $D_i = n_i/n_{i+1}$. The radius of curvature R_i is positive in case of a concave interface and becomes infinity in case of a flat interface. Other matrices for reflection exist, but are not included in the subsequent calculations. Hence, these calculations do not account for reflections at the parasitic interfaces, which result in a distorted laser mode. In a practical device, the air/glass interface should be anti-reflection coated in order to suppress unwanted losses from this interface.

The complex beam parameter $q(z)$ represents the real beam spot size $w(z)$ and the radius of curvature $R(z)$ of the beam front in a Gaussian beam travelling along the z -axis. The complex beam parameter is expressed by $1/q(z) = 1/R(z) - i\lambda/(\pi w^2(z) n_i)$. Here, λ is the optical wavelength of the monochromatic beam and $i = \sqrt{-1}$ is the complex unit. For every axial position, $q(z)$ can be calculated according to $q_{i+1} = (A_i + B_i q_i)/(C_i + D_i q_i)$.

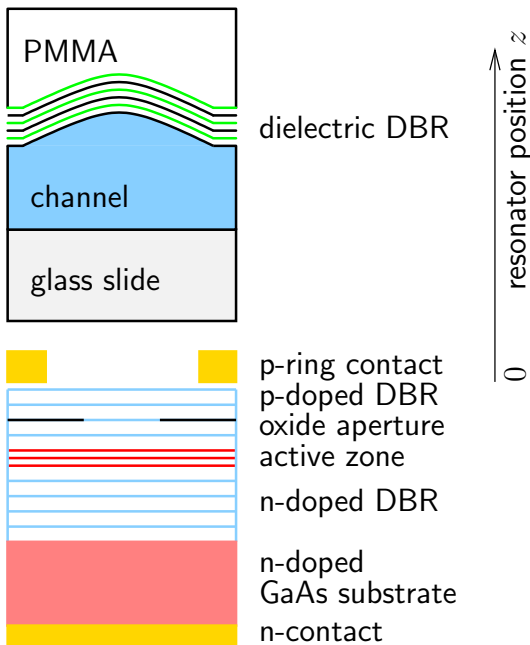


Fig. 1: Schematic drawing of the analyzed resonator structure. It comprises the VCSEL, the microfluidic channel and the hot-embossed PMMA channel wall, which is coated with a dielectric DBR.

Internal and extended resonator differ in length by more than one order of magnitude. This suggests a plane beam front passing the p-DBR, neglecting thermal lensing and other guiding or anti-guiding effects in the VCSEL [2], [3]. The radius of curvature and the beam spot size were calculated for initial beam diameters of 8 and 10 μm . The radius of curvature of the beam front is shown in Fig. 2. The invisible pole at the position $z = 0$ is in accordance with the assumed plane beam front at this point. The air/glass boundary at the axial position of 20 μm shifts the radius of curvature of the beam front towards a larger radius (i.e., weaker bending). An opposite shift is introduced at the glass/channel boundary at $z = 50 \mu\text{m}$. When passing the concave extended mirror at $z = 80 \mu\text{m}$, the radii of curvature are 158 and 264 μm , respectively. The concave extended mirror should match this curvature in order to establish a stable resonator. Doing so, the beam can make multiple bounces between the end mirrors while retaining its spot size and its radius of curvature of the beam front.

2.1 Output coupler and optical fiber launch

The aperture of the output coupler should be sufficiently larger than the beam. Any cut-off results in optical loss. The losses can be estimated from the ratio of cut-off and incident optical powers for transmission through a circular metallic aperture with radius ρ , which amounts to $\exp(-2\rho^2/w^2(z))$. The beam spot size is depicted in Fig. 3. The beam is continuously diverging from its initial diameter of 8 μm (and 10 μm , not shown here). The calculations yield loss ratios of less than $2 \cdot 10^{-6}$ for the fundamental mode in case of an aperture radius of 15 μm . Higher-order modes with a beam parameter product of $M^2 = 2$ experience a relative loss of $6 \cdot 10^{-3}$, which is substantially higher. In conjunction with a resonator loss caused by the transmitted light of approximately $2 \cdot 10^{-2}$, this facilitates mode discrimination for fundamental mode operation.

The emitted light can be coupled directly into an optical fiber. This necessitates a fiber with an aperture which is large enough to accommodate the transverse beam profile. Furthermore, the numerical aperture of the fiber should exceed that of the VECSEL. This is achieved if the beam passes the aperture of the output coupler and travels 200 μm in the PMMA. At this position, a 50 μm core diameter graded-index multimode fiber is placed. The aperture of the fiber core is expected to receive 89% of the incident power.

3. Conclusion

The calculation of a Gaussian beam propagating in a multilayer cavity provides the necessary radii of curvature of the optical elements. By using the ABCD-matrix method the beam profile was traced along the axis of propagation. There is indication that direct optical coupling to a multimode fiber is feasible and that the resonator has favorable mode discrimination for fundamental mode operation.

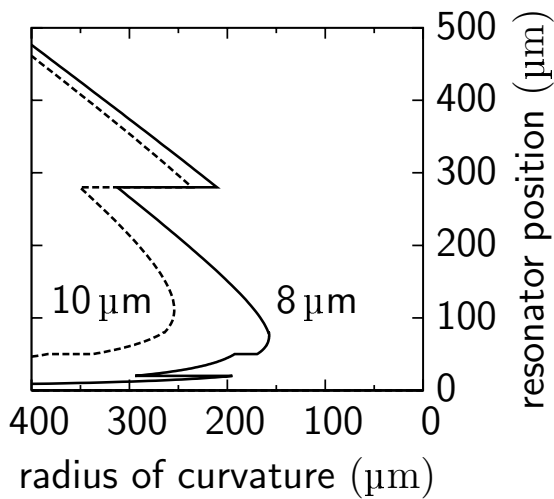


Fig. 2: Calculated radii of curvature of the beam front in the extended resonator. The beam propagates bottom up. Two different initial beam spot sizes of $8\ \mu\text{m}$ and $10\ \mu\text{m}$ are assumed.

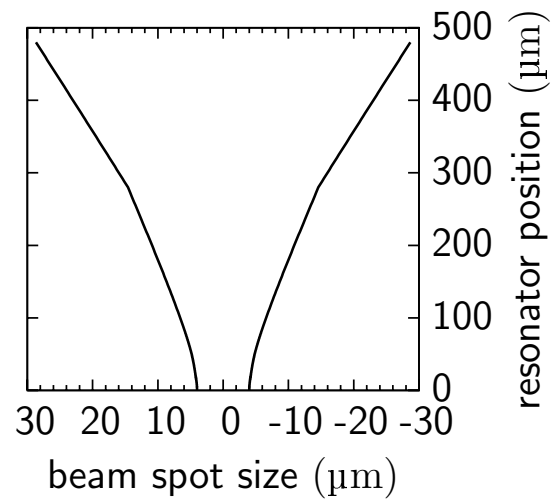


Fig. 3: Calculated beam spot sizes of the beam in the extended resonator. The direction of propagation is the same as in Fig. 2. The initial beam spot size is $8\ \mu\text{m}$.

References

- [1] J.M. Ostermann, F. Rinaldi, P. Debernardi, and R. Michalzik, “VCSELs with enhanced single-mode power and stabilized polarization for oxygen sensing”, *IEEE Photon. Technol. Lett.*, vol. 17, no. 11, pp. 2256–2258, 2005.
- [2] G.A. Smolyakov and M. Osiński, “Analysis of ring-metal-aperture VCSELs for single-lateral-mode operation”, *J. Lightwave Technol.*, vol. 23, pp. 4278–4286, 2005.
- [3] L. Raddatz, I.H. White, H.D. Summers, K.H. Hahn, M.R. Tan, and S.-Y. Wang, “Measurement of guiding effects in vertical-cavity surface-emitting lasers”, *IEEE Photon. Technol. Lett.*, vol. 8, pp. 743–746, 1996.

High-Order-Mode VCSEL With 12 mW Output Power

A. Gadallah

We report high-power single-higher-order transverse mode emission of a large-area oxide-confined rectangular-shaped VCSEL with a multi-spot shallow surface relief. Both a record-high output power of 12 mW and a record-low differential series resistance of 18 ohms are achieved. Stable single-higher-order transverse mode emission with a side-mode suppression ratio exceeding 35 dB is maintained up to thermal rollover. Measurements of near- and far-field intensity profiles of the higher-order mode are presented.

1. Introduction

The special features of VCSELs such as low power consumption, circular beam shape, emission perpendicular to the wafer surface, on-wafer testing before packaging, and efficient high-frequency modulation are providing the motivation for a continued search for new device types. Besides, VCSELs are ideally suited to form two-dimensional arrays of compact optical sources owing to their low threshold currents and high packing density. These attributes make VCSELs attractive light sources for various applications such as optical data transmission [1], optical navigation with computer mice [2], gas sensing [3], optical illumination and pumping [4], or optical particle manipulation [5]. However, VCSELs normally operate in multiple transverse modes, due to the large transverse dimensions of the device. Many VCSEL applications, on the other hand, require high-power single transverse mode emission. Hence, much effort has been invested in the research into such single-mode VCSELs.

For this aim, we contribute with a VCSEL type that has a rectangular aperture with large aspect ratio and provides high single-mode power using a shallow etching technique. In this technique, a quarter-wavelength antiphase layer is added onto a regular top Bragg reflectors in order to induce a decrease in top mirror reflectivity. This layer is then selectively removed during processing by means of wet-chemical etching, such that the threshold gain of a desired mode is lower than that of all other transverse modes. The oscillating laser mode has a high transverse mode order. The emitted laser wavelength is around 850 nm. As an additional favorable feature, the devices show low differential series resistances due to the large aperture area compared with usual single transverse mode VCSELs.

2. Description of the Device

Figure 1 shows a schematic (top) and a top view (bottom) of an 8-spot surface-etched rectangular-shaped VCSEL to enforce single-mode operation of the E_{81} mode having 8 maxima along the aperture length and one maximum along the aperture width. The epitaxial material was provided by Philips Technologie GmbH U-L-M Photonics. The layer structure consists of a bottom n-doped 37 pairs distributed Bragg reflector (DBR), a one-wavelength thick cavity containing three 8 nm thick GaAs quantum wells separated by 10 nm AlGaAs barriers, a 22 pairs p-DBR and a topmost quarter-wave thick GaAs antiphase layer, all grown on an n-GaAs substrate.

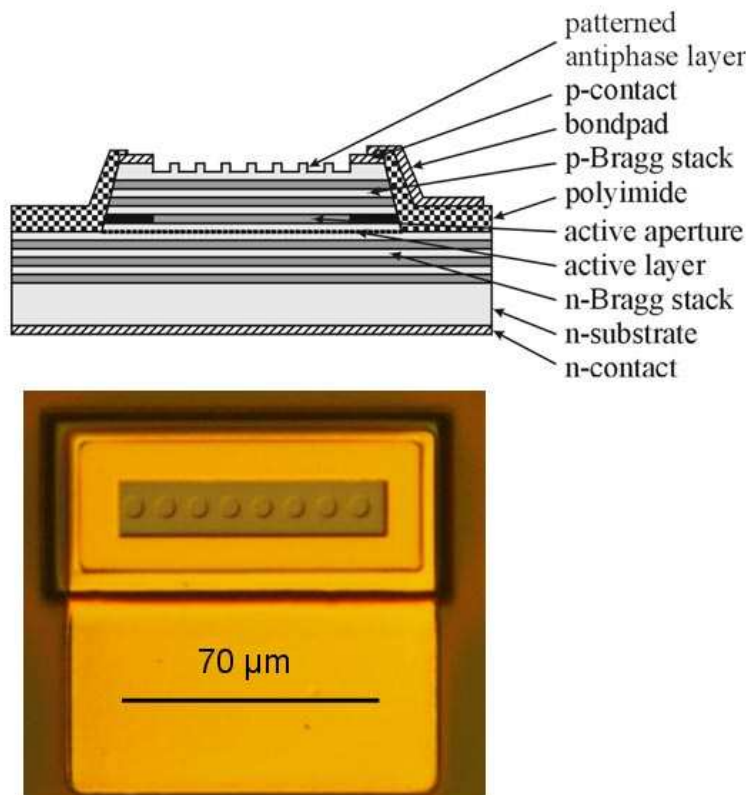


Fig. 1: Schematic drawing (top) and top view (bottom) of a fully-processed 8-spot shallow surface etched rectangular-shaped VCSEL.

The cavity resonance is in the vicinity of 850 nm. The antiphase layer induces losses for the total structure. This layer is selectively removed in a single processing step using wet-chemical etching. The 8-spot shallow etch pattern in Fig. 1 is adapted to the intensity profile of the E_{81} mode. The diameter of each spot is about $6 \mu\text{m}$, the pitch is $9 \mu\text{m}$ and the active aperture area is about $6 \mu\text{m} \times 68 \mu\text{m}$. The pattern is designed such that there is a maximum overlap between the etched spots and the calculated intensity maxima of the targeted mode. With this method, a single-higher-order transverse mode is selected. The analysis of higher-order-mode selection using surface etching was reported in [6]. Current confinement is achieved through thermal oxidation of an AlAs layer placed just above the one-wavelength thick inner cavity. This step defines the aperture area mentioned above.

Wet etching is used to reach the AlAs layer. N- and p-type metalization processes are applied, followed by polyimide passivation. Finally, bondpad metalization is carried out for electrical contacting.

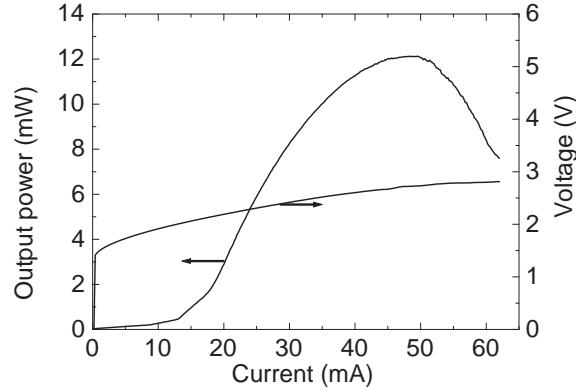


Fig. 2: CW operation characteristics of an 8-spot surface-relief VCSEL with an active aperture area of $6.3 \times 68.3 \mu\text{m}^2$.

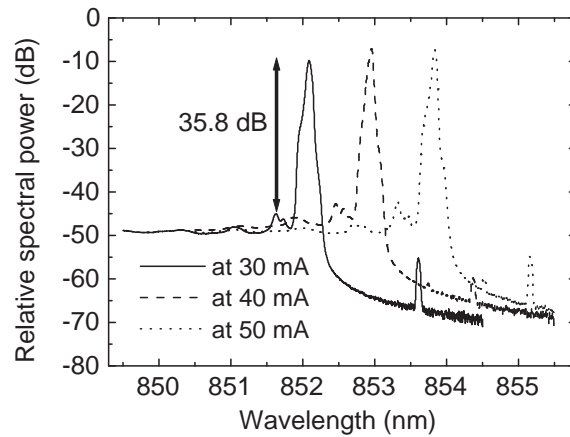


Fig. 3: Emission spectra of the device in Fig. 2 at different currents.

3. Characterization and Results

Room-temperature continuous-wave light–current–voltage (LIV) characteristics of the device from Fig. 1 are shown in Fig. 2. The corresponding spectra at different currents are depicted in Fig. 3. The competitive mode is about 35 dB lower than the targeted mode even up to thermal rollover. The maximum output power at thermal rollover is 12 mW, which is a record-high output power for fully monolithic VCSELs, either oscillating on the fundamental mode [7]– [15] or on higher-order modes [16], [17]. The average differential series resistance is 18Ω , as obtained from the slope of the current–voltage curve in the range from 20 to 50 mA, which is remarkably low. The threshold current is 12.8 mA and the maximum differential quantum efficiency is 38.5%. The relatively high threshold is due to optical losses induced by the antiphase layer.

In order to identify the main modes in the spectra in Fig. 3, we have performed spectrally resolved near-field measurements by scanning a lensed fiber tip over the output aperture with high resolution. Figure 4 shows the near-field intensity profile of the same VCSEL at 30 mA, taken with a spectral width of 0.046 nm centered around the spectral peak in Fig. 3 (no changes are observed even with 5 nm spectral width). In contrast to the simulations,

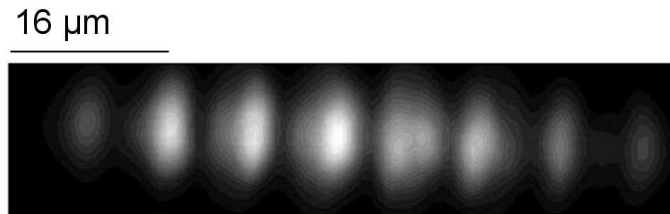


Fig. 4: Near-field intensity profile of the device in Fig. 2 at 30 mA.

there is a marked difference between the intensity maxima and shape of the spots. We attribute this to the inhomogeneous temperature throughout the active aperture, which leads to cavity detuning. Figure 5 shows the measured far-field intensity in the plane defined by the etch spots. Four major peaks are observed. The peak positions correspond well with model calculations assuming diffraction from a multi-spot phase grating, where the distance between spots and the phase shift of $\pi/2$ between etched and unetched regions are the main parameters.

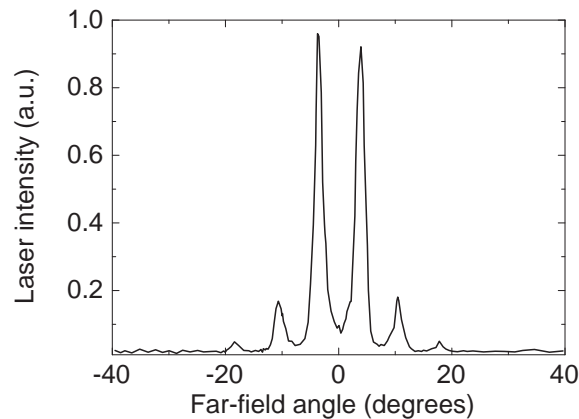


Fig. 5: Measured far-field intensity profile corresponding to Fig. 4.

4. Conclusion

We have demonstrated that large-area ($> 400 \mu\text{m}^2$) multi-spot surface-etched rectangular-shaped VCSELs show stable high-power single-higher-order transverse mode emission. Moreover, the differential series resistance is low. Near- and far-field intensity profiles prove the successful mode selection. The manufacturing of this VCSEL needs only one additional lithography and etching step, which makes it attractive for commercial fabrication. The VCSELs are intended to be applied for optical manipulation of microparticles.

When positioned at an angle with respect to the fluidic flow direction underneath a microfluidic chip, all-optical deflection of flowing particles can be achieved with light forces. Non-mechanical sorting is thus possible [5]. With the VCSEL presented here, the distance between the intensity spots is 9 μm , which cannot be easily achieved with conventional linear VCSEL arrays as applied in [5].

References

- [1] R. Michalzik and K.J. Ebeling, “Operating principles of VCSELs”, Chap. 3 in *Vertical-Cavity Surface-Emitting Laser Devices*, H. Li and K. Iga (Eds.), pp. 53–98. Berlin: Springer-Verlag, 2003.
- [2] A. Pruijboom, M. Schemmann, J. Hellmig, J. Schutte, H. Moench, and J. Pankert, “VCSEL-based miniature laser-Doppler interferometer”, in *Vertical-Cavity Surface-Emitting Lasers XII*, C. Lei, J.K. Guenter (Eds.), Proc. SPIE 6908, pp. 69080I-1–7, 2008.
- [3] J.M. Ostermann, F. Rinaldi, P. Debernardi, and R. Michalzik, “VCSELs with enhanced single-mode power and stabilized polarization for oxygen sensing”, *IEEE Photon. Technol. Lett.*, vol. 17, no. 11, pp. 2256–2258, 2005.
- [4] J.-F. Seurin, G. Xu, Q. Wang, B. Guo, R. Van Leeuwen, A. Miglo, P. Pradhan, J.D. Wynn, V. Khalfin, and C. Ghosh, “High-brightness pump sources using 2D VCSEL arrays”, in *Vertical-Cavity Surface-Emitting Lasers XIV*, J.K. Guenter, K.D. Choquette (Eds.), Proc. SPIE 7615, pp. 76150F-1–9, 2010.
- [5] R. Michalzik, A. Kroner, A. Bergmann, and F. Rinaldi, “VCSEL-based optical trapping for microparticle manipulation”, in *Vertical-Cavity Surface-Emitting Lasers XIII*, K.D. Choquette, C. Lei (Eds.), Proc. SPIE 7229, pp. 722908-1–13, 2009.
- [6] A. Gadallah, A. Kroner, I. Kardosh, F. Rinaldi, and R. Michalzik, “Oblong-shaped VCSELs with pre-defined mode patterns”, in *Semiconductor Lasers and Laser Dynamics III*, K.P. Panayotov, M. Sciamanna, A.A. Valle, R. Michalzik (Eds.), Proc. SPIE 6997, pp. 69971R-1–9, 2008.
- [7] R.A. Morgan, G.D. Guth, M.W. Focht, M.T. Asom, K. Kojima, L.E. Rogers, and S.E. Callis, “Transverse mode control of vertical-cavity top-surface-emitting lasers”, *IEEE Photon. Technol. Lett.*, vol. 4, no. 4, pp. 374–376, 1993.
- [8] C. Jung, R. Jäger, M. Grabherr, P. Schnitzer, R. Michalzik, B. Weigl, S. Müller, and K.J. Ebeling, “4.8 mW singlemode oxide confined top-surface emitting vertical-cavity laser diodes”, *Electron. Lett.*, vol. 33, no. 21, pp. 1790–1791, 1997.
- [9] H.J. Unold, M.C. Riedl, S.W.Z. Mahmoud, R. Jäger, and K.J. Ebeling, “Long monolithic cavity VCSELs for high singlemode output power”, *Electron. Lett.*, vol. 73, no. 3, pp. 178–179, 2001.

- [10] A.J. Fischer, K.D. Choquette, W.W. Chow, A.A. Allerman, D.K. Serkland, and K.M. Geib, “High single-mode power observed from a coupled-resonator vertical-cavity laser diode”, *Appl. Phys. Lett.*, vol. 79, no. 25, pp. 4079–4081, 2001.
- [11] D. Zhou and L.J. Mawst, “High-power single-mode antiresonant reflecting optical waveguide-type vertical-cavity surface-emitting lasers”, *IEEE J. Quantum Electron.*, vol. 38, no. 12, pp. 1599–1606, 2002.
- [12] Å. Haglund, J.S. Gustavsson, J. Vukušić, P. Modh, and A. Larsson, “Single fundamental mode output power exceeding 6 mW from VCSELs with a shallow surface relief”, *IEEE Photon. Technol. Lett.*, vol. 16, no. 2, pp. 368–370, 2004.
- [13] A. Furukawa, S. Sasaki, M. Hoshi, A. Matsuzono, K. Moritoh, and T. Baba, “High-power single-mode vertical-cavity surface-emitting lasers with triangular holey structure”, *Appl. Phys. Lett.*, vol. 85, no. 22, pp. 5161–5163, 2004.
- [14] A. Kroner, F. Rinaldi, J.M. Ostermann, and R. Michalzik, “High-performance single fundamental mode AlGaAs VCSELs with mode-selective mirror reflectivities”, *Optics Communications*, vol. 270, no. 2, pp. 332–335, 2006.
- [15] J.-W. Shi, C.-C. Chen, Y.-S. Wu, S.-H. Guol, C. Kuo, and Y.-J. Yang, “High-power and high-speed Zn-diffusion single fundamental-mode vertical-cavity surface-emitting lasers at 850-nm wavelength”, *IEEE Photon. Technol. Lett.*, vol. 20, no. 13, pp. 1121–1123, 2008.
- [16] P.R. Claisse, W. Jiang, P.A. Kiely, B. Gable, and B. Koonse, “Single high order mode VCSEL”, *Electron. Lett.*, vol. 34, no. 7, pp. 681–682, 1998.
- [17] S. Shinada and F. Koyama, “Single high-order transverse mode surface-emitting laser with controlled far-field pattern”, *IEEE Photon. Technol. Lett.*, vol. 14, no. 12, pp. 1641–1643, 2002.

Static Characteristics of VCSELs and PIN Photodiodes for Bidirectional Standard Multimode Fiber Transmission

Alexander Kern and Dietmar Wahl

We present the monolithic design, fabrication and static properties of 850 nm wavelength AlGaAs–GaAs-based transceiver chips with a stacked layer structure of a VCSEL and a PIN photodetector. Bidirectional data transmission via a single, two-side butt-coupled multimode fiber (MMF) is thus enabled. The approach aims at a miniaturization of transceiver chips in order to ensure compatibility with standard MMFs with core diameters of 50 and 62.5 μm used predominantly in premises networks. These chips are supposed to be well suited for low-cost and compact half- and full-duplex interconnection at Gbit/s data rates over distances of a few hundred meters.

1. Introduction

Owing to the increasing penetration of optical interconnection into mobile systems, local industrial networks and nowadays also into the home environment, compact and low-cost transceivers are more and more needed. A possible way to satisfy this demand is a transceiver chip which consists of a vertical-cavity surface-emitting laser (VCSEL) sharing the chip area with an intimately integrated photodetector. The monolithic integration of both components as well as a design avoiding the use of external optics saves space, weight and module cost.

So far there have been several examples of monolithic integration of a VCSEL and a photodetector for optical interconnection purposes. An interesting attempt to use a VCSEL as an efficient laser source and a resonant-cavity-enhanced avalanche photodetector is introduced in [1]. Such a dual-purpose device is switched between two operation modes. Half-duplex operation at 1.25 Gbit/s data rate over a 50 μm core diameter MMF with 500 m length was demonstrated. Full-duplex data transmission is possible in case of spatial separation of both devices. Similar to [1], just one epitaxial layer structure for a VCSEL can be used in order to fabricate monolithically integrated transceivers consisting of a VCSEL and a resonant photodetector [2]. Unfortunately such solutions are not well suited for low-cost links owing to resonant detection, which requires temperature control at both fiber ends due to the very narrow spectral range of the photodetector. Non-resonant detection is achieved by the employment of separate epitaxial layers for photodiode and VCSEL [3,4]. Usually such a transceiver is grown in one run and thus contains all the epitaxial layers from the beginning. Both the vertical and horizontal separation of the devices is achieved by means of lithography and selective etching techniques.

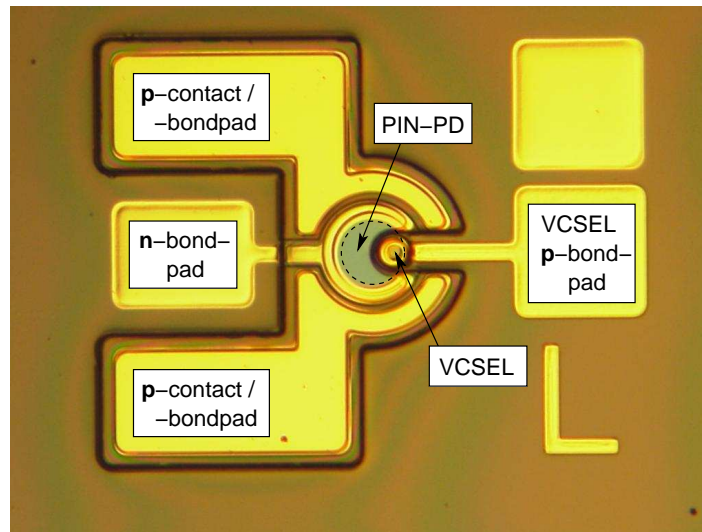


Fig. 1: Photograph of a transceiver chip consisting of a VCSEL and a 60 μm diameter PIN PD. The VCSEL is positioned off-center with respect to the photodetector in order to maximize the effective photodetecting area of the transceiver. The dashed line indicates the alignment of a MMF with 50 μm core diameter.

In recent years, we have shown several designs of monolithically integrated VCSELs and GaAs-based metal–semiconductor–metal (MSM) photodiodes [5]. Since MSM photodiodes generally have lower responsivities due to their metal contact fingers that partially shadow the detector area, PIN-type photodiodes are predestined for applications implying reduced fiber core diameters. Matching the transceiver chips to standard MMFs requires further miniaturization of the VCSEL in order to maximize the photosensitive area of the integrated chip. Figure 1 shows a transceiver chip with a 60 μm PIN PD and a laterally integrated VCSEL.

2. Chip Layout and Processing

A monolithically integrated transceiver chip comprises all epitaxial layers necessary for signal generation and detection. Figure 2 illustrates schematically such a layer structure grown by molecular beam epitaxy.

2.1 VCSEL

The layers for the PIN photodetector are grown on top of the VCSEL layers, separated by a 150 nm thick $\text{Al}_{0.9}\text{Ga}_{0.1}\text{As}$ etch stop layer. The resonator of the VCSEL is built by a n-type doped bottom Bragg mirror containing 38.5 $\text{Al}_{0.2}\text{Ga}_{0.8}\text{As}/\text{Al}_{0.9}\text{Ga}_{0.1}\text{As}$ periods grown on a n-doped GaAs substrate and 23 equivalent p-type top mirror pairs. The inner cavity has an optical thickness of one wavelength and contains three 8 nm thick GaAs quantum wells, separated by 10 nm $\text{Al}_{0.27}\text{Ga}_{0.73}\text{As}$ barrier layers. A 32 nm thick p-doped AlAs layer in the first top mirror period above the active region is designated for current

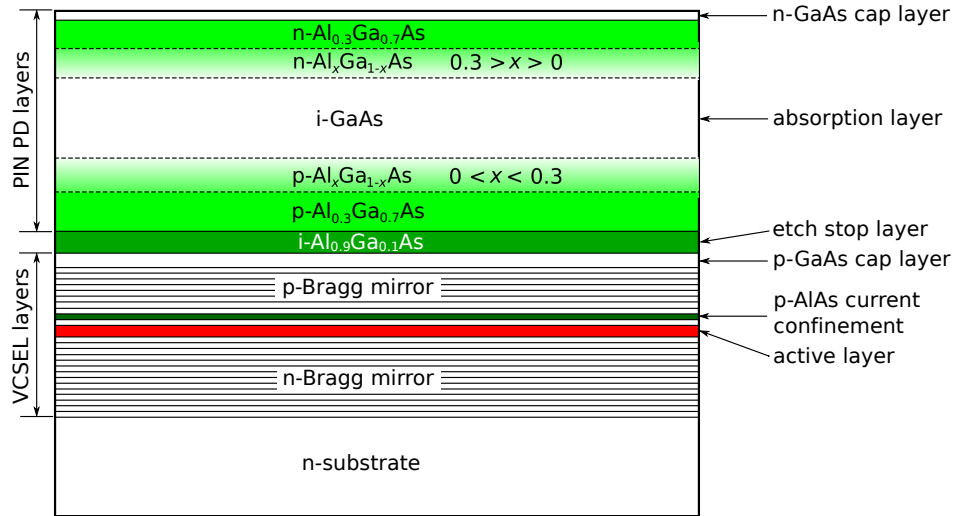


Fig. 2: Schematic layer structure of the transceiver chip. The layers for the PIN PD on top of the VCSEL layers are separated by an etch stop layer.

confinement after an oxidation step. The VCSEL growth is terminated with a 30 nm highly p-doped GaAs layer, which provides a low-resistance p-contact and at the same time prevents oxidation of the subjacent aluminum containing layers.

2.2 PIN PD

The PIN photodiode is grown on top of the intrinsic etch stop layer, which also partially acts as an insulator by reducing capacitive coupling between the two devices. The 1 μm thick undoped GaAs absorption layer is sandwiched by p- and n-doped $\text{Al}_{0.3}\text{Ga}_{0.7}\text{As}$. The higher bandgap energy of these two contact layers provides a window for the wavelengths of interest at around 850 nm. In order to minimize the energy band discontinuities between the absorption and contact layers, linearly graded n- and p- $\text{Al}_x\text{Ga}_{1-x}\text{As}$ ($x = 0 \rightarrow 0.3$) is employed, ensuring an easier escape of the light-induced carriers from the undoped GaAs. The 10 nm thick n-doped GaAs cap layer protects the subjacent $\text{n-Al}_{0.3}\text{Ga}_{0.7}\text{As}$ from oxidation.

2.3 Fabrication

The fabrication of transceiver chips is based on lithographic structuring with photosensitive resists and subsequent etching or material deposition steps. Seven to eight lithographic steps are necessary for the full processing of the transceiver chip shown in Fig. 3. In the first step, the detector layers on top of the VCSEL are removed by a selective reactive-ion etching (RIE) process. In order to ensure that the uppermost VCSEL layer is not affected by the etching, it is protected by an etch stop layer with a high aluminum content, as mentioned above. Combining dry-etching processes with SiCl_4 alone and with appropriate $\text{SF}_6/\text{SiCl}_4$ ratio, high etching selectivities between GaAs and $\text{Al}_x\text{Ga}_{1-x}\text{As}$

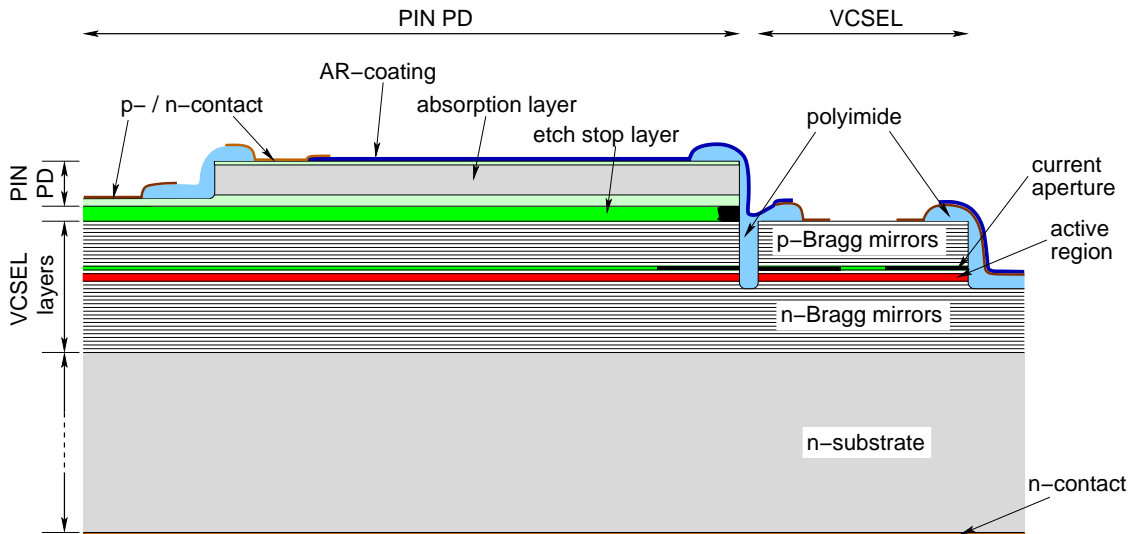


Fig. 3: Schematic layer structure of the transceiver chip. The layers for the PIN PD on top of the VCSEL layers are separated by an etch stop layer.

layers can be achieved [6], thus terminating the dry-etching on the $\text{Al}_{0.9}\text{Ga}_{0.1}\text{As}$ layer. Followed by a selective wet-etching with hydrofluoric acid, the highly p-doped cap layer of the VCSEL can now be exposed. Unlike, e.g., MSM PDs with planar contact structure, PIN PDs have vertically displaced contacts and thus require an additional etch step to expose the p-doped $\text{Al}_{0.3}\text{Ga}_{0.7}\text{As}$ layer, as can be seen in the left part of Fig. 3. With increased $\text{SF}_6/\text{SiCl}_4$ ratio, the selective dry-etching process can also be adapted to layers with lower aluminum content [6]. By means of the described selective etching techniques, a uniform layer topography all over the wafer can be guaranteed in spite of the intentional layer thickness inhomogeneity due to the epitaxial growth process. The third etching process spatially separates the VCSEL and the photodetector by a 2–4 μm narrow trench and gives access to the current confinement layer, as seen in the right part of Fig. 3. It is performed just with SiCl_4 without selectivity. Also this process step requires reactive-ion etching due to its steep mesa sidewalls, which are crucial for the miniaturization and dense integration of the VCSEL and PIN PD. Selective oxidation in a hot water vapor atmosphere forms the current aperture in the AlAs layer. An aluminum content of 90% in the 150 nm thick etch stop layer ensures only a moderate oxidation rate compared to the current confinement layer [7]. A deep oxidation of the etch stop layer associated with a volume change would induce strain in the surrounding layers, which could cause cracks and damage of the PD's edges after the subsequent annealing process for the n-contacts. On the other hand, a low aluminum content could result in a lower etching selectivity of the hydrofluoric acid. The fourth lithography step provides planarization and passivation with polyimide. Afterwards, both p- and n-contacts of the PD and VCSEL are evaporated and annealed, in order to form low-resistance contacts. As can be seen in the left part of Fig. 1, the bondpad arrangement of the PD allows testing with a microwave probe. The VCSEL is driven via the bondpad of the p-contact and the back side n-contact on the substrate. In the last lithography step, an Al_2O_3 quarter-wave antireflection (AR)

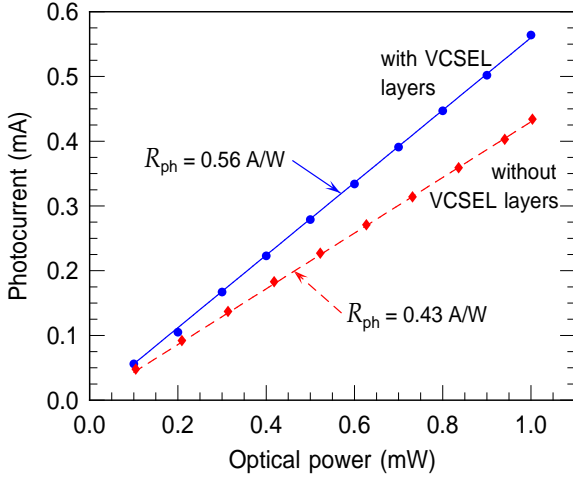


Fig. 4: Photocurrent of a PIN PD with 60 μm diameter biased at 3 V as a function of the incident optical power at 850 nm wavelength. The measurements were carried out with two samples with and without VCSEL layers underneath the PIN PD.

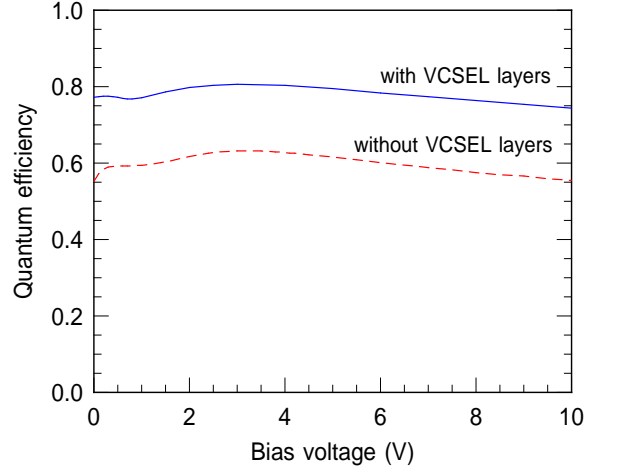


Fig. 5: Quantum efficiencies of PIN PDs from Fig. 4 dependent on the reverse bias voltage. The maximum quantum efficiency is achieved for both samples at a bias voltage of about 3 V.

layer is sputtered on the area of the transceiver chip which is exposed to incident light. The reflectivity of the semiconductor surface is thus reduced from approximately 30 % to 1.3 % over a spectral width of nearly 50 nm [5].

3. Device Measurements

3.1 Basic PIN PD characteristics

The VCSEL as well as the PIN photodiode are designed for operation at 850 nm. For photodiode characterization, the beam of a reference laser diode was focused on an AR-coated full-area circular photodetector with 60 μm diameter reverse biased at 3 V. Both the sample containing only the PIN layers and the sample including all transceiver layers, i.e., VCSEL and PIN PD, were used in order to study possible influences of the underlying VCSEL layers. In Fig. 4, the relation between the generated photocurrent I_{ph} and the corresponding incident optical power P_{opt} is shown. The power was varied with an optical attenuator in order to keep the operating current constant and thus to avoid a thermally induced wavelength drift of the reference laser. The responsivity

$$R_{\text{ph}} = \frac{I_{\text{ph}}}{P_{\text{opt}}} \quad (1)$$

of the two devices can be determined from the slope of the strongly linear curves. The device with only the PIN layers has a responsivity of 0.43 A/W. The theoretical value of 0.41 A/W is 5 % lower and includes only a simple single-pass absorption with an absorption coefficient of 9000 cm^{-1} for high-purity GaAs at 850 nm [8]. In this case, around 59 % of the

incident optical power is absorbed by the 1 μm thick GaAs absorption layer. The measured responsivity of the sample with a complete transceiver structure reaches 0.56 A/W. The 30 % higher responsivity arises from the subjacent VCSEL structure, where almost all of the non-absorbed intensity is reflected and thus passes the absorption region for a second time. The calculated responsivity of 0.57 A/W considers a simple double-pass absorption or just a single propagation through a twice as thick absorption layer and is a good approximation to the measured value. The higher measured value for the device with only the PIN layers could instead occur from a rather weak backreflection of the underlying structure, which was not considered in the calculation.

The responsivity of a photodetector introduced by (1) can also be expressed as

$$R_{\text{ph}} = \eta \frac{q}{h\nu} = \eta \frac{\lambda}{1.24 \mu\text{m}} \frac{\text{A}}{\text{W}}, \quad (2)$$

including its quantum efficiency η , Planck's constant h , the elementary charge q , the light frequency ν , and the wavelength λ . In Fig. 5, the quantum efficiency extracted from the photocurrent measurements according to (1) and (2) is presented as a function of the bias voltage. The dependence is indeed weak, nevertheless the maximum value of a quantum efficiency of 81 % for the sample with underlying VCSEL Bragg mirrors and 63 % for the photodiode with single-pass absorption is reached at around 3 V bias voltage. The quantum efficiency is [9]

$$\eta = (1 - R) \cdot (1 - \exp\{-\alpha d\}), \quad (3)$$

in which $R = 1.3\%$ is the reflection coefficient of the AR-coated PD [5], d the thickness of the absorption layer and $\alpha = 9000 \text{ cm}^{-1}$ the absorption coefficient of pure GaAs at 850 nm according to [8]. In (3) the absorption in the p- and n-regions of the PIN PD is neglected due to the higher bandgap of $\text{Al}_{0.3}\text{Ga}_{0.7}\text{As}$. The calculated value of about 82 % for the complete transceiver is close to the experimental data. The lower theoretical value of 59 % for the sample without the VCSEL layers could indicate a certain reflection of the non-absorbed light by the underlying p- and etch stop layer. The approach of single-pass absorption has to be taken with some care.

3.2 Basic VCSEL characteristics

The transmitting element of the transceiver chip is a standard top-emitting, oxide-confined, predominantly multimode VCSEL operating in the 850 nm wavelength range. For optimization and evaluation purposes, three VCSEL sizes were implied in the lithography mask design. The fully processed sample contains transceivers with different VCSEL mesa diameters of 22, 25, and 28 μm . For instance, Fig. 1 shows a transceiver chip with a 28 μm VCSEL and a 60 μm PD. The operation characteristics of the three VCSELs from the same sample, correspondingly having different oxide aperture diameters, are displayed in Fig. 6. Multimode operation is observed using devices with 7.8 and 4.5 μm oxide aperture with maximum optical output powers of 10.3 and 6.6 mW at thermal rollover, respectively. The smallest device with an oxide aperture of just 1.5 μm , on the other hand, shows single-mode operation with a maximum optical power of 1.9 mW. The

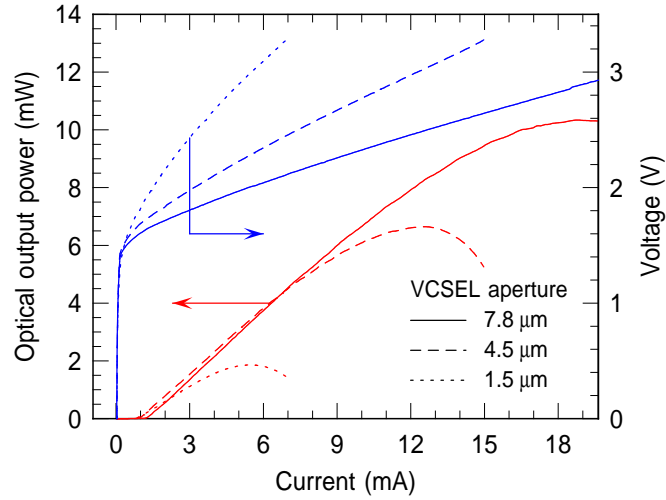


Fig. 6: Continuous-wave light–current–voltage characteristics of GaAs VCSELs with three different oxide aperture diameters at room temperature.

largest VCSEL has a threshold current of 1.3 mA and a differential quantum efficiency of 54 %. The device with a current aperture of 4.5 μm shows similar values of 1 mA and 51 %. In contrast, the smallest VCSEL has 1 mA threshold current but only 34 % differential quantum efficiency. Higher scattering losses at the oxide aperture are a likely reason. The differential resistances extracted by linear interpolation of the current–voltage characteristics at high operating currents are 235, 104, and 65 Ω for 22, 25, and 28 μm VCSEL mesas, respectively.

4. Conclusion

In this article, a new kind of monolithically integrated 850 nm wavelength transceiver chip has been presented for bidirectional optical data transmission over standard multimode fibers. The chips consist of PIN photodiodes and oxide-confined, top-emitting VCSELs, integrated to match 50 and 62.5 μm core diameter GI MMFs. The miniaturization versus previous generations of VCSEL/MSM PD chips requires the establishment of new fabrication processes and thus also new epitaxial layer designs. The crucial point of the seven lithography steps are the dry-etching processes, which define the PD plateau and expose the p-contact layer of the PIN photodetector and VCSEL. The etching selectivity for the $\text{Al}_x\text{Ga}_{1-x}\text{As}$ layers can be adjusted with an appropriate choice of the $\text{SF}_6/\text{SiCl}_4$ gas ratio in the RIE machine.

The PIN photodiode with 1 μm thick absorption layer has a responsivity of 0.43 A/W for single-pass absorption. For the complete transceiver layer structure, the responsivity is enhanced by 30 % to 0.56 A/W, which is due to the reflection of the non-absorbed light at the underlying VCSEL layers and thus a double-pass absorption. The quantum efficiency of the transceiver-type PIN PD is 81 %, whereas the single-pass PD has 63 %. Oxide-confined VCSELs with 7.8 μm current aperture diameter show maximum optical output powers of 10.3 mW, threshold currents below 1.3 mA, and 54 % differential quantum efficiency.

Investigations into the dynamic properties of complete transceiver chips are in progress. We expect a lot of room for improvements with optimized layer structures and processing. Half- and full-duplex data transmission experiments over different multimode fibers will be performed in the near future.

References

- [1] J.D. Ingham, R.V. Penty, and I.H. White, “Bidirectional multimode-fiber communication links using dual-purpose vertical-cavity devices”, *J. Lightwave Technol.*, vol. 24, pp. 1283–1294, 2006.
- [2] O. Sjölund, D.A. Louderback, E.R. Hegblom, J. Ko, and L.A. Coldren, “Individually optimized bottom-emitting vertical-cavity lasers and bottom-illuminated resonant photodetectors sharing the same epitaxial structure”, *J. Opt. A: Pure Appl. Opt.*, vol. 1, pp. 317–319, 1999.
- [3] A.M. Kasten, A.V. Giannopoulos, C. Long, C. Chen, and K.D. Choquette, “Fabrication and characterization of individually addressable vertical-cavity surface-emitting laser arrays and integrated VCSEL/PIN detector arrays”, in *Vertical Cavity Surface Emitting Lasers XI*, K.D. Choquette, J.K. Guenter (Eds.), Proc. SPIE 6484, pp. 64840C-1–6, 2007.
- [4] P. Kazlas, J. Wasserbauer, J. Scott, D. Paananen, S. Swirhun, and D. Lewis, “Monolithic vertical-cavity laser/p-i-n photodiode transceiver array for optical interconnects”, *IEEE Photon. Technol. Lett.*, vol. 10, pp. 1530–1532, 1998.
- [5] R. Michalzik, A. Kern, M. Stach, F. Rinaldi, and D. Wahl, “True bidirectional optical interconnects over multimode fiber”, in *Optoelectronic Interconnects and Component Integration IX*, A.L. Glebov, R.T. Chen (Eds.), Proc. SPIE 7607, pp. 76070B-1–17, 2010.
- [6] S. Salimian and C.B. Cooper, III, “Selective dry etching of GaAs over AlGaAs in SF₆/SiCl₄ mixtures”, *J. Vac. Sci. Technol. B*, vol. 6, pp. 1641–1644, 1988.
- [7] K.D. Choquette, R.P. Schneider, Jr., K.L. Lear, and K.M. Geib, “Low threshold voltage vertical-cavity lasers fabricated by selective oxidation”, *Electron. Lett.*, vol. 30, pp. 2043–2044, 1994.
- [8] H.C. Casey, Jr., D.D. Sell, and K.W. Wecht, “Concentration dependence of the absorption coefficient for *n*- and *p*-type GaAs between 1.3 and 1.6 eV”, *J. Appl. Phys.*, vol. 46, pp. 250–257, 1975.
- [9] K.J. Ebeling, *Integrated Optoelectronics*, Berlin: Springer-Verlag, 1993.

Heat-Sink Modules: Performance Enhancement for VCSEL Chips

Anna Bergmann and Rudolf Rösch

We present the layout development for a heat-sink module tailored for small-dimension laser chips. By means of improved heat dissipation, the laser characteristics are expected to be enhanced, which is important for example for a sufficient trapping performance when used as a laser source for optical traps. We show the requirements for the module parts as well as their assembly.

1. Introduction

We are using vertical-cavity surface-emitting laser (VCSEL) sources in optical traps [1]. Advantages are the vertical emission, a suitable emission wavelength of about 850 nm and the rather inexpensive fabrication of these lasers. Additionally, VCSELs can be arranged with very small pitch in almost arbitrary shaped arrays.

In recent studies, we have shown a particle sorting application where tilted linear VCSEL arrays are integrated underneath a microfluidic chip with a channel thickness of several tens of micrometers [2]. These VCSEL arrays are manufactured with a self-aligned surface relief process employing dry etching for steep vertical side walls [3].

After processing, the semiconductor material is cleaved into comparatively small pieces of 1.2 mm by 1.4 mm. These laser chips contain the important sorting cell as well as two neighboring cells to enable an easier handling of the chip and thus a protection of the lasers. However, due to the small dimensions of the laser chip, there was poor heat dissipation and consequently elevated temperatures in the semiconductor material. This led to limited output powers and an earlier thermal rollover. The trapping performance of the laser source is thus drastically degraded by these factors. For those reasons, it seemed necessary to incorporate a heat sink into the setup.

2. Future Setup With Microfluidic Chip and Heat Sink

The former concept for the integrated optical trap can be seen in Fig. 1. One cleaved laser chip is soldered to the polydimethylsiloxane (PDMS) microfluidic chip by indium bumps. Thin glass with back side fanout tracks seals the microfluidic channel. These fanout tracks enable addressing of the laser arrays.

However, operating the lasers in the described setup, we observed output powers between one fifth and almost one half of the output power measured on-wafer. This effect and

also the earlier thermal rollover are shown in Fig. 2 for comparison. Because of the strong degradation of the device performance due to poor heat dissipation, we decided to implement a heat sink.

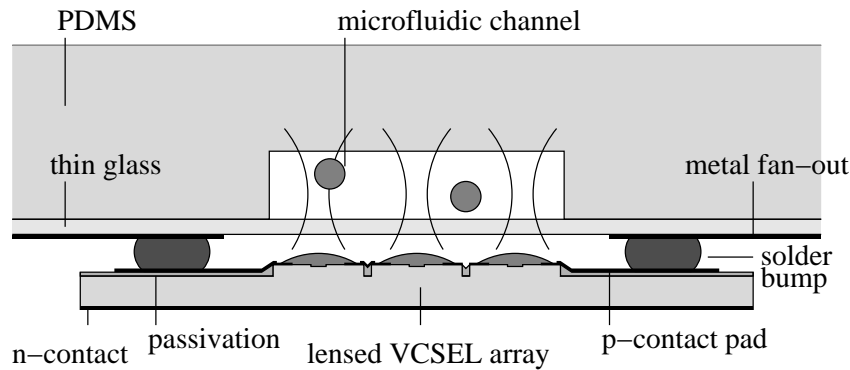


Fig. 1: Former concept of the integrated optical trap. The laser chip with on-facet microlenses is soldered by indium to the microfluidic chip which is sealed by thin glass. Contacting is achieved via lithographically structured metallization on the back side of the glass [1].

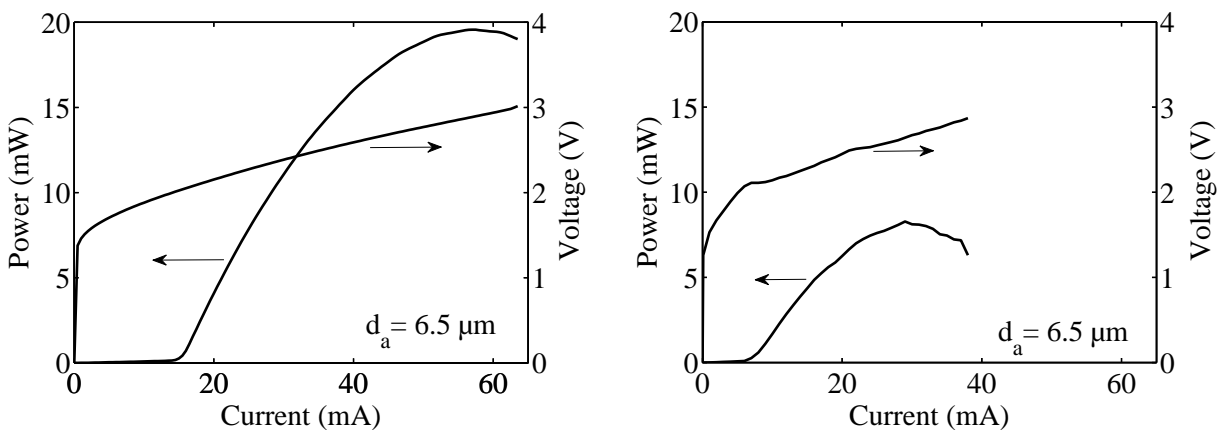


Fig. 2: Operation characteristics of an array with six lasers before (left) and after cleaving and integration (right). The active diameter of the devices is $6.5 \mu\text{m}$.

Figure 3 shows the new integrated setup. We are planning to solder-bond the laser chip onto a copper heat sink. The laser chip is surrounded by a glass sheet with an opening and a thickness similar to that of the chip. Fanout metallization is structured on the glass surface. This module is then attached to the microfluidic chip by an adhesive which cures when exposed to ultraviolet light. By mixing this adhesive with micrometer-sized spheres of different diameters, we can easily adjust the distance between heat sink and microfluidic chip and thereby prevent the microlenses on the laser facets from being impaired at the glass surface.

In the following we will introduce the different parts necessary for the proposed setup and finally the assembly.

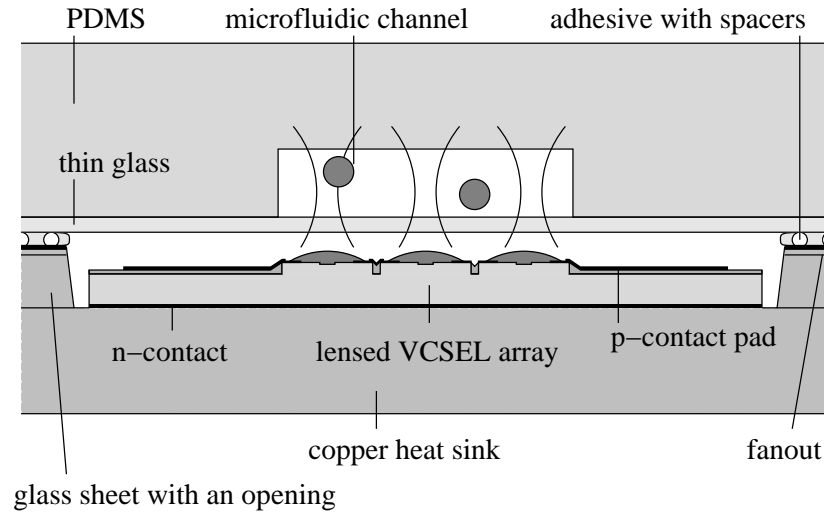


Fig. 3: Proposed concept of the integrated optical trap with the VCSEL array on a heat sink.

3. Heat-Sink Module: Components and Integration

3.1 Challenge: contacting of the embedded laser chip

The main difficulty when applying a heat sink as illustrated above is the contacting step. In the given approach, only very small distances between laser and microfluidic channel can be tolerated because we are dealing with small optical powers and an only weak focusing of the light in comparison to other trapping setups. To keep up with miniaturization, we use glass with a thickness of only $30\ \mu\text{m}$. Additionally we discarded to contact the lasers by wire bonding. Those wires would have a minimum diameter of $25\ \mu\text{m}$, resulting in a too large distance between lasers and microfluidic channel. Consequentially we chose the thinner contacting solution, namely lithographically structured fanout tracks on top of the planarized surface.

3.2 Heat-sink module: requirements on the copper part

Our present approach for the module design uses copper as a heat spreader. A rectangular piece of glass with an opening serves as the electrical insulation between copper and fanout metallization.

During high-temperature processing steps, the glass is subjected to mechanical stress caused by the mismatch of the thermal expansion coefficients. If the glass is mounted on a smaller area instead of the whole surface, this tension build-up is suppressed. Therefore we decided to elevate the glass bonding area in comparison to the rest of the heat sink surface. This area contains grooves for a facilitated glass bonding process, resulting from an improved outflow of the glue. Additionally, the heat sink contains an elevated frame for stronger mechanical support.

For some applications it is required to shift the laser chip from the center to the edge of the heat sink, particularly to enable a denser packing of various parts. For this reason,

the copper part contains a mounting area both in the center and at one of the edges. With this feature, the heat sink is usable in standard setups as well as in specialized ones. The whole copper material is able to serve as the back side contact for the laser arrays. This contact is realized by a hole for a wire in conjunction with a thread for a fixing screw. Figure 4 shows a drawing of the designed copper heat sink, satisfying all of the requirements mentioned above. One advantage is the usability for VCSEL array chips as well as for VCSEL chips with an extended cavity (called VECSEL chips here). Their semiconductor thicknesses are almost the same and their dimensions are rather similar.



Fig. 4: Left: Drawing of the designed copper heat spreader. Approximate dimensions are $18 \times 25 \text{ mm}^2$. Right: Images of the fabricated heat sinks with soldered laser chips.

Due to the bonding area at the edge, the copper heat spreader is not symmetric and the center of gravity is slightly off-center. This could have the shortcoming that spin-coating of photoresist is dangerous due to unbalanced centripetal forces.

3.3 Heat-sink module: requirements on the glass part

Glass is supposed to be the insulating material between copper and fanout metallization. By using glass, we are able to observe the glue distribution while conjoining copper with glass. Another advantage is the inexpensive and easy fabrication.

The very first requirement is a rectangular opening with dimensions in the same range as the laser chip. At two edges of this rectangle are additionally circular holes with $400 \mu\text{m}$ diameter. They enable an easier application of the glue into the gap between laser chip and glass, because it is slightly bigger than the outer diameter of the used cannulas. The glass slide thickness is similar to the semiconductor thickness. Again, the glass opening is suitable for both the VCSEL array and VECSEL chips.

Because it carries the electrical contacts, the glass sheet has to be long enough to be accessible even after attaching the microfluidic chip on top. The dimensions of the glass part will be around 4 cm length and 2.6 cm width.

3.4 Heat-sink module: fanout tracks

Using large glass plates is not enough. The fanout tracks must be long enough as well. That means new mask layouts have to be made, taking both centered and displaced setups

into account. In the centered setup, the laser chip will be mounted in the center with symmetric fanout tracks (Fig. 5), whereas in the displaced setup, the laser chip is shifted to the edge. The glass opening is also shifted, and the fanout tracks start from this point at the edge (Fig. 6).

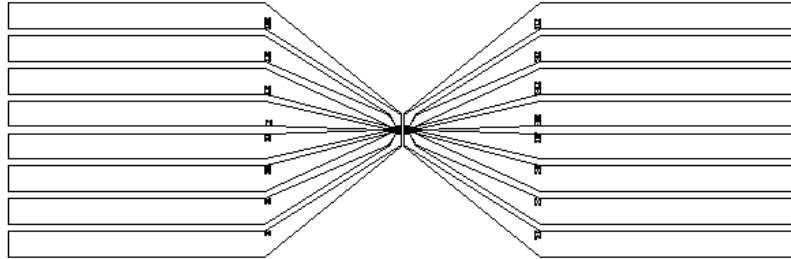


Fig. 5: Mask layout for common applications with the laser chip in the center of the heat-sink module. All fanout tracks start in the middle and have a length of approx. 3 cm.

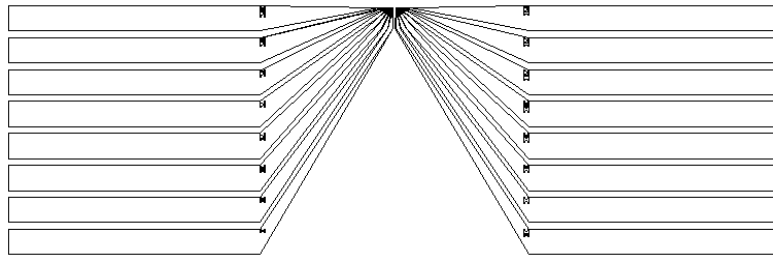


Fig. 6: Mask layout for specialized applications with the laser chip at the edge of the heat sink. All fanout tracks are accumulated at one side of the laser chip. Their length is about 3 cm.

3.5 Heat-sink module: assembly

The first step in the assembly process of the heat-sink module is the evaporation of indium onto the copper surface where the laser chip is supposed to be soldered. After soldering, the glass substrate is bonded to the copper carrying the soldered laser chip. In the next step, the gap between laser chip and glass is filled with a two-part adhesive through a cannula via compressed air.

For an improved adhesion of photoresist and metal we structure a polyimide layer above the filled gap. Polyimide needs a one-hour hard-bake step at 300 °C. This high temperature is one of the reasons for the stepped glass bonding area.

Afterwards we fabricate fanout tracks bridging the gap and reaching over the glass surface. For beam shaping, we apply integrated microlenses on top of the laser facets by reflow of cylindrical photoresist islands. Since the reflow is done at 250 °C, lens fabrication cannot be done prior to the polyimide curing.

The last assembly step consists of bonding the heat sink with lasers to the microfluidic chip, by a UV-curing adhesive mixed with spacers. Figure 7 shows a schematic of the complete assembly with microfluidic chip, long glass plate with fanout, and copper with soldered laser chip.

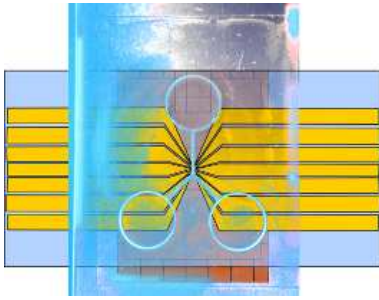


Fig. 7: Schematic of the complete heat-sink assembly. Clearly visible are the copper heat spreader with stepped areas and the long glass with fanout tracks. Attached on top is the microfluidic chip with channels in a Y-junction configuration.

4. Conclusion

Implementing copper as a heat spreader for the laser chip, the trapping performance is expected to improve considerably. The described heat-sink module can be applied in the integrated optical trap or similar integrated setups with small laser chip dimensions.

We have shown the layouts of the needed parts as well as the assembly of the complete module. All parts are designed in a way that they are suitable for both common and specialized applications, and also for similar types of laser chips.

References

- [1] R. Michalzik, A. Kroner, A. Bergmann, and F. Rinaldi, "VCSEL-based optical trapping for microparticle manipulation", in *Vertical-Cavity Surface-Emitting Lasers XIII*, K.D. Choquette, C. Lei (Eds.), Proc. SPIE 7229, pp. 722908-1–13, 2009.
- [2] A. Kroner, C. Schneck, F. Rinaldi, R. Rösch, and R. Michalzik, "Application of vertical-cavity laser-based optical tweezers for particle manipulation in microfluidic channels", in *Nanophotonics II*, D.L. Andrews, J.-M. Nunzi, A. Ostendorf (Eds.), Proc. SPIE 6988, pp. 69881R-1–12, 2006.
- [3] A. Kroner, "Optical particle manipulation by application-specific densely packed VCSEL arrays", *Annual Report 2007*, pp. 47–52. Ulm University, Institute of Optoelectronics.

Continuous-Wave Characteristics of MEMS Atomic Clock VCSELs

Ahmed Al-Samaneh and Dietmar Wahl

Vertical-cavity surface-emitting lasers (VCSELs) emitting at 894.6 nm wavelength have been fabricated for Cs-based atomic clock applications. For polarization control, a previously developed technique relying on the integration of a semiconducting surface grating in the top Bragg mirror of the VCSEL structure is employed. More specifically, we use a so-called inverted grating. The VCSELs are polarized orthogonal to the grating lines with no far-field diffraction side-lobes for sub-wavelength grating periods. Orthogonal polarization suppression ratios exceed 20 dB. The polarization stability has been investigated at different elevated substrate temperatures up to 80°C, where the VCSEL remains polarization-stable even well above thermal roll-over.

1. Introduction

Atomic clocks are stable frequency sources which provide enhanced accuracy and stability required for many recent civil and military applications ranging from communication systems to global positioning as well as synchronization of communication networks. Nowadays these applications are increasingly demanding frequency sources with long-term instabilities below 10^{-11} over one day, which cannot be afforded by quartz-based clocks. Hence, research into miniaturized atomic clocks has been initiated in particular in the United States of America [1], [2]. In 2008, the European Commission (EC) started to fund a collaborative research project within its seventh framework programme (FP7) for research and technological development to realize the first European miniature-size atomic clock. It is called *MEMS atomic clocks for timing, frequency control & communications* (MAC-TFC, www.mac-tfc.eu). The objective of MAC-TFC is to develop and demonstrate all necessary technology to achieve an atomic clock having a volume less than 10 cm^3 , a power consumption not exceeding 155 mW, and a short-term instability (Allan deviation) of 5×10^{-11} over one hour averaging interval. The proposed atomic clock is based on coherent population trapping (CPT), obtained in an extremely compact Cs-based vapor cell of a few cubic millimeters volume which is illuminated by a high-frequency modulated VCSEL [3].

VCSELs are compelling light sources for MEMS atomic clocks, since they simultaneously meet the requirements of 65 to 80°C temperature operation while emitting a low-noise, narrow-linewidth, single-mode, single-polarization beam with 894.6 nm wavelength under harmonic 4.6 GHz intensity modulation (as required for CPT using the Cs D1 line). Their sub-mA threshold currents are favorable for small power consumption, and hybrid integration with the clock microsystem is straightforward.

2. VCSEL Design and Fabrication

2.1 Layer structure

The VCSEL wafer was grown by solid source molecular beam epitaxy on an n-doped (100)-oriented GaAs substrate. Above the GaAs substrate, there is a 2 μm thick highly n-doped GaAs layer to allow n-contacting. The bottom n-type distributed Bragg reflector (DBR) consists of 38.5 $\text{Al}_{0.2}\text{Ga}_{0.8}\text{As}/\text{Al}_{0.9}\text{Ga}_{0.1}\text{As}$ layer pairs. The active region contains three compressively strained InGaAs quantum wells with 6 % indium content. Above the active region, there is a 30 nm thick AlAs layer for wet-chemical oxidation, required to achieve current confinement and lateral optical guiding of the laser radiation. To achieve single transverse mode laser oscillation, the active aperture formed by selective lateral oxidation is chosen to be 3 to 4 μm . A 25 $\text{Al}_{0.2}\text{Ga}_{0.8}\text{As}/\text{Al}_{0.9}\text{Ga}_{0.1}\text{As}$ layer pairs p-type DBR is grown on top of the AlAs layer. The DBRs are graded in composition and doping concentration for minimizing both the free-carrier absorption as well as the electrical resistance. Moreover, δ -doping is incorporated into the DBRs for improved performance of the VCSEL in terms of low threshold currents and high differential quantum efficiencies [4]. The structure has an additional topmost GaAs quarter-wave layer in which the so-called inverted grating is etched to achieve laser emission with a single polarization mode.

2.2 Grating design and fabrication

Polarization stability of the VCSEL emission is of a great interest for MEMS atomic clock applications. The polarization control technique applied in this work relies on the integration of a semiconducting surface grating in the top Bragg mirror of the VCSEL structure [5]. Compared to standard VCSELs, the fabrication of grating VCSELs involves just a few additional processing steps, namely the definition of the grating and its subsequent etching at the beginning of the fabrication sequence. Moreover, for a special grating VCSEL type, an extra topmost GaAs quarter-wave layer has to be grown. This layer serves as an antiphase layer, creating so-called inverted grating VCSELs [6]. The emission of these devices is polarized orthogonal to the grating lines. Compared to regular grating VCSELs, fabrication tolerances are much relaxed and quasi linearly polarized laser emission is obtained from devices with only moderately increased threshold current and no penalty in differential quantum efficiency and maximum output power. As a further advantage of inverted grating VCSELs, diffraction effects are strongly reduced [6]. Grating fabrication employs electron-beam lithography and wet-chemical etching using citric acid. Figure 1 displays the light outcoupling facet of an inverted grating VCSEL. The polarizing effect originates from the difference in optical losses (top mirror reflectivity) and thus threshold gains of modes polarized parallel or orthogonal to the grating lines. Surface gratings are easy to adapt to different devices, since the major grating parameters scale with the emission wavelength. Therefore the grating design parameters selected in this work are based on simulations and experimental results of VCSELs emitting in other wavelength regimes [6], [7]. Inverted gratings with quarter-wave etch depth, sub-wavelength grating periods (specifically 0.6 and 0.7 μm), and 50 % duty cycle have been employed. These grating parameters have shown the best performance in terms of

low threshold current, low diffraction loss, and high orthogonal polarization suppression ratio [6].

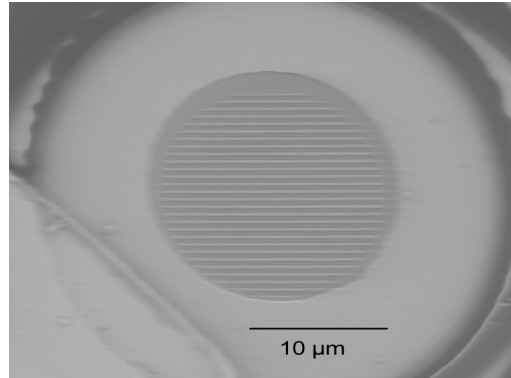


Fig. 1: Scanning electron micrograph of a fully processed surface grating VCSEL.

3. Characterization

The correct emission wavelength of 894.6 nm in the given case is the key selection parameter of VCSELs for MEMS atomic clocks. As mentioned above, the emission wavelength should be obtained at elevated ambient temperature and moderately high bias currents to guarantee a low power consumption and sufficient modulation bandwidth.

3.1 Operation characteristics and spectra

VCSELs having standard n-type substrate-side contacts have been successfully fabricated. Figure 2 (left) shows the light–current–voltage characteristics of a VCSEL with an active diameter of 4.4 μm. Its threshold current is lower than 0.5 mA. The continuous-wave spectrum at a current of 2.4 mA is illustrated in Figure 2 (right). The fundamental transverse mode is lasing at 894.6 nm. A higher-order mode is located on the short-wavelength side with a side-mode suppression ratio of more than 25 dB, which is large enough for the present application. Figure 3 shows the spectrum of another VCSEL with 3.3 μm active diameter. At an elevated temperature of 80 °C (as it might be expected in an integrated MEMS atomic clock) and a current of 4.7 mA, this device reaches the target wavelength with a side-mode suppression ratio of almost 40 dB.

3.2 Polarization control

In this subsection, we investigate the polarization stability of inverted grating VCSELs. Figure 4 (left) depicts the polarization-resolved light–current–voltage (PR-LIV) characteristics of a VCSEL with 4.1 μm active diameter, a grating period of 0.7 μm, and a grating depth of 60 nm. The dashed and dash-dotted lines represent the optical power measured behind a Glan–Thompson polarizer² whose transmission direction is oriented parallel and

²B. Halle GmbH, model PGT, long version, 60 dB extinction ratio

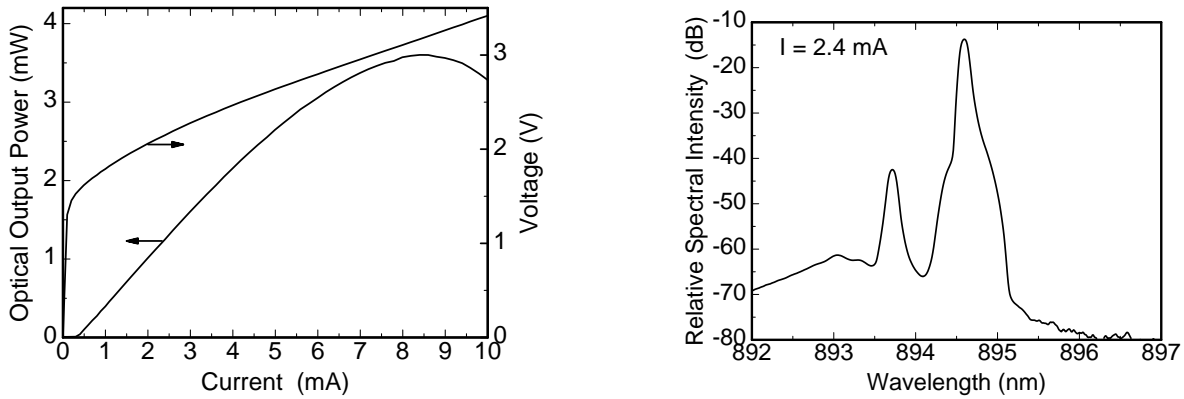


Fig. 2: Operation characteristics of an 895 nm VCSEL with 4.4 μm active diameter (left). Spectrum of the same VCSEL at 2.4 mA current and $T = 300$ K ambient temperature (right).

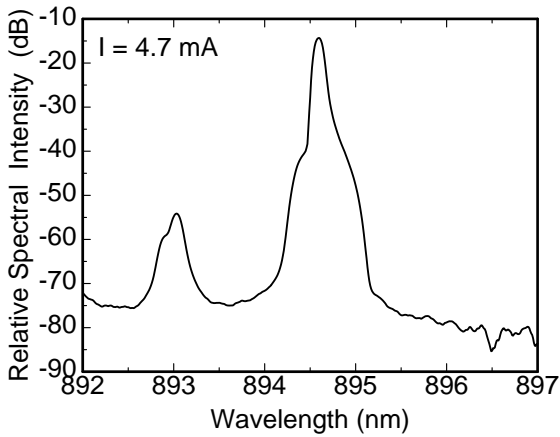


Fig. 3: Spectrum of a VCSEL with 3.3 μm active diameter at 4.7 mA current and $T = 80^{\circ}\text{C}$ ambient temperature.

orthogonal to the grating lines, respectively. The magnitude of the orthogonal polarization suppression ratio (OPSR) exceeds 20 dB for currents between 2.5 mA and thermal roll-over. Here, the OPSR is defined as the ratio between parallel and orthogonal output powers, namely

$$\text{OPSR} = 10 \cdot \log \left(\frac{P_{\text{parallel}}}{P_{\text{orthogonal}}} \right) \text{ dB} . \quad (1)$$

Since the VCSELs to be incorporated in MEMS atomic clock microsystems will experience high ambient temperatures (e.g., $T = 65^{\circ}\text{C}$), the polarization control introduced by surface gratings has been investigated under elevated temperature conditions. Figure 4 (right) shows PR-LI characteristics of a grating VCSEL with the substrate temperature varied between 20 and 80 $^{\circ}\text{C}$ in steps of 20 $^{\circ}\text{C}$. As can be seen, the grating VCSEL remains polarization-stable even well above thermal roll-over.

3.3 Far-field properties

For optimum light routing in the clock microsystem, it is important to know the beam properties of the VCSELs. The emission far-fields of a single-mode inverted grating

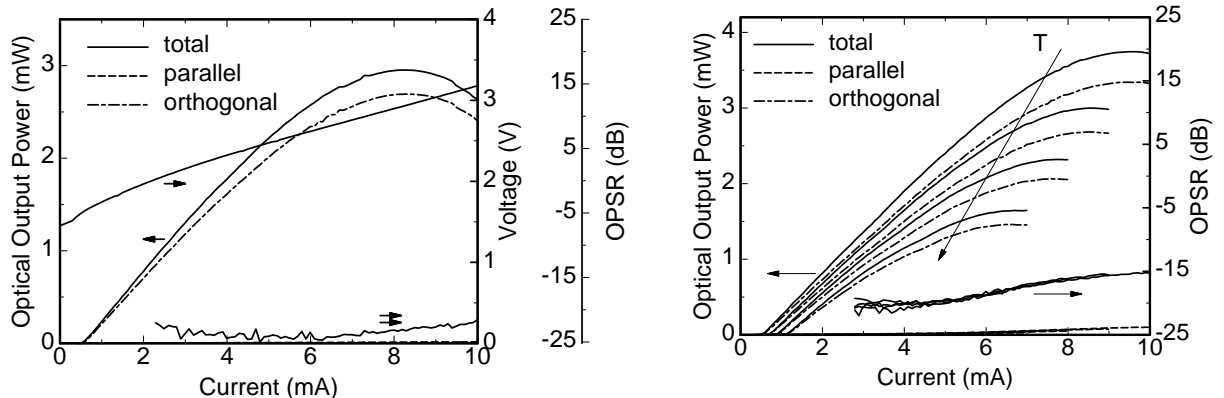


Fig. 4: Polarization-resolved operation characteristics of a grating VCSEL with $4.1\ \mu\text{m}$ active diameter at room temperature (left) and of a grating VCSEL with $4.4\ \mu\text{m}$ active diameter at substrate temperatures from 20 to $80\ ^\circ\text{C}$ in steps of $20\ ^\circ\text{C}$ (right). For both VCSELs, the surface grating has $60\ \text{nm}$ grating depth, $0.7\ \mu\text{m}$ grating period, and 50% duty cycle. The quasi-vertical arrow in the right figure points towards higher temperature.

VCSEL with an active diameter of about $3.6\ \mu\text{m}$ parallel and orthogonal to the grating lines are shown in Fig. 5. Both far-fields are almost identical, indicating an almost perfectly circular beam shape. There are no emission side-lobes, which proves the absence of diffraction effects by the sub-wavelength grating.

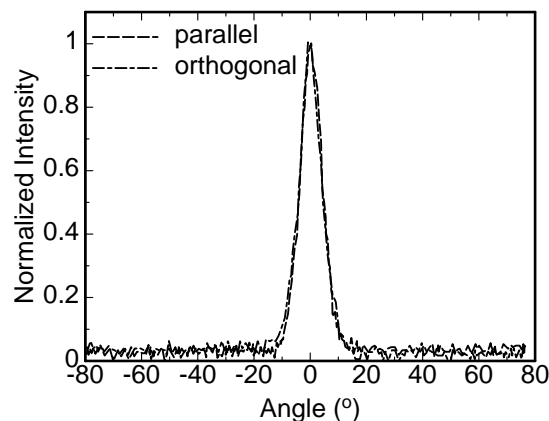


Fig. 5: Far-fields of an inverted grating VCSEL measured orthogonal and parallel to the grating lines at $4\ \text{mA}$ bias. The laser has an active diameter of $3.6\ \mu\text{m}$. The grating period is $0.6\ \mu\text{m}$, the grating depth is $60\ \text{nm}$, and the duty cycle is 50% .

4. Conclusion

We have reported the fabrication and characterization of $894.6\ \text{nm}$ VCSELs to be incorporated in Cs-based MEMS atomic clocks. The main requirements on the lasers, such as correct emission wavelength, single-mode, single-polarization emission, low threshold currents, and high-temperature operation have been successfully met. For polarization

control, inverted gratings have been employed. The VCSELs are polarized orthogonal to the grating lines with sufficient suppression of the competing polarization and no far-field diffraction side-lobes for sub-wavelength grating periods. At elevated substrate temperatures, the VCSELs remain polarization-stable even well above thermal roll-over.

5. Acknowledgments

The authors thank Y. Men for performing the electron beam lithography. They wish to thank S. Renz, A. Strodl, and D.S. Setz for their help in the processing and characterization. A very special thanks goes to Pierluigi Debernardi for the invention of the surface grating technique employed in this work and numerous simulations done in the past. Funding by the EC within its seventh framework programme (FP7) under grant agreement number 224132, project MAC-TFC is acknowledged.

References

- [1] R. Lutwak, J. Deng, W. Riley, M. Varghese, J. Leblanc, G. Tepolt, M. Mescher, D.K. Serkland, K.M. Geib, and G.M. Peake, “The chip-scale atomic clock – low-power physics package”, in Proc. *36th Annual Precise Time and Time Interval (PTTI) Meeting*, pp. 339–354. Washington DC, USA, Dec. 2004.
- [2] S. Knappe, V. Shah, P. Schwindt, L. Hollberg, J. Kitching, L.A. Liew, and J. Moreland, “A microfabricated atomic clock”, *Appl. Phys. Lett.*, vol. 85, no. 9, pp. 1460–1462, 2004.
- [3] C. Gorecki, M. Hasegawa, N. Passilly, R.K. Chutani, P. Dziuban, S. Gailliou, and V. Giordano, “Towards the realization of the first European MEMS atomic clock”, in Proc. *2009 IEEE/LEOS International Conference on Optical MEMS and Nanophotonics*, pp. 47–48. Clearwater, FL, USA, Aug. 2009.
- [4] D. Wahl, D. Setz, and A. Al-Samaneh, “Development of VCSELs for atomic clock applications”, *Annual Report 2008, Institute of Optoelectronics, Ulm University*, pp. 49–54, 2008.
- [5] R. Michalzik, J.M. Ostermann, and P. Debernardi, “Polarization-stable monolithic VCSELs” (invited), in *Vertical-Cavity Surface-Emitting Lasers XII*, C. Lei, J.K. Guenter (Eds.), Proc. SPIE 6908, pp. 69080A-1–16, 2008.
- [6] J.M. Ostermann, P. Debernardi, and R. Michalzik, “Optimized integrated surface grating design for polarization-stable VCSELs”, *IEEE J. Quantum Electron.*, vol. 42, no. 7, pp. 690–698, 2006.
- [7] J.M. Ostermann, F. Rinaldi, P. Debernardi, and R. Michalzik, “VCSELs with enhanced single-mode power and stabilized polarization”, *IEEE Photon. Technol. Lett.*, vol. 17, no. 11, pp. 2256–2258, 2005.

Structured SiN-masks for Self Separation of Full 2"-GaN Wafers by Hydride Vapor Phase Epitaxy

Frank Lipski

Using a dielectric mask structured by optical lithography, freestanding 2"-GaN wafers were prepared by hydride vapor phase epitaxy (HVPE) and self separation during cooldown. The mask was deposited on a GaN template grown on sapphire by metal organic vapor phase epitaxy (MOVPE). We found that the instability of the SiN mask at growth temperature supports the further self-separation. Testing different mask geometries, a hexagonally shaped pattern with a period of 30 μm and an opening of 3 μm showed best performance. This mask allowed the growth and separation of a full 2" GaN wafer by utilizing the stress arising during cooldown from thermal mismatch to the substrate. The thickness inhomogeneity is below 10 % and the samples show good surface morphology.

1. Introduction

Unlike other established semiconductor material systems, nowadays GaN technology is based on heteroepitaxy on foreign substrates due to missing GaN bulk crystals. While the ammonothermal growth showed good progress for the fabrication of these demanded substrates in the last years [1,2], hydride vapor phase epitaxy (HVPE) is still considered as the most promising tool. Nevertheless HVPE growth of thick GaN samples is a challenge. It is mostly a heteroepitaxial process, where large strain is generated on one side by lattice mismatch of the foreign substrate material to GaN and on the other side by the large mismatch of the respective thermal expansion coefficients yielding to severe bowing and often to strong cracking of the grown samples. In order to reduce strain and bowing in the final quasi-substrate, a removal technique of the foreign substrate from the grown GaN layer is required. Many approaches towards that challenge were reported in literature, such as laser-lift-off (LLO) [3], mechanical polishing for substrate removal [4] or growth on etchable substrates like GaAs or ZnO [5,6]. A self-evident technique is the use of stress arising during cooldown for the separation. Many publications describe such an approach [7,8], nevertheless it is a difficult process as it requires some kind of interlayer in the epitaxial structure for separation. On one hand, such a layer should weaken the interface, on the other hand, most of the stress during cooldown should arise exactly at this position, otherwise the cracking may occur at an undefined position in the crystal. And finally there is the need to find a compromise of weak connection and good material quality in the GaN grown above the interlayer. This seems to be very critical e.g. for low temperature interlayers [9].

In this work we used dielectric masks, structured by optical lithography and dry etching by an ex-situ process. This idea was originally used for defect reduction by epitaxial

lateral overgrowth (ELOG) being nowadays fairly well established, and is also applied for self-separation [10]. This method is well reproducible, in particular compared to most of the in-situ deposited interlayers. The material quality of the overgrown layer above the mask is excellent and the method also allows full control on the mask pattern and hence on the strength of the connection.

2. Experimental

The HVPE growth was performed in a commercial Aixtron single-wafer HVPE system with a horizontal quartz-tube, heated in a furnace with five zones. A 1:1 mixture of nitrogen and hydrogen was used as carrier gas, as it showed best performance regarding cracking [11]. Ammonia was applied as nitrogen precursor, while for the group-III element GaCl was used, formed inside the reactor by streaming HCl gas over a liquid Ga source heated to 850 °C. The used showerheads for the GaCl injection together with the carrier gas flows were carefully adjusted to reduce parasitic deposition as much as possible. The temperature and pressure for the GaN growth were kept constant at 1050 °C and 900 hPa respectively. In order to improve the surface morphology, the V/III-ratio, pressure and growth rate were changed during the last few micrometers of the growth. Details of this procedure can be found elsewhere [12]. The growth was started at a fairly low growth rate of about 10 $\mu\text{m}/\text{h}$ with a high V/III-ratio to pronounce lateral growth and then changed up to 100 $\mu\text{m}/\text{h}$.

The HVPE-growth was performed on 2 μm thick GaN template layers grown in an Aixtron 200/4 RF-S MOVPE system on (0001) sapphire wafers with a thickness of 430 μm and a diameter of 2". The substrates had a miscut of 0.3° towards the a-plane, yielding to an improved surface morphology [12]. For defect-reduction an in-situ SiN-layer was deposited during the growth of the GaN template [13]. Such templates are strongly compressively strained and allow crack-free growth of comparably thick HVPE layers more easily. On these templates, a 200 nm thick SiN or SiO₂ layer was deposited by plasma enhanced chemical vapor deposition (PECVD) and structured by optical lithography and dry etching. We investigated several different patterns for these studies.

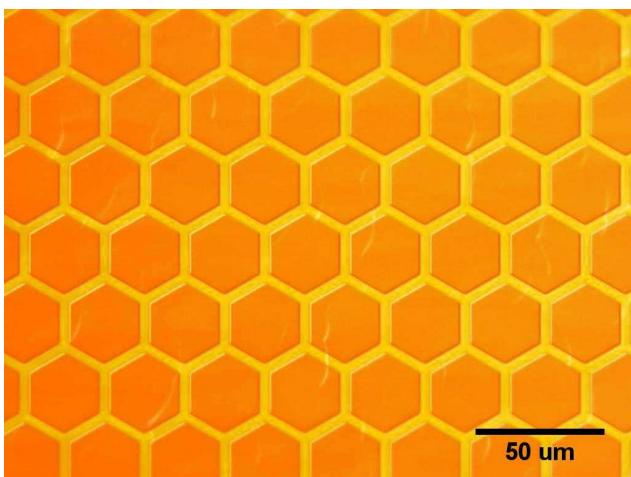


Fig. 1: Honeycomb pattern where the masked area is hexagonally shaped. The period of the mask is varied between 15 μm and 100 μm .

The first one is a simple stripe pattern with masked stripes of a width of 8 μm and an opening of 3 μm in between. The stripes are aligned along the $\langle 1\bar{1}00 \rangle$ -direction. The second pattern is hexagonally shaped like a honeycomb with open trenches between masked hexagons (Fig. 1). For this pattern the size of mask and trench were varied, see table 1. Again, the trenches run along the $\langle 1\bar{1}00 \rangle$ -direction of GaN.

After locally removing the mask by dry etching, the samples were put back into the MOVPE system to initiate lateral growth starting from the open trenches in the mask partly covering the masked area. This growth step starts at fairly low temperature and low V/III-ratio corresponding to a 3D growth mode. The patterns formed in this step having triangular cross-sections were afterwards overgrown with increased temperature and increased V/III-ratio for a more lateral growth over the masked areas. Although the masked area is not completely closed during this step, it helps to achieve a closed layer at an early stage in the HVPE growth.

3. Results and Discussion

3.1 Mask material

First, the applicability of SiO_2 and SiN as masking interlayer for a subsequent self-separation were investigated. Therefore, two samples were prepared with the same stripe pattern and then overgrown using the same conditions in MOVPE and HVPE with an about 300 μm thick GaN layer. On both samples, self-separation during cool-down could be observed. However, only the one with the SiN -mask separated at the prepared interlayer. Obviously, the SiN mask dissolves during HVPE growth, additionally leading to a dissolution of the nearby GaN, resulting in big cavities in the GaN buffer. In Fig. 2 a SEM-picture of the cross-section of this sample is shown. The position of the former mask can be identified by the big void due to a late coalescence of the overgrown layer. Mainly the GaN buffer below the mask is partly dissolved while the buffer below the former opening is not attacked. In contrast to the sample with SiO_2 -mask, horizontal cracks were only observed at the mask position. SiO_2 is much more stable compared to SiN . Hence mask and GaN buffer of the SiO_2 masked sample survive the HVPE growth unharmed. Instead of a separation on the mask, horizontal cracks about 20 μm above developed as consequence of the high stress due to the thermal mismatch of sapphire and GaN during cooldown.

Obviously, the dissolution of the mask together with the GaN nearby is essential for the separation. A sample, where the SiO_2 -mask material was removed after the second MOVPE step resulting in cavities where the grown triangular overlaps the former mask due to a less pronounced lateral growth in HVPE, showed the same behavior as for remaining SiO_2 . Again, horizontal cracks appeared above the cavities (see Fig. 3). These horizontal cracks also lead to self separation and freestanding GaN, but in a fairly uncontrolled random process. These samples also show several vertical cracks yielding to only small pieces of GaN instead of a full free-standing wafer.

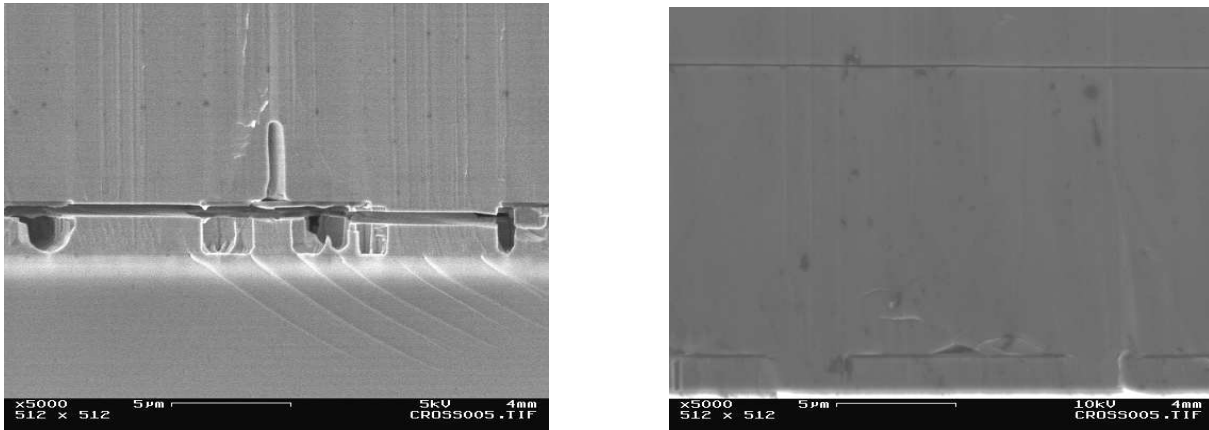


Fig. 2: Cross section SEM pictures after HVPE growth of about $300\ \mu\text{m}$. The left picture shows the SiN mask which dissolved and also attacked the GaN directly below the mask. The mask position is indicated by the vertical cavity due to a late coalescence of the overgrown GaN. The right picture shows the growth on a SiO₂ mask. The mask material and the GaN nearby is still stable, but a horizontal crack about $20\ \mu\text{m}$ above the mask developed.

3.2 Mask pattern

Freestanding GaN-pieces that were produced with the stripe pattern showed a strong asymmetric (concave) bow with a curvature of $1100\ \text{km}^{-1}$ and $1550\ \text{km}^{-1}$ parallel and orthogonal to the stripes, respectively. In order to suppress this asymmetric bowing, we investigated the honey-comb like pattern as described above (see Fig. 1). In order to optimize the separation properties, the ratio between masked and open area was varied keeping the opening width constant at $3\ \mu\text{m}$ thus changing the filling factor FF, i.e. the ratio of the masked to open area (table 1). We expected a better separation for a larger FF. For a $200\ \mu\text{m}$ thick GaN layer no separation was achieved for the $15\ \mu\text{m}$ period sample. The $30\ \mu\text{m}$ period showed full separation, although the GaN layer broke into several pieces due to the comparably low layer thickness. However, for the larger periods of $60\ \mu\text{m}$ and $100\ \mu\text{m}$, it was not possible to get a closed layer during the HVPE growth. To increase the FF at still acceptable period length, we have reduced the width of the openings to

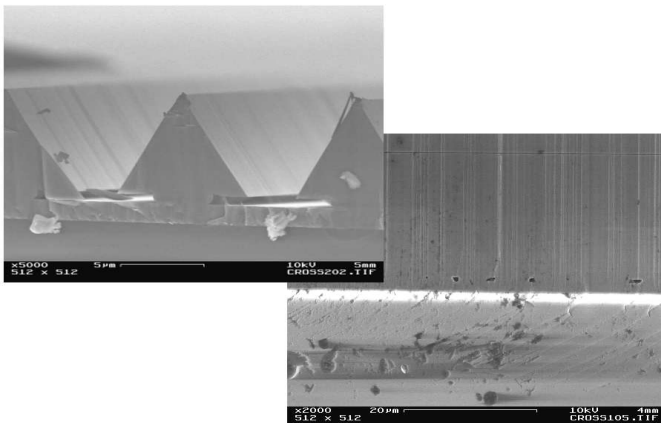


Fig. 3: SEM picture of a sample where the SiO₂ was removed after the second MOVPE step (left). The part, that is overgrown over the former mask will remain as cavity after the HVPE growth. The right picture shows a crosssection after HVPE growth. Similar to samples where the SiO₂ was not removed, horizontal cracks above the inter-layer developed and are visible in the SEM picture.

1.5 μm . This lead to a slightly improved separation. However, as this is at the limit of our optical lithography, further experiments were done with 3 μm openings.

We also observed that the separation does not depend on the layer thickness if a thickness of about 200 μm is exceeded. However, a larger thickness is needed to avoid vertical cracking of the GaN layer during separation.

Table 1: Ratio of masked to open area (FF) for different patterns.

Pattern	Trench width	Period	Filling factor (FF)
stripe	3 μm	8 μm	72%
hexagon	3 μm	15 μm	64%
hexagon	3 μm	30 μm	81%
hexagon	3 μm	60 μm	90%
hexagon	3 μm	100 μm	94%
hexagon	1.5 μm	30 μm	90%

3.3 Properties of separated GaN-wafers

In Fig. 4 a photograph of an about 1.5mm thick separated GaN wafer is shown with a thickness inhomogeneity of only 10%. Such a thickness is actually the limit of our HVPE system due to parasitic depositions inside the reactor. It has a very smooth surface (Fig. 5).

All separated samples exhibit a concave bow depending on the total layer thickness. The bow of the 1.5 mm thick sample was determined by HRXRD measurement to be 277 km^{-1} while a thinner sample with half the thickness showed a bow of 750 km^{-1} .



Fig. 4: Photograph of a full 2" GaN wafer self-separated during cool-down by growth on the hexagonally shaped mask with a period of 30 μm . The thickness of the wafer is about 1.5 mm.

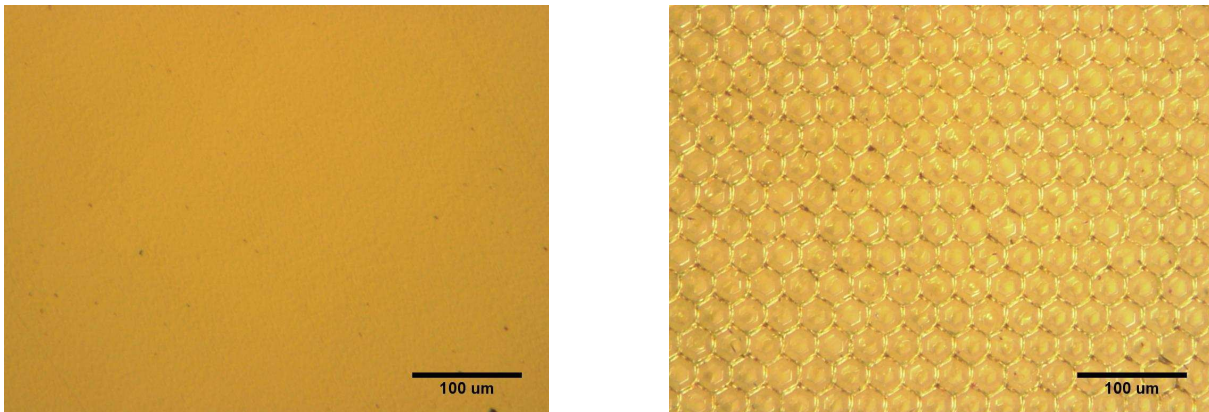


Fig. 5: Optical microscopy photograph with Nomarski contrast of the free-standing self-separated GaN layer. The surface is very smooth (left). On the backside (right), the mask structure is still observable, proving that separation happened on that interlayer.

The quality of the layer was further investigated by PL and HRXRD measurements. The full width at half maximum (FWHM) of the (002)- and (102)-reflections are 75 arcsec and 230 arcsec, respectively.

The position of the donor bound exciton (D^0X) at 3.470 eV measured by low temperature photoluminescence with a HeCd-laser as excitation (Fig. 6) indicates a strain free surface. The FWHM of less than 1 meV for the D^0X shows the good quality. The dislocation density determined by a chemical etching method, where we used hot HCl-gas and atomic force microscopy [14] was below $1 \cdot 10^6 \text{ cm}^{-2}$. By room temperature Hall measurement we determined a carrier mobility of $740 \text{ cm}^2/\text{Vs}$ and a carrier concentration of $6 \cdot 10^{16} \text{ cm}^{-3}$.

4. Conclusion

Full 2"-wafers of freestanding GaN of high quality were fabricated by a self-separation process during cool-down by an inserted dielectric mask. It was found that SiN as mask material dissolves at the chosen temperature in HVPE and leads to cavities in the GaN-buffer below, strongly enhancing the self-separation process and making the production of crack-free freestanding GaN wafers possible.

Acknowledgments

We like to thank M. Feneberg of the Institute of Semiconductor Physics, Ulm University for PL measurements. Technical support provided by I. Argut is also gratefully acknowledged. This work was financially supported by Freiberger Compound Materials GmbH, Freiberg and the German Federal Ministry of Education and Research under contract 01BU0620.

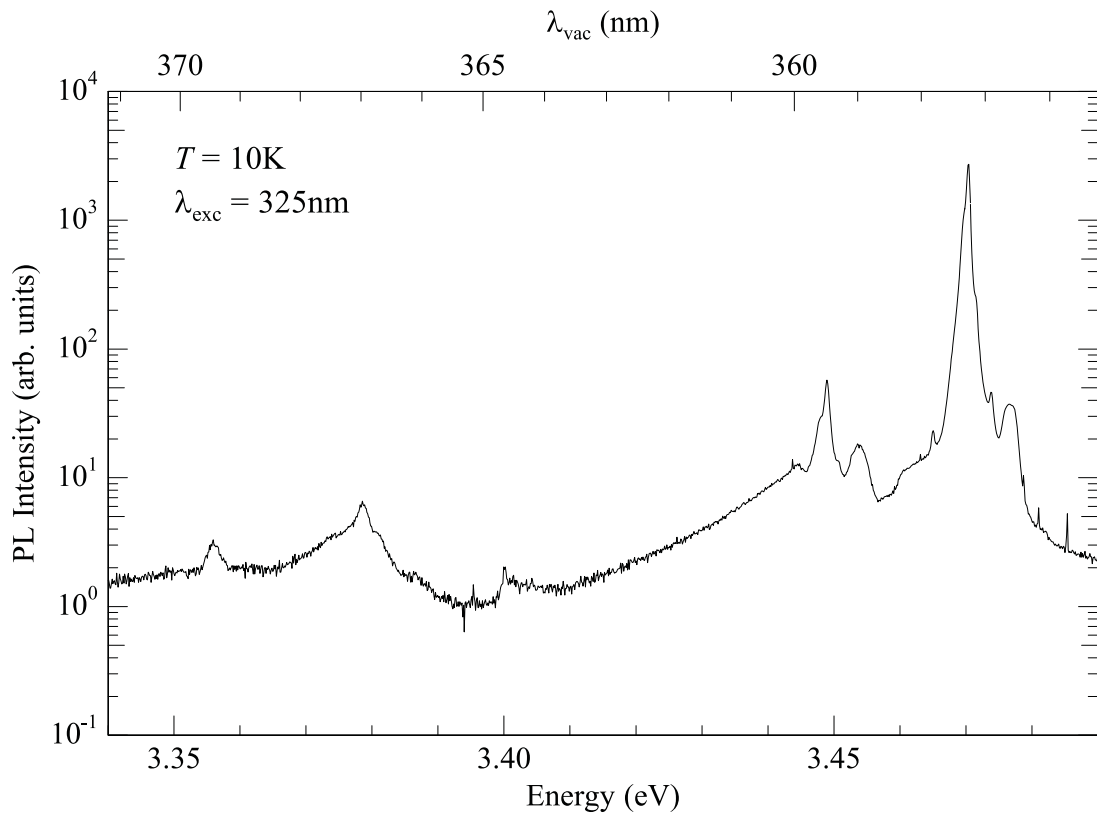


Fig. 6: Low temperature (10 K) PL spectrum of a freestanding sample, grown on the hexagonal mask with a period of 30 μm .

References

- [1] T. Fukuda and D. Ehretraut, "Prospects for the ammonothermal growth of large GaN crystal", *J. Cryst. Growth*, vol. 305, pp. 304–310, 2007
- [2] R. Dwilinski, R. Doradzinski, J. Garczynski, L. P. Dierzputowski, A. Puchalski, Y. Kanbara, K. Yagi, H. Minakuchi, and H. Hayashi, "Excellent crystallinity of truly bulk ammonothermal GaN", *J. Cryst. Growth*, vol. 310, pp. 3911–3916, 2008
- [3] C.R. Miskys, M.K. Kelly, O. Ambacher, and M. Stutzmann, "Freestanding GaN-substrates and devices", *phys. stat. sol. (c)*, vol. 0, pp. 1627–1650, 2003.
- [4] S. Nakamura, M. Senoh, S. Nagahama, N. Iwasa, T. Yamada, T. Matusushita, H. Kiyoku, Y. Sugimoto, T. Kozaki, H. Umemoto, M. Sano, and K. Chocho, "InGaN/GaN/AlGaIn-based laser diodes with cleaved facets grown on GaN substrates", *Appl. Phys. Lett.*, vol. 73, pp. 832–834, 1998.
- [5] K. Motoki, T. Okahisa, N. Matsumoto, M. Matsushima, H. Kimura, H. Kasai, K. Takemoto, K. Uematsu, T. Hirano, M. Nakayama, S. Nakahata, M. Ueno, D. Hara, Y. Kumagai, A. Koukitu, and H. Seki, "Preparation of Large Freestanding GaN Substrates by Hydride Vapor Phase Epitaxy Using GaAs as a Starting Substrate", *Jpn. J. Appl. Phys.*, vol. 40, pp. L140–L143, 2001.

- [6] F. Lipski, S.B. Thapa, J. Hertkorn, T. Wunderer, S. Schwaiger, F. Scholz, M. Feneberg, M. Wiedenmann, K. Thonke, H. Hochmuth, M. Lorenz, and M. Grundmann, “Studies towards freestanding GaN in hydride vapor phase epitaxy by in-situ etching of a sacrificial ZnO buffer layer”, *phys. stat. sol. (c)*, vol. 6, pp. S352–S355, 2009.
- [7] Y. Oshima, T. Eri, M. Shibata, H. Sunakawa, K. Kobayashi, T. Ichihashi, and A. Usui, “Preparation of Freestanding GaN Wafers by Hydride Vapor Phase Epitaxy with Void-Assisted Separation”, *Jpn. J. Appl. Phys.*, vol. 42, pp. L1–L3, 2002
- [8] S. Bohyama, H. Miyake, K. Hiramatsu, Y. Tsuchida, and T. Maeda, “Freestanding GaN Substrate by Advanced Facet-Controlled Epitaxial Lateral Overgrowth Technique with Masking Side Facets”, *Jpn. J. Appl. Phys.*, vol. 44, pp. L24–L26, 2004
- [9] Yi. V. Zhilyaev, A. V. Nasonov, S.D. Raebksi, S.N. Roding, M.O. Shcheglov, and V. Yu. Davydov, “Bulk gallium nitride: preparation and study of properties”, *phys. stat. sol. (a)*, vol. 195, pp. 122–126, 2003.
- [10] C. Hennig, E. Richter, M. Weyers, and G. Tränkle, “Self-separation of thick two inch GaN layers grown by HVPE on sapphire using epitaxial lateral overgrowth with masks containing tungsten”, *phys. stat. sol. (c)*, vol. 4, pp. 2638–2641, 2007.
- [11] E. Richter, C. Hennig, M. Weyers, F. Habel, J.D. Tsay, W.Y. Liu, P. Brückner, F. Scholz, Y. Makarov, A. Segal, and J. Kaeppler, “Reactor and growth process optimization for growth of thick GaN layers on sapphire substrates by HVPE”, *J. Cryst. Growth*, vol. 277, pp. 6–12, 2005.
- [12] P. Brückner, F. Habel, and F. Scholz, “HVPE growth of high quality GaN layers”, *phys. stat. sol. (c)*, vol. 3, pp. 1471–1474, 2006.
- [13] J. Hertkorn, F. Lipski, P. Brückner, T. Wunderer, S.B. Thapa, F. Scholz, A. Chuvilin, U. Kaiser, M. Beer, and J. Zweck, “Process optimization for the effective reduction of threading dislocations in MOVPE grown GaN using in situ deposited SiN masks”, *J. Cryst. Growth*, vol. 310, pp. 4867–4870, 2008.
- [14] F. Habel and M. Seyboth, “Determination of dislocation density in epitaxially grown GaN using an HCl etching process”, *phys. stat. sol. (c)*, vol. 0, pp. 2448–2451, 2003.

Investigations of HVPE grown Nonpolar a-plane GaN on Slightly Misoriented r-plane Sapphire Substrates

Stephan Schwaiger

We have investigated the growth of nonpolar GaN templates by hydride vapor phase epitaxy (HVPE). This includes a systematic study of misoriented r-plane sapphire wafers with a miscut angle up to $\pm 1^\circ$ towards the c-axis of the crystal as starting substrates. Starting with an AlN nucleation layer approximately $3.3\mu\text{m}$ of nonpolar a-plane GaN are grown by metalorganic vapor phase epitaxy (MOVPE). The subsequent growth by HVPE was optimized to obtain flat and homogeneous layers with very good crystal quality. This was illustrated by very small full widths at half maximum (FWHM) of x-ray rocking curve (XRC) measurements of less than 500 arcsec. The surface quality was evaluated by scanning electron microscopy (SEM) and optical phase contrast microscopy showing a high number of surface defects (pits) for the samples with a high miscut towards the positive direction whereas a slight miscut of $+0.5^\circ$ reduces the surface roughness. Additionally, smallest XRC FWHM values have been obtained for this particular miscut. A miscut towards negative directions results in lower crystalline quality and the surfaces shows hillock-like features. All GaN layers on misoriented substrates are tilted with respect to the substrate. Their tilt angle increases with the miscut angle. Its direction is opposed to the miscut of the sapphire.

1. Introduction

Currently, commercially available devices based on the nitrides, like light emitting diodes, are typically grown along the crystallographic c-direction. Unfortunately, huge piezoelectric fields are present within respective heterostructures, because of the lattice geometry and the induced strain. The resulting effects are mostly summarized as the quantum confined Stark effect [1]. One negative consequence is the reduced carrier recombination probability in quantum wells (QWs) [2]. To get rid of these negative effects, growth in nonpolar or semipolar direction is investigated by many groups. Typical nonpolar directions are a $[11\bar{2}0]$ and m $[10\bar{1}0]$. Due to the lack of real bulk GaN, the structures have to be grown either on foreign substrates like e.g. r-plane sapphire leading to a-plane GaN [3], or m-plane SiC [4] or LiAlO₂ [5] which results in m-plane GaN. However, the resulting material grown in those unusual directions typically contains a high number of defects. Other groups use sliced pieces from hydride vapor phase epitaxially (HVPE) grown GaN as starting substrates [6] resulting in a drastic reduction of the defect density. However, only small sized wafers of a few square millimeters are nowadays available for extremely high prices. In short the perfect substrate is still missing.

Therefore we are currently investigating the optimized growth of nonpolar quasi-substrates by HVPE which can be used for subsequent device epitaxy, as this method provides large enough growth rates. However, the nucleation on foreign substrates usually requires a wide range of optimization parameters and is quite challenging. Therefore, we are studying the optimization of the template layers by metal organic vapor phase epitaxy (MOVPE) for the subsequent hydride vapor phase epitaxial (HVPE) process. In this manner, we ensure to use the advantages of both systems. Misoriented sapphire wafers are known to improve the surface quality of *c*-plane GaN layers [7]. Here, we present a systematic study of the influence of slightly misoriented *r*-plane sapphire substrates on the growth of non-polar *a*-plane GaN layers via the combination of MOVPE and HVPE.

2. Experimental

All samples investigated within this study are grown on quarters of 2 inch epi-ready *r*-plane sapphire wafers resulting in a GaN growth in $[11\bar{2}0]$ direction. We used a commercial horizontal flow Aixtron AIX-200/4 RF-S reactor with the standard precursors trimethylgallium (TMGa), trimethylaluminum (TMAI) and ammonia (NH_3) for the MOVPE growth. As carrier gas, we used Pd diffused hydrogen. The process temperature was controlled by a pyrometer at the backside of the rotation tray. Before starting growth the substrates were exposed to an in-situ desorption step at 1200°C for 10 min in hydrogen atmosphere. For the HVPE growth, a commercial horizontal flow Aixtron single-wafer system with five different heating zones was used. The carrier gas usually is a mixture of nitrogen and Pd diffused hydrogen. The precursors for the GaN growth are high purity NH_3 and GaCl which can be produced by streaming HCl gas over liquid gallium at a temperature of approximately 850°C .

As substrates we used *r*-plane sapphire wafers with a slight miscut ranging from -1.0° to 1.0° towards the $[0001]$ -axis of the sapphire in steps of 0.5° . The miscut is defined positive when the angle between surface and *c*-direction is smaller than the angle between the *r*-direction and the *c*-direction of the sapphire. The different samples were labeled as samples A (-1.0°), B (-0.5°), C (reference sample, $\pm 0^\circ$), D ($+0.5^\circ$) and E ($+1.0^\circ$), where lower case letters denote the respective MOVPE templates and capital letters the final HVPE grown samples. The growth process was identical for all samples. The MOVPE growth was carried out on half wafers, whereas the HVPE growth was performed on quarters in order to have exactly the same growth conditions for several samples.

First, a high temperature AlN nucleation layer (NL) with a thickness of about 30 nm was deposited in MOVPE. Then an initial GaN layer with a total thickness of approx. $3.3\ \mu\text{m}$ was grown in a two step growth process, interrupted by two in-situ SiN defect reduction layers. The first GaN layer was grown at a temperature of 1120°C , a pressure of 150 hPa, with a V/III-ratio of ≈ 2180 and a growth rate of $\approx 1.2\ \mu\text{m}/\text{h}$. After $0.3\ \mu\text{m}$, SiN was deposited by applying a constant flow of silane (SiH_4) and ammonia (NH_3). The surface was fractionally covered with SiN acting as a nanomask and influencing the morphology of the overgrown layer resulting in a defect reduction [8,9]. At a nominal thickness of $1.0\ \mu\text{m}$ a second SiN layer was deposited. Now, the growth parameters were changed to the second GaN step conditions: mainly the V/III-ratio was decreased to about 540, resulting in an

increased growth rate of $\approx 2.5 \mu\text{m}/\text{h}$. The growth parameters of the following single-step HVPE growth were as follows: A temperature of approximately 900°C , a pressure of 900 hPa , with a V/III-ratio of ≈ 18 and a total thickness of approximately $12 \mu\text{m}$.

For investigating the crystal quality, all samples were analysed by x-ray diffraction (XRD) rocking curve measurements (XRC) as well as low temperature (14K) photoluminescence (PL) spectra. The latter enables the qualification of typical defects in non-polar layers like basal plane stacking faults (BSFs) or prismatic stacking faults (PSFs) [10,11]. The surface quality was evaluated by scanning electron microscopy (SEM), optical phase contrast microscopy (OM) and atomic force microscopy (AFM).

3. Results and Discussion

Nonpolar a-plane GaN grown by MOVPE usually shows a typical morphology: A stripe like feature along the c direction and some surface pits [12]. We observed a reduced and more homogenous surface roughness for negative miscuts (samples a, b) whereas for positive miscuts the stripe like pattern becomes more pronounced and surface defects start to develop (d, e). This is consistent with the data reported by Araki et al. [13]. Even earlier, Imura et al. [14] reported a specular surface for miscut orientations of -0.5°

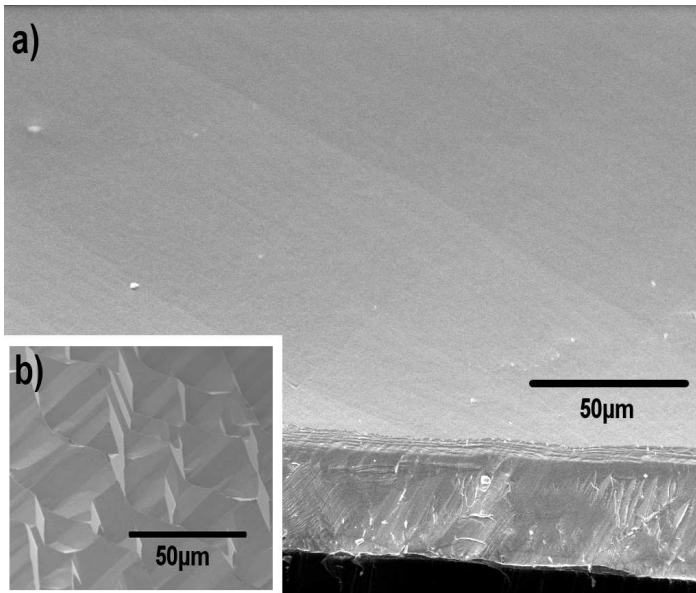


Fig. 1: a) SEM micrograph of the typical HVPE grown layers after optimization. The surface looks smooth without any facets, pits or stripe like features. b) The inset shows unoptimized HVPE GaN grown under high temperature conditions (color online).

(the definition of miscut angles is exactly opposite in this paper), which is also in line with our data. Investigations on the crystal quality via XRD and PL (not shown) are in contrast to these findings of the surface quality. The samples with higher miscut towards the positive direction (d, e) show reduced XRD linewidths and less stacking fault related luminescence (typically at 3.42 eV and $3.30\text{--}3.35 \text{ eV}$) compared to the PL signal from the near band edge region.

3.1 GaN grown by HVPE

Before growing on these miscut templates, we have optimized the growth of nonpolar GaN on exactly oriented r-plane wafers. The growth parameters like temperature, pressure, V/III-ratio, H₂/N₂-ratio, growth rate etc. have been varied to get layers with optimized surface and crystal quality. Layers grown before this optimization usually had a very rough and faceted surface (Fig. 1 b).

3.2 MOVPE template

The typical surface of HVPE grown GaN after optimization (Fig. 1 a) is very smooth and does exhibit neither the often observed surface defects ("pits") nor the stripe like features otherwise typical for a-plane GaN on r-plane sapphire grown by MOVPE.

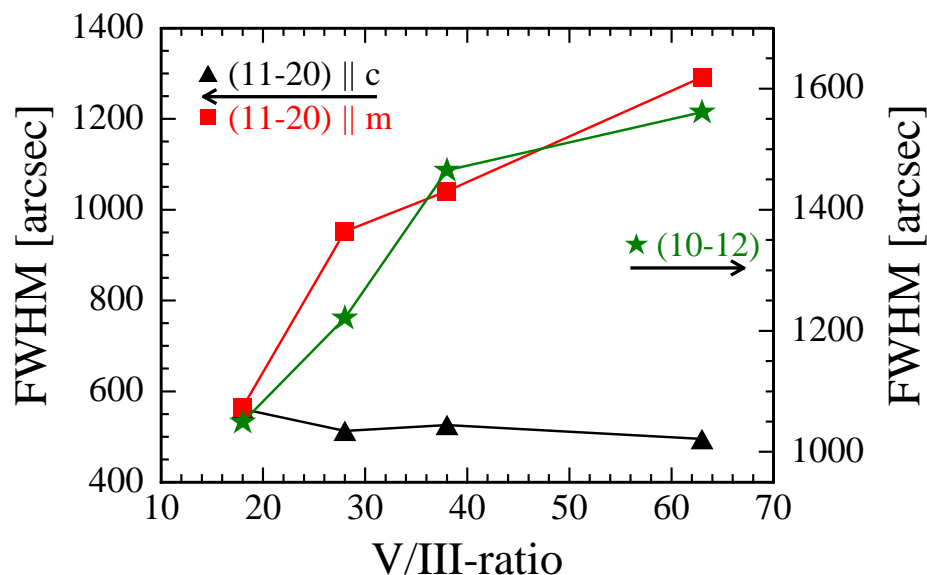


Fig. 2: XRC FWHM values for HVPE grown GaN layers with different V/III-ratio during growth. The improvement for lower values can clearly be seen (color online).

The optimized overgrowth in HVPE does not only improve the surface morphology but also the crystal quality of the layers. X-ray rocking curve linewidths of the symmetrical reflections could be reduced from around 750 arcsec for the MOVPE template to less than 500 arcsec for the HVPE grown layer regardless of the direction of the incident beam. Besides the temperature which is the key parameter for a flat surface ($T \approx 900^\circ\text{C}$, cf. Fig. 1), the ammonia flow rate is the growth parameter that shows the strongest influence. Only for low V/III-ratios (≤ 20) it is possible to grow a-plane GaN layers in HVPE with nearly no anisotropy in XRD measurements (Fig. 2). Smaller asymmetric reflection linewidths like $(10\bar{1}2)$ are also indicating a better crystal quality.

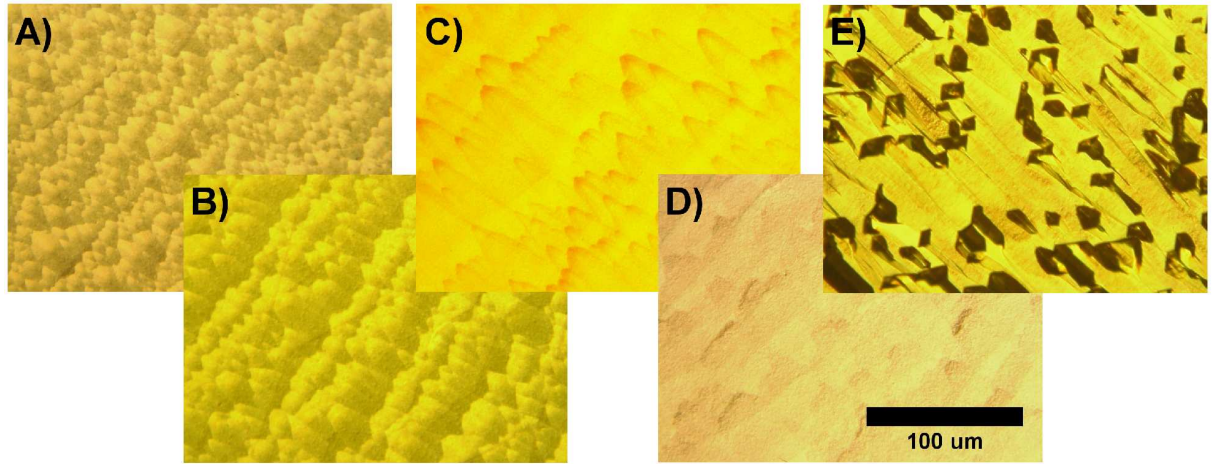


Fig. 3: Optical microscope images of the surfaces of the HVPE grown samples with different miscut A) -1° , B) -0.5° , C) 0° , D) $+0.5^\circ$, E) $+1^\circ$ (color online).

The final HVPE GaN layers show a different surface morphology for the different miscut angles (Fig. 3). It seems that a negative miscut (samples A, B) leads to a rough surface with a high density of microscopic hillocks with an average diameter of approximately $20\ \mu\text{m}$. Both, no miscut and a miscut towards positive angles leads to drastically improved surfaces. The morphology gets more homogenous and the roughness is decreased. This also could be proven by AFM measurements (not shown). However, if the miscut is

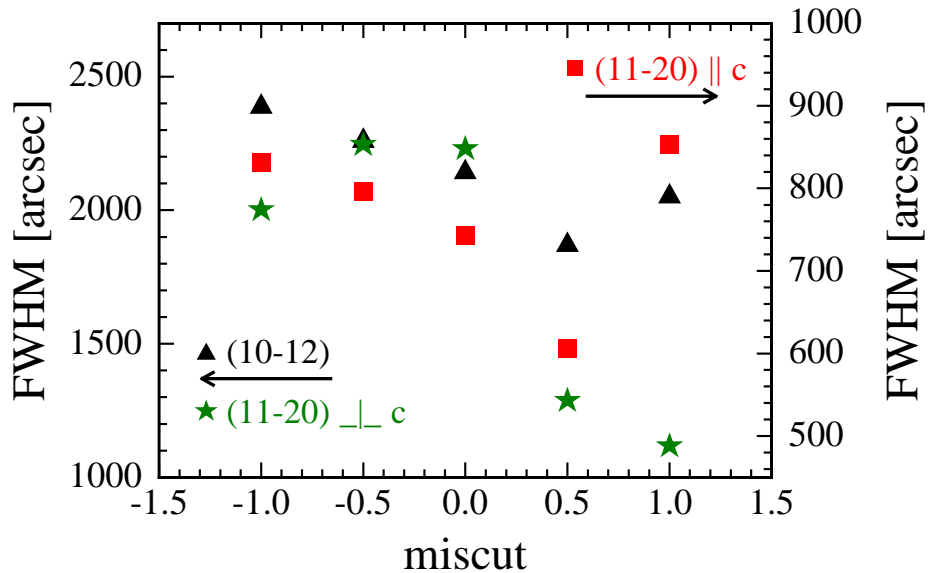


Fig. 4: FWHM of XRD rocking curves. The asymmetrical $(10\bar{1}2)$ reflection and the symmetrical $(11\bar{2}0)$ reflection with the incident beam perpendicular (parallel) to the *c* direction is plotted to the left (right). (color online).

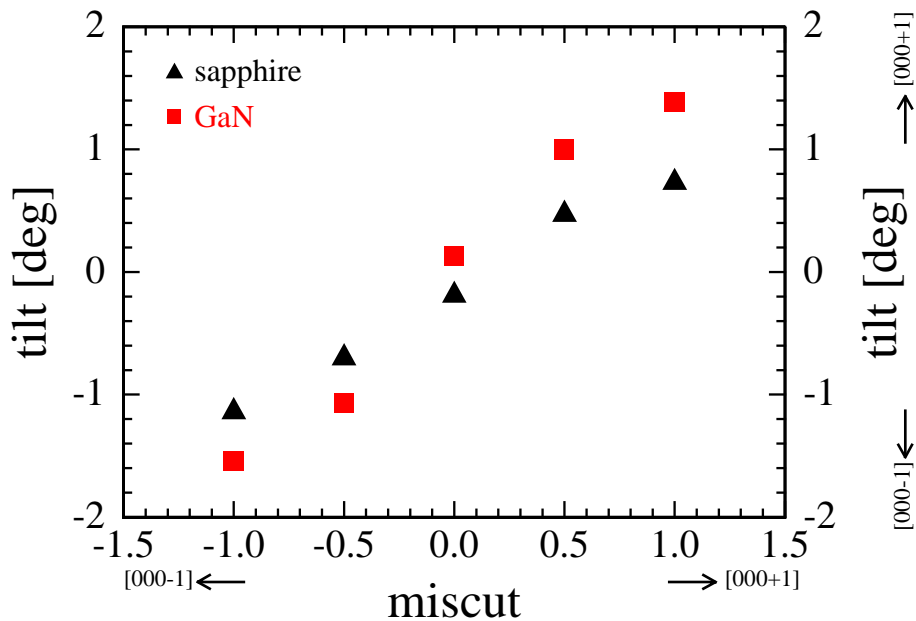


Fig. 5: Inclination of the HVPE grown GaN layers and the sapphire wafers, measured by XRD. The tilt of the sapphire (black triangles) and the GaN (red squares) is plotted against the (nominal) miscut of the sapphire substrate (color online).

too large, the — from MOVPE growth — well known surface defects start to develop so that the resulting surface is even rougher than for negative miscut angles (E). The pits themselves are of increased size when compared to the MOVPE templates because of the increased thickness of the sample.

In order to judge the crystal quality of the samples, XRC measurements were performed (Fig. 4). Somehow as expected from the results of the MOVPE grown templates, the crystal quality for the samples with negative miscut is worse compared to layers grown on positive miscut substrates. But in contrast to those findings, the smallest FWHM values were not measured for the sample with the highest positive miscut (E) but for sample D with a slight miscut of $+0.5^\circ$. Nevertheless this fits quite well to the results of the optical investigations of the HVPE grown samples. As the $(10\bar{1}2)$ reflection is known to be sensitive to edge and screw dislocations [15], it is often used to judge the crystal quality. The FWHM of this reflection is essentially smaller for the samples with a positive miscut. In particular sample D shows the strongest improvement and smallest values.

One question of course will rise if one grows on miscut substrates. How is the inclination between substrate and layer, between sapphire and GaN? To analyze this, again XRC measurements were recorded (Fig. 5). The measured miscuts of the sapphire wafers agree to the nominal values. For all miscuts, the overgrown GaN layer shows an inclination angle with respect to the surface that is larger than the miscut of the sapphire. The data points shown in figure 5 represent the direction of the normal of the reflection plane. This means that the tilt is measured with respect to the surface. So the inclination of

the a-direction of GaN is even higher than and in the same direction as the tilt of the sapphire r-plane. Hence the tilting of the GaN layer is totally opposed to the miscut of the sapphire (with respect to the ‘normal’ r-plane surface).

4. Summary

We studied the influence of slightly misoriented r-plane sapphire substrates on the crystal quality and surface morphology of a-plane GaN grown by HVPE on MOVPE templates. We found strongly different miscuts for the best values of either of these two parameters. The situation got better after HVPE growth: Now, both, surface quality and crystal quality can be improved by a slight miscut of $+0.5^\circ$ towards the [0001] direction. It was also shown that the GaN layers are grown tilted with respect to the sapphire wafers with an inclination totally opposed to that of the miscut sapphire substrate.

5. Acknowledgments

This work was financially supported by the Deutsche Forschungsgemeinschaft within the research group “Polarization Field Control in Nitride Light Emitters (PolarCoN)” under contract no. Scho 393/22-1.

References

- [1] F. Bernardini, V. Fiorentini, and D. Vanderbilt, “Spontaneous polarization and piezoelectric constants of III-V nitrides”, *Phys. Rev. B*, vol. 56, pp. R10024–R10027, 1997.
- [2] T. Takeuchi, C. Wetzel, S. Yamaguchi, H. Sakai, H. Amano, and I. Akasaki, “Determination of piezoelectric fields in strained GaInN quantum wells using the quantum-confined Stark effect”, *Appl. Phys. Lett.*, vol. 73, pp. 1691–1693, 1998.
- [3] M.D. Craven, S.H. Lim, F. Wu, J.S. Speck, and S.P. DenBaars, “Structural characterization of nonpolar (1120) a-plane GaN thin films grown on (1102) r-plane sapphire”, *Appl. Phys. Lett.*, vol. 81, pp. 469–471, 2002.
- [4] B. Imer, F. Wu, M.D. Craven, J.S. Speck, and S.P. DenBaars, “Stability of (1100) m-plane GaN films grown by metalorganic chemical vapor deposition”, *Jpn. J. Appl. Phys.*, vol. 45, pp. 8644–8647, 2006.
- [5] A-T. Cheng, Y-K. Su, W-C. Lai, and Y-Z. Chen, “Metalorganic vapor phase epitaxy growth of m-plane GaN using LiAlO₂ substrates”, *Jpn. J. Appl. Phys.*, vol. 47, pp. 3074–3076, 2008.
- [6] T. Paskova, R. Kroeger, S. Figge, D. Hommel, V. Darakchieva, B. Monemar, E. Preble, A. Hanser, N.M. Williams, and M. Tutor, “High-quality bulk a-plane GaN sliced from boules in comparison to heteroepitaxially grown thick films on r-plane sapphire”, *Appl. Phys. Lett.*, vol. 89, p. 051914, 2006.

- [7] F. Scholz, P. Brückner, F. Habel, M. Peter, and K. Köhler, “Improved GaN layer morphology by hydride vapor phase epitaxy on misoriented Al_2O_3 wafers”, *Appl. Phys. Lett.*, vol. 87, p. 181902, 2005.
- [8] A. Chakraborty, K.C. Kim, F. Wu, J.S. Speck, S.P. DenBaars, and U.K. Mishra, “Defect reduction in nonpolar a-plane GaN films using in situ SiN_x nanomask”, *Appl. Phys. Lett.*, vol. 89, p. 041903, 2006.
- [9] J. Hertkorn, F. Lipski, P. Brückner, T. Wunderer, S.B. Thapa, F. Scholz, A. Chuvilin, U. Kaiser, M. Beer, and J. Zweck, “Process optimization for the effective reduction of threading dislocations in MOVPE grown GaN using in situ deposited SiN_x masks”, *J. Crystal Growth*, vol. 310, pp. 4867–4870, 2008.
- [10] R. Liu, A. Bell, F.A. Ponce, C.Q. Chen, J.W. Yang, and M.A. Khan, “Luminescence from stacking faults in gallium nitride”, *Appl. Phys. Lett.*, vol. 86, p. 021908, 2005.
- [11] P.P. Paskov, T. Paskova, B. Monemar, S. Figge, D. Hommel, B.A. Haskell, P.T. Fini, J.S. Speck, and S. Nakamura, “Optical properties of nonpolar a-plane GaN layers”, *Superlattices and Microstructures*, vol. 40, pp. 253–261, 2006.
- [12] T.S. Ko, T.C. Wang, R.C. Gao, H.G. Chen, G.S. Huang, T.C. Lu, H.C. Kuo, and S.C. Wang, “Study on optimal growth conditions of a-plane GaN grown on r-plane sapphire by metal-organic chemical vapor deposition”, *J. Crystal Growth*, vol. 300, pp. 308–313, 2007.
- [13] M. Araki, N. Mochimizo, K. Hoshino, and K. Tadatomo, “Effect of misorientation angle of r-plane sapphire substrate on a-plane GaN grown by metalorganic vapor phase epitaxy”, *Jpn. J. Appl. Phys.*, vol. 47, pp. 119–123, 2008.
- [14] M. Imura, A. Hoshino, K. Nakano, M. Tsuda, M. Iwaya, S. Kamiyama, H. Amano, and I. Akasaki, “Flat (1120) GaN thin film on precisely offset-controlled (1102) sapphire substrate”, *Jpn. J. Appl. Phys.*, vol. 44, pp. 7418–7420, 2005.
- [15] B. Heying, X.H. Wu, S. Keller, Y. Li, D. Kopolnek, B.P. Keller, S.P. DenBaars, and J.S. Speck, “Role of threading dislocation structure on the x-ray diffraction peak widths in epitaxial GaN films”, *Appl. Phys. Lett.*, vol. 68, pp. 643–645, 1996.

Inverse GaN Pyramids for Semipolar GaInN/GaN Light-Emitting Diodes

Thomas Wunderer

Excellent semipolar GaN material quality can be obtained by growing inverse GaN pyramids on full 2 inch c-plane sapphire when combining the advantages of defect reduction via FACELO and selective area growth for faceted surfaces. The nearly defect free material is obtained by structuring the mask into a honeycomb pattern. When realizing full GaInN/GaN LED structures on those templates, a relatively broad emission is observed during electroluminescence measurements. Furthermore, the dominant wavelength is found to be dependent on the applied current density. The pronounced shift is in good agreement with the wavelength shift along one single facet. Gas phase diffusion during the active area growth is believed to be the main reason for the varying indium content. The homogeneity could be influenced by changing the reactor pressure during the active area growth.

1. Introduction

Non- and semipolar group III-nitrides providing reduced piezoelectric fields are promising candidates for improved device performance due to an increased overlap of the electron and hole wave functions within the quantum wells (QWs) [1]. Nevertheless, one main problem is still limiting the use of non- or semipolar material for commercial production: On foreign substrates with conventional size just inferior material quality compared to c-plane growth can be achieved up to now. In this case, non-radiative recombination is compensating the advantage of the reduced fields and leads to a moderate performance of such devices [2–4]. On the other hand, high quality material can be obtained by cutting pieces from HVPE grown c-plane GaN in the desired direction on which high performance devices were achieved [5]. However, the limited sample size and its high price are still limiting factors for any mass production [6].

In the late 1990s, the technique of facet-controlled epitaxial lateral overgrowth (FACELO) was successfully developed to reduce the defect density of group III-nitrides [7]. Selective area epitaxy can also be used to form three dimensional (3D) GaN structures with side facets providing semipolar surfaces. Hence, complete semipolar device structures can be obtained on low-cost full 2 inch or larger c-oriented sapphire wafers [8].

In this work, we highlight the possibility to combine the advantages of both techniques, efficient defect reduction via FACELO and the formation of 3D structures providing semipolar GaN surfaces using selective area epitaxy. The 3D structures are used as high quality GaN templates for the implementation of complete LED structures for electroluminescence

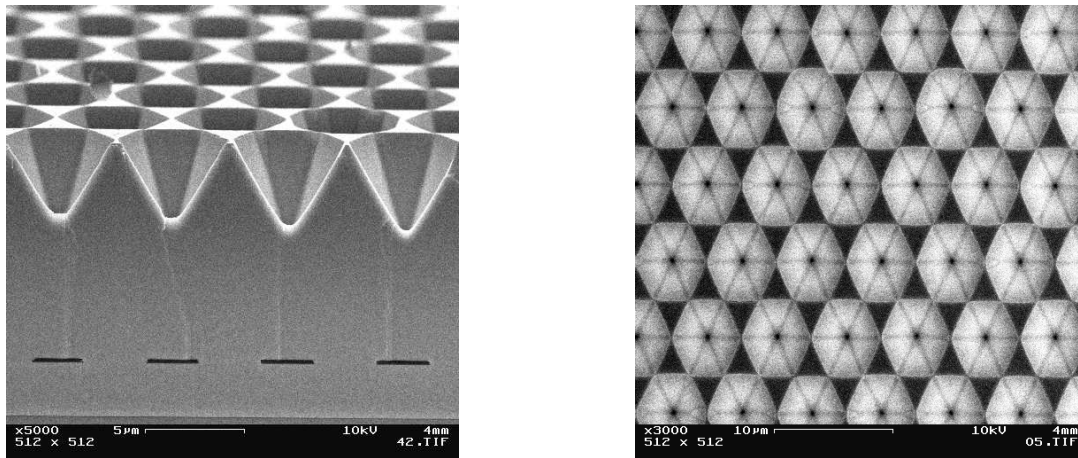


Fig. 1: SEM pictures of 3D GaInN/GaN LED structure: bird's eye view (left) and top view (right).

(EL) test measurements. The unconventional electro-optical properties are analyzed by means of the local layer properties with respect to the structured surface. It is found that the indium composition and QW thickness is varying along a single facet.

2. Experimental

All samples were grown by low pressure metalorganic vapor phase epitaxy (MOVPE). First, about 2 μm thick, high quality GaN was grown on c-plane sapphire wafers including an in-situ deposited SiN interlayer for effective defect reduction [9]. Then, a 200 nm thick SiO₂ layer was deposited via plasma enhanced chemical vapor deposition (PECVD) and structured into a honeycomb pattern serving as a mask for the subsequent selective area growth. Using optimized GaN growth conditions (low temperature, low V/III ratio, high pressure) perfectly ordered inverse pyramids can be realized providing semipolar facets which increase the effectively usable surface. A detailed description of the formation of the 3D structures can be found elsewhere [10]. Realizing a complete LED structure, the 3D GaN template is n-doped, followed by a 5-fold Ga_{1-x}In_xN/GaN multiple quantum well (MQW) layer stack with a nominal QW thickness of 4 nm and an In concentration x exceeding 30%, a p-AlGa_{0.5}N electron blocking layer and a p-GaN top layer. For EL test measurements simple indium contacts are realized by standard photo lithography and e-beam evaporation of the metal.

3. Results and discussion

Different to previous studies [10], the GaN regrowth in the 2nd epitaxial step was elongated allowing for the coalescence of the material above the masked area. This strategy follows the idea of defect reduction via the FACELO principle. Threading dislocations (TDs) which are not blocked, neither by the in-situ deposited SiN nor the ex-situ deposited SiO₂ mask, and penetrate through the opening are bent to the side due to selective area growth.

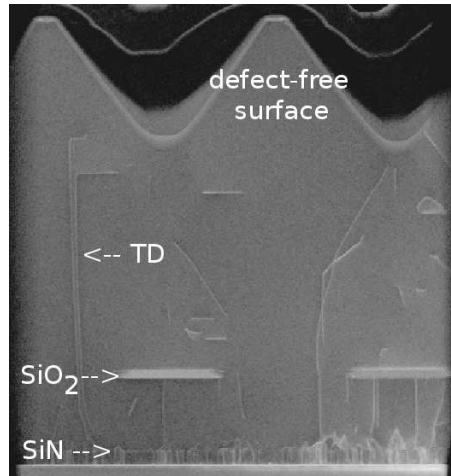


Fig. 2: TEM image of inverse pyramid structure showing the efficient defect reduction.

Using the mask with the honeycomb pattern the TDs are bundled in one point above the mask and (nearly) defect free semipolar facets develop for the subsequent deposition of the active area.

As can be seen in Fig. 1, the 3D surface can be transferred to a higher region above the mask using 3D growth parameters. A planarization of the structure is prohibited whereas it is preferred for typical FACELO samples. Perfectly ordered inverse GaN pyramids are formed providing smooth $\{1\bar{1}01\}$ facets. Transmission electron microscopy (TEM) analyses confirm the efficiency of this technique as no TD could be observed reaching the semipolar surface (Fig. 2). They are blocked by the in-situ deposited SiN, the SiO₂ mask or are bent sideways.

The high material quality is further confirmed via x-ray rocking curve measurements (XRC) and optical investigations using photo- and cathodoluminescence measurements

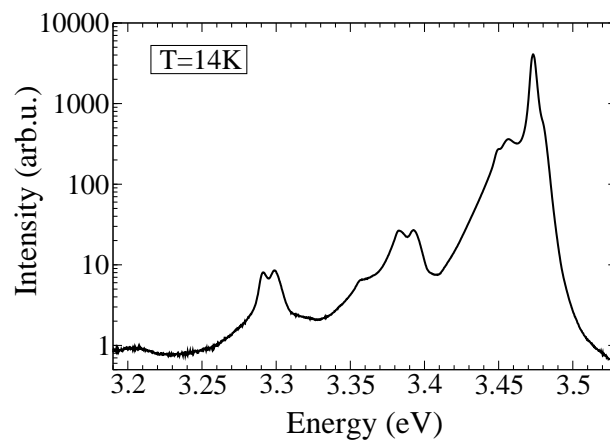


Fig. 3: PL spectrum of inverse GaN pyramids recorded at 14K. The FWHM of the D⁰X at 3.479 eV is determined to be as small as 2.2 meV. No stacking fault-related transition observable as typically found in non-polar GaN on foreign substrates [11].

(PL, CL), respectively. The following values displaying the full-width at half maximum (FWHM) of symmetric and asymmetric reflections, respectively, could be obtained from XRC measurements: 299 arcsec for the (00.2), 410 arcsec for the (10.1), 416 arcsec for the (10.2) and 284 arcsec for the (11.2) reflection. Fig. 3 shows the PL spectrum of the 3D GaN recorded at 14 K. No stacking fault-related transition could be observed for the sample as it is typically found for non-polar GaN grown on foreign substrates [11]. The FWHM of the donor-bound exciton transition (D^0X) at 3.479 eV is as small as 2.2 meV.

Analyzing the structural properties of the active area of the LED sample using scanning TEM (STEM), well developed GaInN QWs with abrupt interfaces can be observed confirming the high material quality from the optical active region, (Fig. 4).

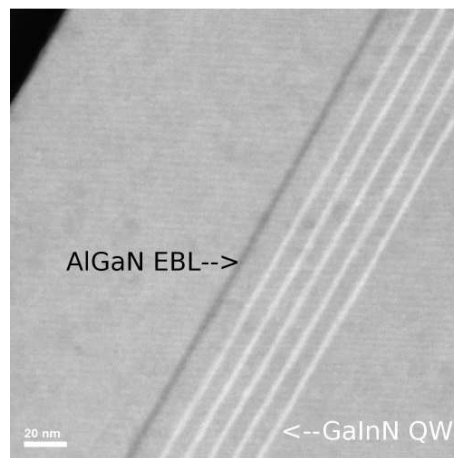


Fig. 4: STEM image of semipolar GaInN/GaN LED structure grown on inverse pyramids.

Figure 5 shows the respective EL spectra recorded for currents between 1 and 20 mA during EL test measurements. A relatively broad emission is detected from the integrally collected light which is not expected when taking into account the reduced piezoelectric field on semipolar surfaces. Whereas for small currents the longer wavelength in the green spectral region is dominating, the emission shifts towards the blue spectral region for higher currents. The exact color coordinate for each current is depicted in Fig. 6. Interestingly, for a current of 1 mA white light can be realized without the use of any phosphor. Furthermore, the coverage of the LED with an orange-red phosphor should open the possibility for the generation of white light with a high color rendering index (CRI) at a high excitation level as there would be no green minimum as often seen in the spectra of commercially available white LEDs.

The unusual shift of the color coordinate within the color diagram can not be simply explained by state filling of potential fluctuations within the QWs when increasing the current. For the 3D surface it is essential to investigate the local layer properties with respect to the specific position on the sample.

Indeed, a strong influence on the QW emission properties was observed within one single facet when performing spatially resolved SEM-CL investigations [12]. Looking to the wavelength distribution on the 3D surface of an undoped sample with a single GaInN

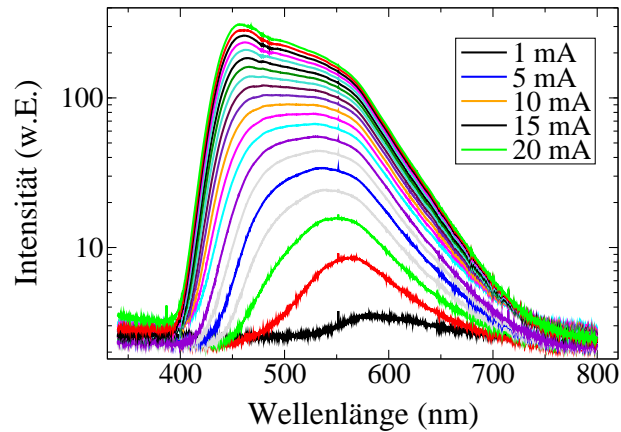


Fig. 5: EL spectra of semipolar GaInN/GaN LED grown on inverse GaN pyramids for currents between 1 and 20 mA.

QW grown under similar conditions the following situation can be recognized (Fig. 7): From the c-plane areas no QW emission could be recorded at all. This phenomenon can be understood as the QW thickness on the c-plane areas was determined to be as thick as about 7 nm with a relatively high indium content. Due to the resulting high piezoelectric field on the c-plane and the unconventionally thick QW, electron and hole wavefunctions get extremely separated. Therefore, the recombination probability is very weak with consequently a completely depressed QW emission. On the other hand, strong luminescence is observed from the semipolar facets. Whereas a longer QW emission wavelength is recorded at the top of the structure, it shifts gradually to shorter wavelengths when coming closer to the tip. From the edges where two $\{1\bar{1}01\}$ planes meet each other a shorter and brighter emission can be recorded. Now, one can argue that the main part of the green emission spectrum during the EL test measurements originates from the upper

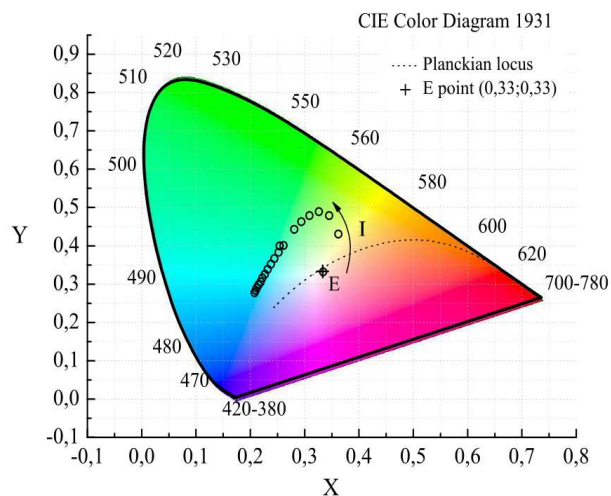


Fig. 6: Color coordinates for currents between 1 and 20 mA determined from the respective spectra (see Fig. 5).

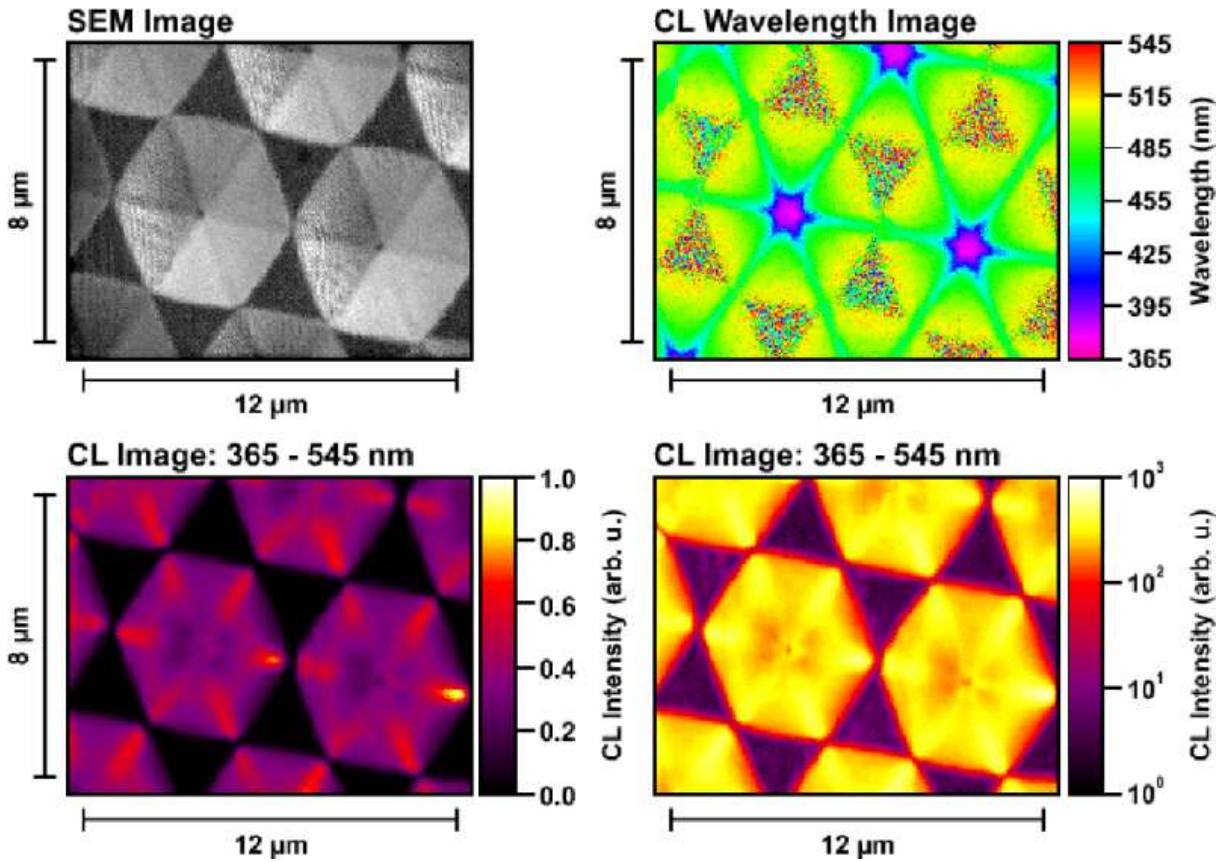


Fig. 7: SEM-CL images recorded from an undoped GaInN single QW grown on inverse pyramids with semipolar $\{1\bar{1}01\}$ facets.

$\{1\bar{1}01\}$ facets, whereas the blue spectral part has its origin from the edges and the area near the tip, correlated with a possible change of the current distribution over the facet area with increasing applied voltage.

The absolute value of the wavelength shift is very much dependent on the geometry of the sample and the growth conditions chosen for the active area growth. Due to the fact that just a slight change of the QW thickness is determined by analyzing the STEM pictures, the strongest influence on the emission wavelength must result from a difference in the indium composition varying along the facet. It is thought that gas phase diffusion and surface migration during the active area growth are remarkably reduced due to the growth conditions necessary for a high indium incorporation efficiency. As could be confirmed by ongoing experiments the wavelength shift could be influenced by changing the growth conditions with respect to the diffusion coefficient. E.g. the variation of the reactor pressure during the active area growth influenced the linewidth of the emission [13] and could probably explain the pronounced shift observed by Nishizuka et al. for GaInN/GaN stripes with $\{11\bar{2}2\}$ facets grown at atmospheric pressure [14].

4. Conclusion

Semipolar GaInN/GaN LEDs were realized on the $\{1\bar{1}01\}$ side facets of selectively grown inverse GaN pyramids on full 2 inch sapphire wafers. The excellent material quality was confirmed by TEM and STEM analyses which suggest (nearly) defect free semipolar surfaces. The relatively broad QW emission during electroluminescence test measurements are correlated with the gradually varying QW wavelength emission along one single facet. Its origin is mainly thought to arise from a different indium composition as a result of gas phase diffusion processes during the active area growth as the QW thickness does not change drastically. Furthermore, the dominant peak wavelength is found to be dependent on the applied current density. Those properties could be advantageous for the generation of white light emitters with a high CRI whereas the desired color coordinate can be fine-tuned by the current.

Acknowledgments

We gratefully acknowledge the fruitful cooperation with M. Feneberg, I. Tischer, M. Wiedenmann and K. Thonke from the Inst. of Quantum Matter, Ulm University, Ulm, Germany. TEM and STEM investigations have been performed by A. Chuvilin and U. Kaiser from the Central Facility of Electron Microscopy, Ulm University, Ulm, Germany. CL measurements have been carried out by S. Metzner, F. Bertram, and J. Christen from the Institute of Experimental Physics, Otto-von-Guericke-University, Magdeburg, Germany. The color coordinates were determined by S. S. Shirokov and A. E. Yunovich from the Department of Physics, M. V. Lomonosov Moscow State University, Moscow, Russia. Furthermore I want to thank J. Wang, F. Lipski, S. Schwaiger, I. Argut, K. Forghani, R. Rösch and F. Scholz for their encouragement. This work was financially supported by the Deutsche Forschungsgemeinschaft (DFG).

References

- [1] P. Waltereit, O. Brandt, A. Trampert, H. Grahn, J. Menniger, M. Ramsteiner, M. Reiche, and K. Ploog, “Nitride semiconductors free of electrostatic fields for efficient white light-emitting diodes”, *Nature*, vol. 406, pp. 865–868, 2000.
- [2] A. Chakraborty, B.A. Haskell, H. Masui, S. Keller, J.S. Speck, S.P. DenBaars, S. Nakamura, and U.K. Mishra, “Nonpolar m -plane blue-light-emitting diode lamps with output power of 23.5mW under pulsed operation”, *Jpn. J. Appl. Phys.*, vol. 45, pp. 739–741, 2006.
- [3] B. Liu, R. Zhang, Z.L. Xie, C.X. Liu, J.Y. Kong, J. Yao, Q.J. Liu, Z. Zhang, D.Y. Fu, X.Q. Xiu, H. Lu, P. Chen, P. Han, S.L. Gu, Y. Shi, Y.D. Zheng, J. Zhou, and S.M. Zhou, “Nonpolar m -plane thin film GaN and InGaN/GaN light-emitting diodes on LiAlO₂ (100) substrates”, *Appl. Phys. Lett.*, vol. 91, pp. 253506-1–3, 2007.

-
- [4] S. Hwang, Y.G. Seo, K.H. Baik, I. Cho, J.H. Baek, S. Jung, T.G. Kim, and M. Cho, “Demonstration of nonpolar a-plane InGaN/GaN light emitting diode on r-plane sapphire substrate”, *Appl. Phys. Lett.*, vol. 95, pp. 071101-1–3, 2009.
- [5] K.-C. Kim, M. Schmidt, H. Sato, F. Wu, N. Fellows, M. Saito, K. Fujito, J. Speck, S. Nakamura, and S. DenBaars, “Improved electroluminescence on nonpolar m-plane InGaN/GaN quantum wells LEDs”, *phys. stat. sol. (RRL)*, vol. 1, pp. 125–127, 2007.
- [6] U. Schwarz and M. Kneissel, “Nitride emitters go nonpolar”, *phys. stat. sol. (RRL)*, vol. 1, pp. A44–46, 2007.
- [7] B. Beaumont, P. Vennéguès, and P. Gibart, “Epitaxial lateral overgrowth of GaN”, *phys. stat. sol. (b)*, vol. 227, pp. 1–43, 2001.
- [8] T. Wunderer, P. Brückner, B. Neubert, F. Scholz, M. Feneberg, F. Lipski, M. Schirra, and K. Thonke, “Bright semipolar GaInN/GaN blue light emitting diode on side facets of selectively grown GaN stripes”, *Appl. Phys. Lett.*, vol. 89, pp. 041121-1–3, 2006.
- [9] J. Hertkorn, F. Lipski, P. Brückner, T. Wunderer, S.B. Thapa, F. Scholz, A. Chuvilin, U. Kaiser, M. Beer, and J. Zweck, “Process optimization for the effective reduction of threading dislocations in MOVPE grown GaN using in situ deposited SiN_x masks”, *J. Crystal Growth*, vol. 310, pp. 4867–4870, 2008.
- [10] T. Wunderer, F. Lipski, J. Hertkorn, S. Schwaiger, and F. Scholz, “Fabrication of 3D InGaN/GaN structures providing semipolar GaN planes for efficient green light emission”, *phys. stat. sol. (c)*, vol. 6, pp. S490–S493, 2009.
- [11] P.P. Paskov, R. Schifano, B. Monemar, T. Paskova, S. Figge, and D. Hommel, “Emission properties of a-plane GaN grown by metal-organic chemical-vapor deposition”, *J. Appl. Phys.*, vol. 98, pp. 093519-1–7, 2005.
- [12] T. Wunderer, F. Lipski, S. Schwaiger, J. Hertkorn, M. Wiedenmann, M. Feneberg, K. Thonke, and F. Scholz, “Properties of blue and green InGaN/GaN quantum well emission on structured semipolar surfaces”, *Jpn. J. Appl. Phys.*, vol. 48, pp. 060201-1–3, 2009.
- [13] T. Wunderer, J. Wang, F. Lipski, S. Schwaiger, K. Forghani, and F. Scholz, to be published.
- [14] K. Nishizuka, M. Funato, Y. Kawakami, Y. Narukawa, and T. Mukai, “Efficient rainbow color luminescence from In_xGa_{1-x}N single quantum wells fabricated on {11 $\bar{2}$ 2} microfacets”, *Appl. Phys. Lett.*, vol. 87, pp. 231901-1–3, 2005.

Sample Support Development for In-Situ Ultra-HRTEM Electrical Investigations

Benedikt Westenfelder

Specially designed sample supports have been developed to permit in-situ investigation of the electrical conductivity of ultrathin samples e.g. sheets of graphene or semiconductor nanofoils in a high-resolution transmission electron microscope (HRTEM). This report describes different ways of realization of a suitable sample platform including the corresponding electrode support geometry.

1. Introduction

The measurement of the influence of adsorbates in terms of individual molecules or atoms on the conductivity of ultrathin materials at simultaneous visualization of events taking place on atomic scale opens not only new horizons in basic research but also provides a well-founded scientific background with regard to potential sensor applications as proposed by F. Schedin et al. [1] in 2007.

In principle the performance of (in-situ) electrical studies in a HRTEM offers a very attractive solution. On one hand, it provides an effective real-time observation of the sample; on the other hand — at adequately low acceleration voltages — it is a relatively non-destructive characterization method for a wide range of materials.

In order to achieve this goal, the respective samples should be both simultaneously: eminently thin and free-standing. With respect to this technological challenge, world wide only few successful experiments are known. In case of semiconductor nanofoils so far no experiments are known. In case of graphene there is one, but very elaborate measuring principle. On this, a sheet of graphene is mounted on a standard TEM grid to realize an electrode from the samples backside. The second contact is made by a scanning tunneling microscope (STM) tip using a particular TEM–STM platform [2, 3].

Here, we present various approaches to realize an in situ electrical measuring sample platform. These sample supports are not only uniquely adaptive but also provide reproducible environmental conditions, which is one of the most important aspects to gain quantitative information and in the face of future applications.

2. Fabrication Approaches

2.1 Approach I: Procedures based on commercially available and already perforated SiN membranes

Commercially available support chips on the basis of silicon with a maximum diameter of 3.05 mm are already very common for TEM investigations. In general they consist of

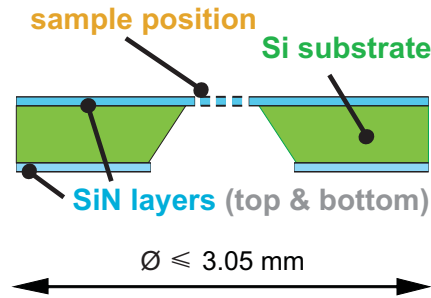


Fig. 1: Schematic cross-sectional view of a typical TEM sample support chip.

two insulating nitride (SiN) or dioxide (SiO₂) layers. One is located at the upper and a second one at the lower surface of a silicon substrate. To achieve a perforated membrane, each of these films needs to be structured. Into the top layer, arrays of little opening are etched on which the sample later will be positioned. The masking of the bottom layer is used to etch selectively large areas of exposed silicon up to the opposing top layer (Fig. 1). The thickness of the resulting SiN or SiO₂ membrane, hole diameter as well as hole pitch are typical size parameters offered for sale to choose them according to the individual requirements (Fig. 2).

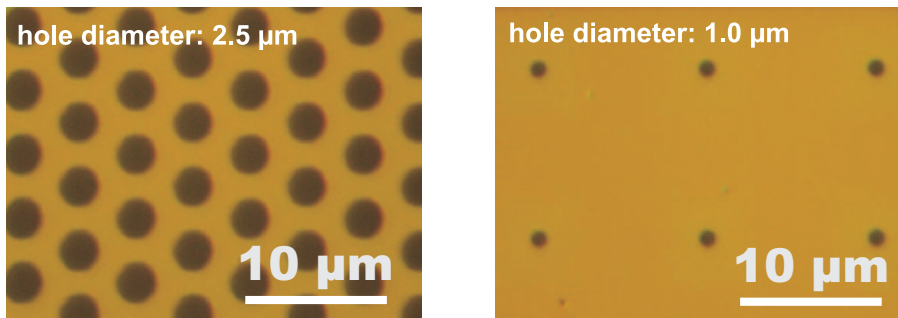


Fig. 2: Two optical micrographs of purchasable SiN membranes with different hole maskings.

Optical lithography is usually the most efficient way to deposit metal electrode structures on these membranes. In this context one should check if the sample supports offered by the supplier are only available as single frame chips or in terms of single frames joint with each other to a so called multi frame array (Fig. 3 a). In the latter case, annoying side wall formations arising from the photo resist can be easier avoided. Otherwise edge beads near the membrane will not only cause loss in lithographic resolution but also reduce dramatically the surface effectively usable for lithographic applications (Fig. 3 b).

Furthermore, after exceeding a critical hole pitch and diameter, resist ripples can arise along the perforated membrane areas leading again to losses of the lithographic resolution (Fig. 3 c). The magnitude of these parameters depends on the viscosity of the photoresist and the occurring surface tension.

Moreover, prior to each resist coating an oxygen plasma treatment of the chip surface is highly recommend. Otherwise the implied surface tension can tend to a rolling off of the liquid during the spin coating process (Fig. 3 d,e).

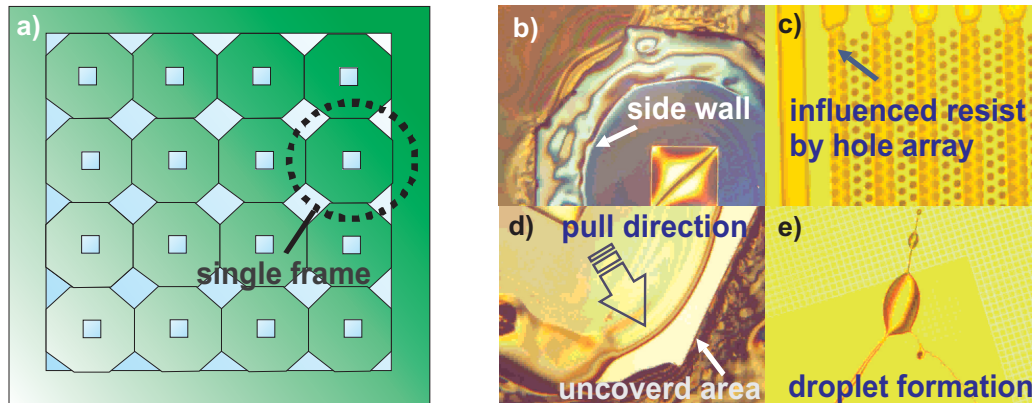


Fig. 3: a) Schematic illustration of a multi frame array chip. This arrangement allows the simultaneous processing of several single frames which can be snapped out, when all lithographic steps are finished. b) Optical micrograph of a single frame chip coated with resist exhibiting highly distinct side wall formations on its edges. c) Resist stripes covering a SiN membrane, where the homogeneity of the thickness is strongly influenced by the perforation. d) Corner region of a single frame chip: Here, the resist tended to a droplet formation. Uncoated areas are remaining, because only a little droplet became pulled apart from the center towards the sample edges. The most of the resist got slipped away during the spin coating by the centrifugal force. e) After the coating only few resist droplets are still adhering at the SiN surface - almost all of the resist got slipped away.

For simple two probe measurements, an interdigitated finger electrode geometry is recommended. This is at most flexible with regard to the sample position (Fig. 4).

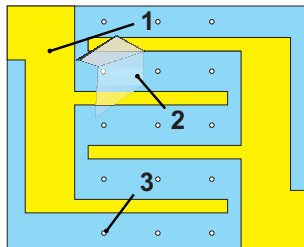


Fig. 4: Schematic top view how an interdigitated finger electrode structure could be easily realized: 1) Metal electrode structure. 2) The sample material e.g. a flake of graphene. 3) In-between the electrodes located membrane holes, onto which the sample should be positioned.

2.2 Approach II: Procedures based on commercially available and non-perforated SiN membranes

In order to gain more flexibility concerning sample size and electrode geometry, in this approach the membrane hole parameter are chosen by oneself. This can easily be achieved by a focused ion beam (FIB) etching procedure (Fig. 5). For this purpose we use the same commercially available TEM support chips, just without perforation of the SiN membrane.

This approach takes advantage if the sample can be positioned accurately, not only in terms of the electrode and hole design. Also a smaller amount of holes and likewise smaller sizes of the SiN membranes can be chosen to improve its mechanical stability. This of particular importance in view of lithography based processes, e.g. electrode fabrication as described above.

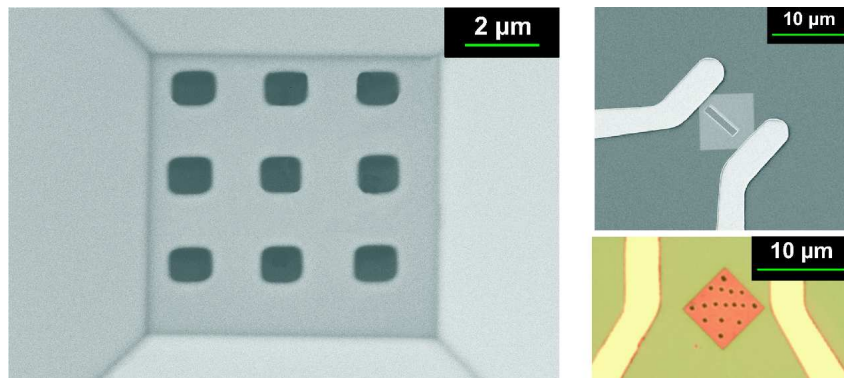


Fig. 5: Scanning electron microscope (SEM) view of variously FIB-perforated membranes from the back (left) and top side (right). Gold electrodes were deposited beside the FIB-fabricated openings.

2.3 Approach III: Procedures based on self-fabricated SiN membranes

Opposite to the approaches described before, the following procedure is based on self-fabricated support chips. Thereby one gains a maximum of flexibility with regard to the choice of electrode or membrane hole design as well as simplified handling during its lithography based fabrication processes.

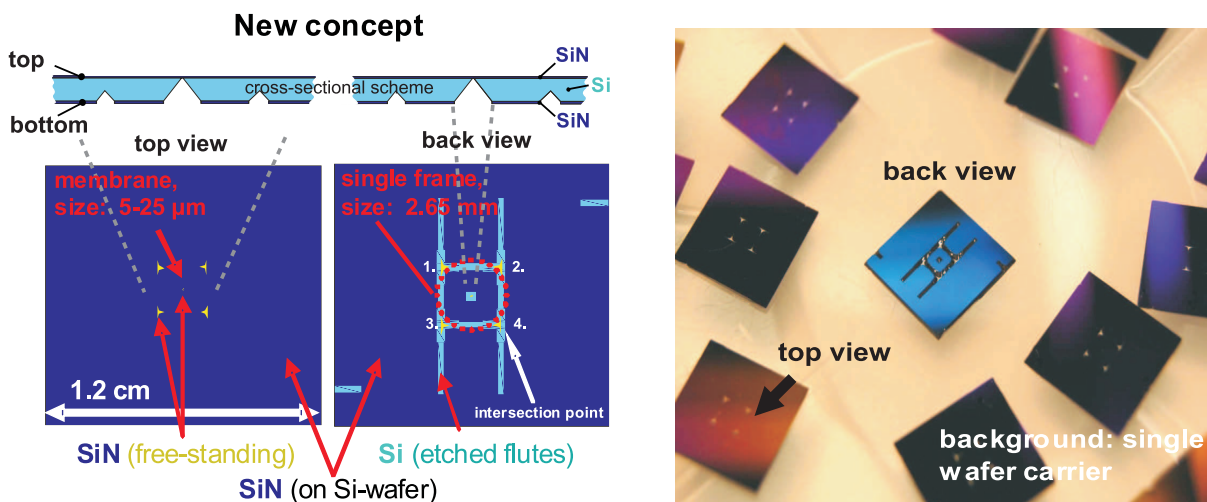


Fig. 6: Left: Drawing of the top and back view of the advanced single frame chip design including a scheme of its cross-sectional area. Right: A photograph of self-fabricated support chips exhibiting specified SiN membrane sizes of around 25 μm .

Similar as for the commercially available chips, the free-standing SiN areas are achieved by using highly anisotropic wet-chemical etching (KOH solution) of unmasked (100) Si surfaces. Simultaneously etched flutes — which include automatically achieved freestanding SiN “triangles” at the four intersection points (numbered in Fig. 6) — enable simple cleaving to remove the surrounding chip areas from the central single frame after sample preparation is finished.

Large, unstructured chip areas around the single frame provide optimum conditions for

resist coating in terms of lithographic applications and the avoidance of accidental cracking into several single or double-frame chips upon contact with a lithography mask or removal of the sample from conductive carbon pads, which are typically used for SEM/FIB sample mounting.

A similarly important benefit of the mechanically stable surrounding areas is the possibility of etching marker structures into the SiN layer to enable the precise sample alignment that is required for subsequent e-beam-writing processes.

After the support chip fabrication itself, electrode structures were deposited onto the SiN membrane (Fig. 7, left). The metal layer system consists of 10 nm titanium, 30 nm gold and again of approximately 100 nm titanium. The top layer is used to protect the gold layer from a tetrafluoromethane plasma introduced by the reactive-ion etching (RIE) machine. Latter is needed to realize precisely a vertical slit in-between the electrodes, in terms of using the electrode structure itself as mask (self-alignment). After the dry etching process the upper titanium layer becomes selectively removed, together with a temporary photoresist mask used to protect the exposed SiN surface around the electrodes (Fig. 7, right).

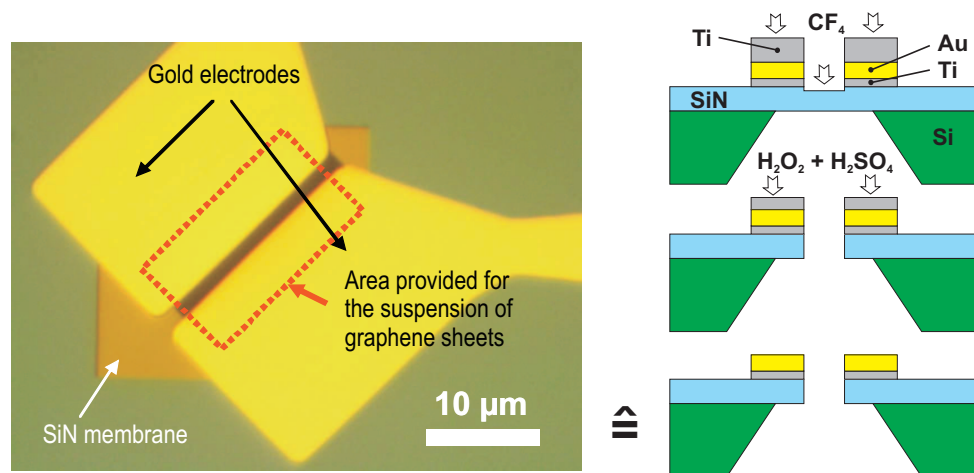


Fig. 7: Left: Optical micrograph of an advanced support geometry. Right: Schematic illustration of the layer system and fabrication steps to achieve such an electrode support structure

The main advantage of this electrode design is that the sample is actually suspended only between the two electrodes and not interacting with any support material. In other words we achieved optimum conditions to perform highly sensitive electrical measurements, especially with regard to the influence of adsorbate-induced surface states on conductivity.

3. Conclusion

We introduced three different approaches to fabricate in a most efficient way and according to individual demands a sample platform which is fully capable to perform in situ electrical measurements on a HRTEM. The first two methods are based on commercially available TEM support chips and hence they represent the cheapest and fastest way. The third

and most promising possibility is an alternative to gain the optimum of flexibility with respect to the further processing and possible applications.

Acknowledgments

Special thanks go to Jannik Meyer and Gerardo Algara-Siller from the Electron Microscopy Group of Materials Science and to Joachim Kusterer from the Institute of Electron Devices and Circuits for his great support with respect to the Si and SiN related processing.

References

- [1] F. Schedin, A.K. Geim, S.V. Morozov, E.W. Hill, P. Blake, M.I. Katsnelson, and K.S. Novoselov, “detection of individual gas molecules adsorbed on graphene”, *Nature Materials*, vol. 6, pp. 652–655, 2007.
- [2] X. Jia, M. Hofmann, V. Meunier, B.G. Sumpter, J. CamposDelgado, J. Manuel RomoHerrera, H. Son, Y. Hsieh, A. Reina, J. Kong, M. Terrones, M.S. Dresselhaus, “Controlled formation of sharp zigzag and armchair edges in graphitic nanoribbons”, *Science*, vol. 323, no. 25, pp. 1701–1705, 2009
- [3] J.Y. Hiang, F. Ding, B.I. Yakobson, P. Lu, L. Qi., and J. Li, “In situ observation of graphene sublimation and multi-layer edge reconstruction”, *PNAS*, vol. 106, no. 25, pp. 10103–10108, 2009

Coaxial GaN/InGaN/GaN Nano-Heterostructures

Mohamed Fikry

The optimization of the epitaxial quality and ordering of coaxial GaN/InGaN/GaN nano-heterostructures is the main focus of this study. Two approaches for the realization of upright ZnO nanopillars, used as templates for the epitaxially grown GaN layers, with their respective degrees of pattern arrangement are introduced. Consequently, the growth of coaxial GaN/InGaN/GaN quantum wells (for three different samples) along with the corresponding structural and optical properties is investigated. By comparing the optimized InGaN quantum well growth conditions in two different MOCVD reactors, we could reduce the FWHM of an intense room temperature photoluminescence peak of the InGaN quantum well at 3 eV from 300 meV to 190 meV. Cathodoluminescence mapping along the nanotubes revealed two main peaks that are emerging from the sides and top facets of the tubes backing an argument for different respective In incorporation.

1. Introduction

Gallium nitride nanotubes and nanorods have been receiving considerable attention as building blocks for nanophotonic technologies due to their unique high aspect ratios, promising the realization of photonic and biological nanodevices such as blue light emitting diodes (LEDs), short-wavelength ultraviolet nanolasers and nanofluidic biochemical sensors [1]. As a first step to realize the potential impact of these novel structures, the development of a process for fabricating dislocation free, position and diameter controlled nanostructures arrays is necessary. A variety of techniques have been utilized to synthesize GaN nanowires including laser ablation [2], metal-initiated Vapor-Liquid-Solid nanowire growth in metalorganic chemical vapor deposition (MOCVD) reactors [3] as well as hydride vapor phase epitaxy [4]. However, these approaches suffered from not having well ordered and upright pillars. On the other hand, there have been various methods to successfully grow high quality, upright and arranged ZnO nanorods [5]. Therefore, one approach for realizing GaN nano-structures in an upright and well ordered form is growing GaN epitaxially around ZnO nanorods as reported in our previous work [6].

ZnO decomposes by reacting with hydrogen or ammonia at elevated temperatures. Therefore, a multi-layer growth process (MGP) for the growth of GaN layers on ZnO templates by Metal Organic Vapor Phase Epitaxy (MOVPE) [7] has been developed. However, at the very last stage of growth at high temperatures, the ZnO may easily dissolve resulting in GaN nanotubes taking the original pattern of the ZnO pillars (Fig. 1). Furthermore, we have demonstrated the growth of a coaxial GaInN quantum well structure around the resulting GaN nanotubes [8]. In the present study, we investigated further the optimization of the afore-mentioned coaxial quantum well growth along with the corresponding

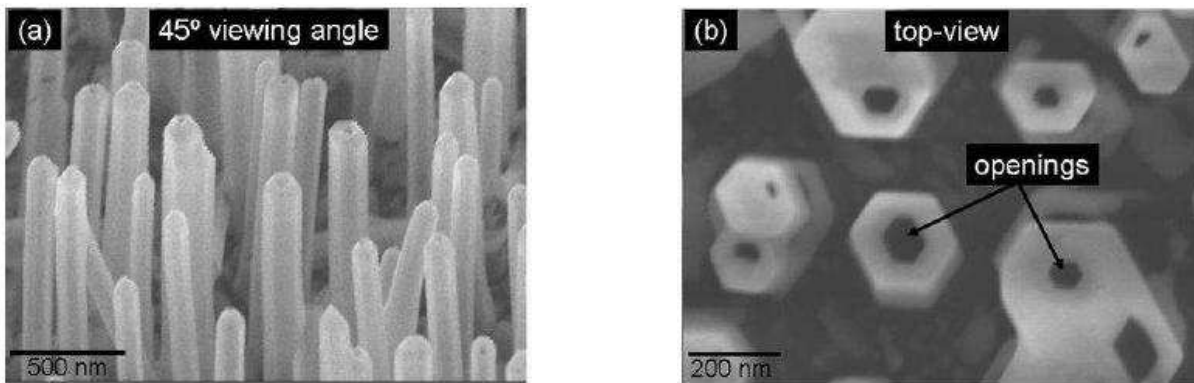


Fig. 1: GaN nanotubes grown around ZnO nanorods which dissolved during the MOVPE process [6].

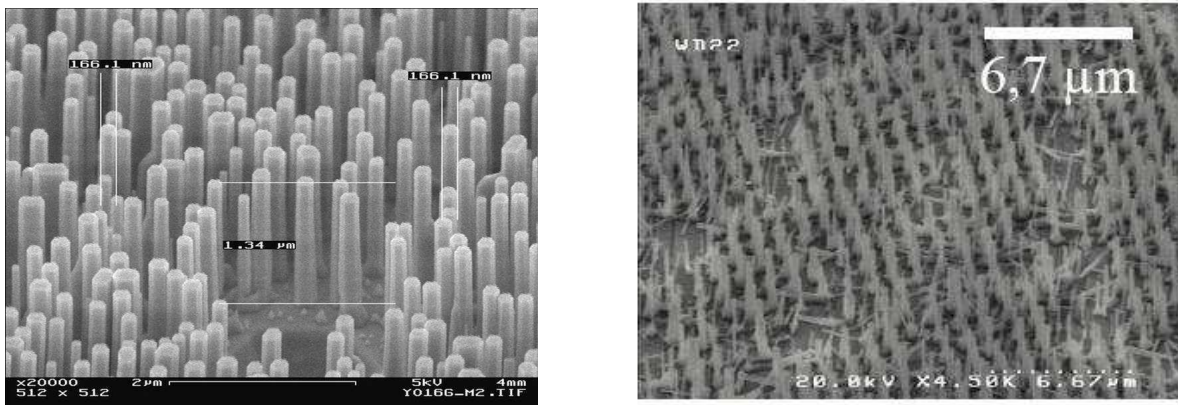


Fig. 2: ZnO nanorods grown on a-plane sapphire using a ZnO seed layer (left) [9] and using a gold catalyst (right) [10].

optical and structural characterizations using photoluminescence, transmission electron microscopy, scanning electron microscopy and cathodoluminescence. In addition, a new approach for the control of the arrangement and diameter of the ZnO pillar templates is described accompanied by the corresponding optical characterization of the overgrown coaxial GaN/InGaN/GaN heterostructures.

2. Experimental

The ZnO nanopillars used as templates in these studies have been grown using two different approaches. The first is a catalyst-free vapor-solid process on a-plane sapphire wafers which started with a ZnO nanocrystal nucleation seed layer using zinc acetate as precursor [9]. In a subsequent step, the nanorods were deposited at 845 °C with Ar as carrier gas where a ZnO/carbon powder was used as a precursor. Vertically aligned ZnO nanorods (Fig. 2 left) with typical diameters and heights of 100–300 nm and 1–2 μm were achieved, respectively.

However, this is a random process where the precise control of the position or ordering

of the rods is not controllable and the degree of reproducibility of such process is not quite high. Therefore, a second approach utilizing the structured patterning of a thin metal catalyst layer on the a-plane sapphire substrate before the ZnO pillar growth was attempted [10]. Around 2 nm of Au were deposited on the a-plane sapphire followed by the deposition of a monolayer of polystyrene spheres with a diameter of 1.4 μm . Then the sample is treated on a hot plate and in an oxygen plasma for fixing the spheres on the gold film and reducing their size, respectively. Finally, the gold film in the open windows between the spheres is wet etched and the spheres are removed in an ultrasonic bath. The final pattern of the gold catalyst takes the form of the Polystyrene sphere monolayer, where the periodic distance is dictated by the diameter of the spheres, the time in oxygen plasma and the wet etching time of the gold film. The ZnO pillar growth is thus enhanced mainly at the sites where the gold catalyst is positioned. A SEM picture of the subsequently grown ZnO pillars in an ordered form on the patterned gold catalyst is shown in Fig. 2 (right) with diameters of 100–300 nm and lengths of 1–1.5 μm , respectively. The ZnO templates are then transferred to our AIXTRON AIX 200 RF low pressure (LP) MOVPE system. Here, the precursors were trimethylgallium (TMGa) and NH_3 . In the following, we compare three different samples. For sample A, the ZnO pillars were grown using the catalyst-free nucleation seed layer. The subsequent GaN nanotube growth and the In containing layers including the adjacent GaN barrier layer took place in two different MOVPE systems, respectively, in order to take advantage of the well established InGaN growth environment in the second system. A single coaxial quantum well was epitaxially grown. We have already reported about the characterization results for this sample in [8]. It is retrieved here for comparison.

For sample B, the sequence was exactly the same except for the facts that three coaxial quantum wells were grown and there was no growth interruption. InGaN growth took place in the same MOVPE system after the InGaN growth conditions have been optimized. Finally, sample C was a gold patterned ZnO template with the same GaN and InGaN growth conditions as sample B.

Photoluminescence carried out at room and low temperature was applied to investigate the band gaps of the grown multi-layer nano-structures. The shape of the grown nanopillars was mainly investigated by scanning electron microscopy (SEM). Transmission electron microscopy (TEM) measurements revealing the dimensions of single rods and the heterostructure details for sample A are retrieved [8]. Low temperature cathodoluminescence was utilized to map the distribution of quantum wells for sample B.

3. Coaxial GaInN Quantum Wells

As mentioned above for sample A, the deposition of one InGaN quantum well took place in a second MOVPE system. Here, the growth was re-established by growing a thin GaN layer (about 7 nm) at 885 $^\circ\text{C}$ with triethylgallium (TEGa) as Ga precursor and N_2 as carrier gas. Then, the trimethylindium (TMIn) flow was switched to the reactor to grow a GaInN quantum well with nominally about 10 % In at a temperature of 830 $^\circ\text{C}$. Finally, the temperature was set back to 885 $^\circ\text{C}$ for the growth of the outer GaN barrier layer, first grown with N_2 as carrier gas, then switching to H_2 for the last few nanometers. SEM

inspection showed that the diameters of the nanotubes have significantly increased and the tube openings were closed (Fig. 3 left).

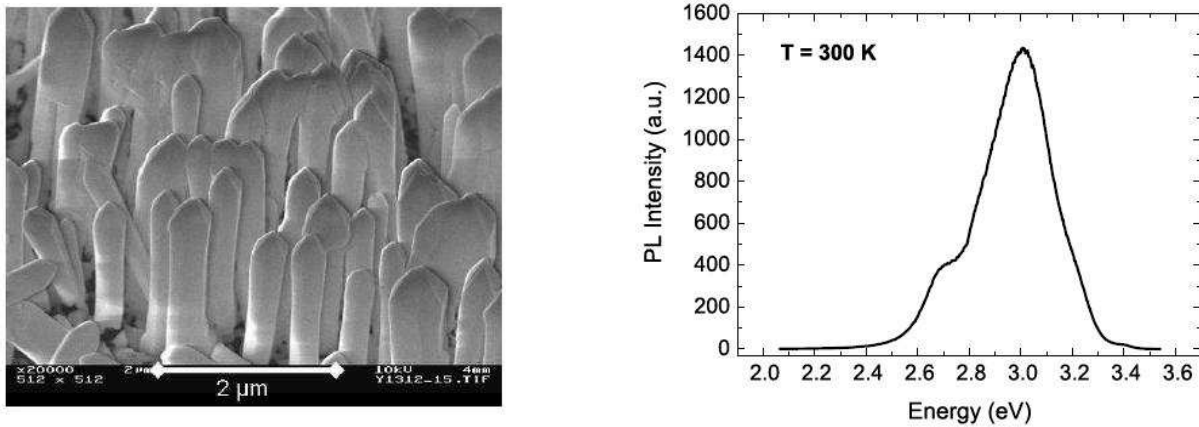


Fig. 3: Sample A: GaInN/GaN coaxial nanotube structures (left) and the corresponding room temperature photoluminescence spectrum (right) [8].

It seems that most material was deposited at the top of the tubes, indicating a less pronounced precursor diffusion down to the template surface. This may be a consequence of the fairly densely packed nanotubes and of the lower diffusivity of TMI_n and TEGa as compared to TMGa, being even further pronounced by the lower growth temperature. In room temperature photoluminescence, a fairly intense peak at around 3 eV, the position expected for the GaInN quantum well, was observed (Fig. 3 right) with a full width at half maximum of 300 meV. TEM analysis (not shown here) showed a quantum well thickness of 4 nm, a covering spacer of 20 nm and a distance of 40 nm from the inner tube wall to the quantum well layer [8].

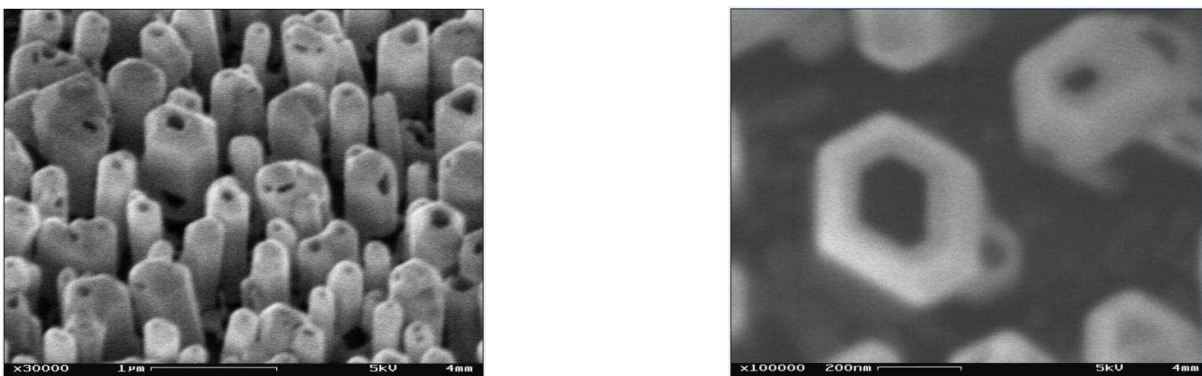


Fig. 4: Sample B: three GaN/GaInN/GaN coaxial nanotube heterostructures grown without growth interruption.

For sample B, three quantum wells were deposited directly after the epitaxial growth of the GaN tube in the same machine. Here, the InGa_n quantum wells growth conditions were optimized for a barrier and quantum well thicknesses of 7 nm and 3 nm on *c*-plane sapphire, respectively, with an emission wavelength of 417 nm. Within that context, the barrier and

quantum well growth temperatures were 880 °C and 860 °C, respectively, using the same precursors and carrier gas as for sample A. As opposed to sample A, the tube openings were apparently observed (Fig. 4). This could indicate the process sensitivity with respect to the diffusivity of TMIn and TEGa to the temperature variations between the two machines. In room temperature photoluminescence, an intense peak with a narrower spectral width of 190 meV was observed at 3.086 eV indicating again the existence of a quantum well structure (Fig. 5 (left)). Note that the light-colored lines are just software created Gaussian fits for calculation purposes.

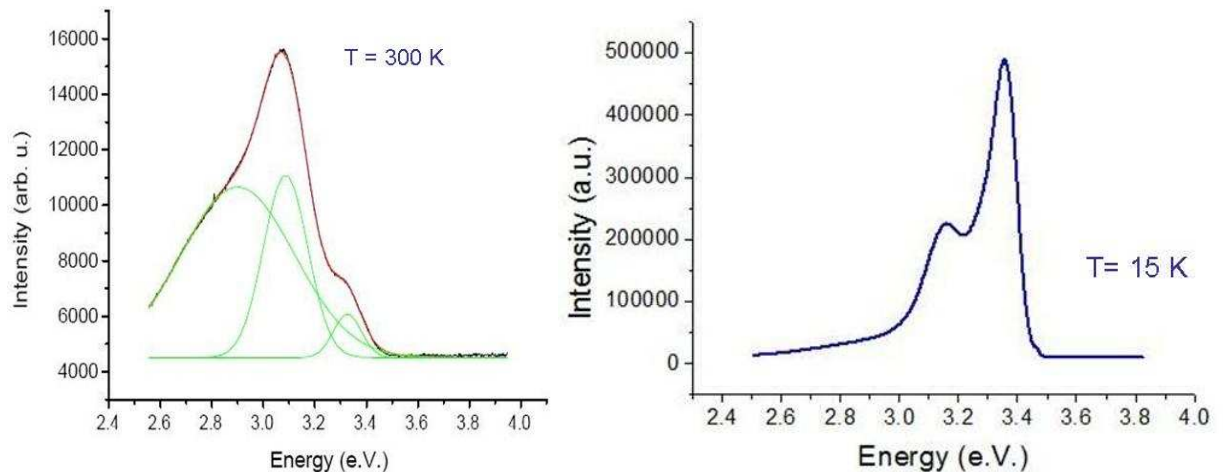


Fig. 5: Sample B: Room temperature and low temperature photoluminescence spectrum for three GaN/GaInN/GaN coaxial nanotube heterostructures.

Moreover, a wide blue luminescence peak - also noticeable for sample A - centered around 2.8 eV is observed, which has been reported by Wang et al. to be attributed to carbon incorporation from the TMGa incomplete dissociation at low temperatures during the deposition of the first layers of GaN [11]. Another shoulder peak at 3.33 eV was observed that could be attributed to either band gap emission of some remaining ZnO or a possible stacking fault in GaN or even some InGaN layers with less In incorporation along different facets of the GaN nanotube (namely: the side walls or the top ring of the tube). In low temperature photoluminescence (Fig. 5 right), the intensity of the InGaN quantum well peak was shifted to 3.16 eV and was increased by a factor of 2.5 with the same spectral width of 190 meV. The peak at 3.33 eV was increased by a factor of 5 whereas the blue luminescence peak was suppressed. Furthermore, low temperature cathodoluminescence mapping along the rods has been undergone (Fig. 6 and Fig. 7). It was shown that the emission of the lower energy peak that is attributed to the InGaN quantum well mainly emerged from the top of the tubes (Fig. 6), whereas the higher energy peak emission emerged from sides and bottom of the tubes (Fig. 7). Five minutes hydrochloric acid (HCL) treatment was undergone to a twin sample to etch away any remaining ZnO, however the spectrum did not show a significant decrease of the peak at 3.33 eV, thus supporting more the assumption of a stacking fault or a an InGaN phase separation on the different facets of the tubes.

The ZnO pillars of sample C were less dense and more ordered than those of samples

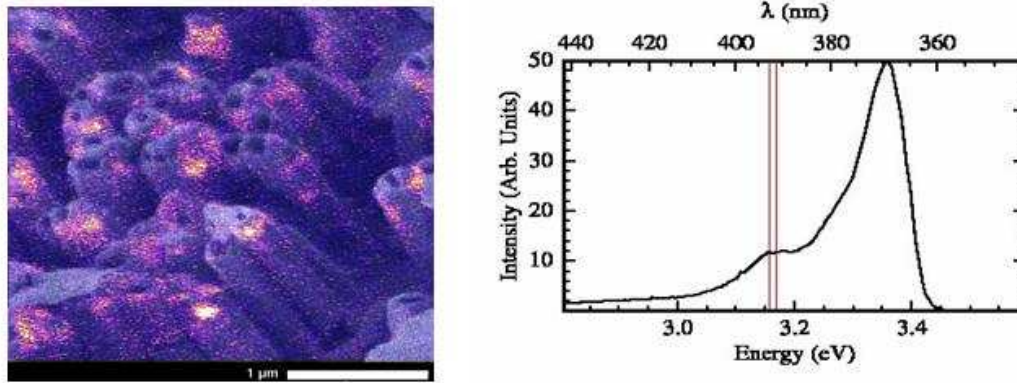


Fig. 6: Low temperature cathodoluminescence mapping along the nano-tubes for sample B under detector window centered at 393 nm.

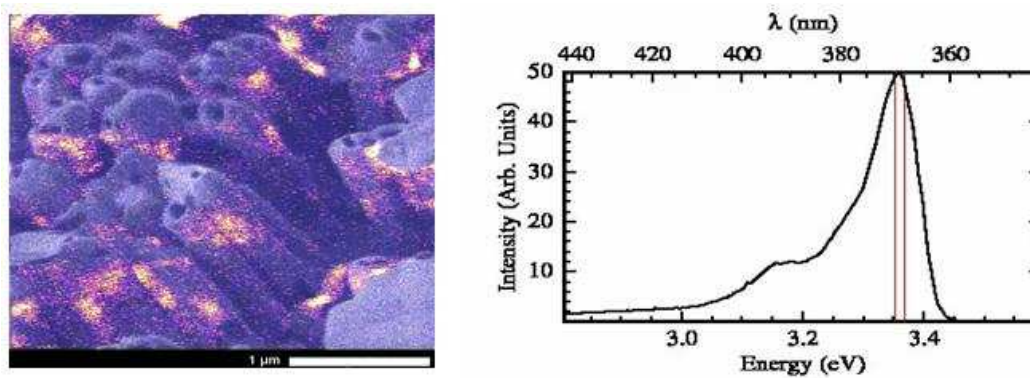


Fig. 7: Low temperature cathodoluminescence mapping along the nano-tubes for sample B under detector window centered at 370 nm.

A and B since the approach of the structured patterning of the gold film mentioned in the experimental section has been utilized. The InGa_N quantum well growth conditions were exactly the same as those for sample B. As shown in Fig. 8 (left), the GaN tubes with their coaxial quantum wells took the same arrangement as the original ZnO pillars. However, the diameters of tube openings were considerably reduced (Fig. 8 (right)). In low temperature photoluminescence (Fig. 9), a sharp peak showing the donor bound exciton emission of GaN at 3.46 eV with spectral width of 14 meV was observed. This is in addition to a newly observed peak at 3.41 eV that is assumed to be stacking fault of GaN, blue luminescence and the afore-mentioned unclarified peak around 3.33 eV.

Surprisingly, the InGa_N quantum well peak at 3.16 eV, previously discussed for sample B, did not show any sign in the spectrum. Probably, the TmIn and TEGa diffusion on a lower density of pillars is more homogeneously distributed along the rods leading to lower In incorporation on the top ring facets of the tubes, thus reducing the emission of the afore-mentioned InGa_N peak. However, still CL and TEM of that sample are needed for confirmation of the afore-mentioned argument. Notably, the wide blue luminescence at low temperature for sample C is considerably high compared to sample B that could indicate a possible manifestation of gradient of In incorporation.

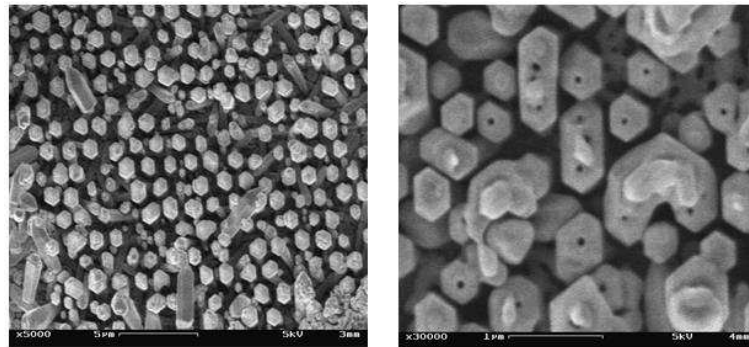


Fig. 8: Sample C: SEM pictures of the coaxial GaN/InGaN/GaN nano-heterostructures showing a relatively ordered pattern (left) and a smaller tube opening diameter compared to sample B (right).

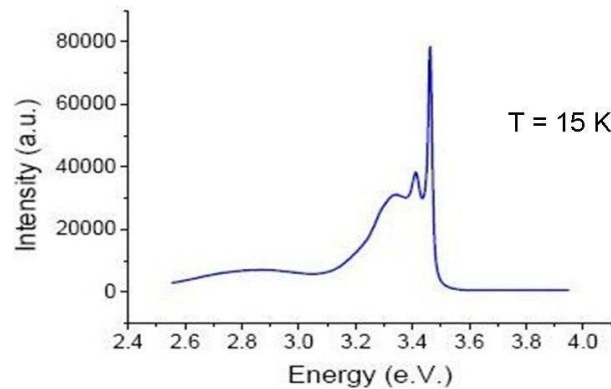


Fig. 9: Low temperature photoluminescence for sample C: coaxial GaN/InGaN/GaN quantum wells overgrown around a less dense and more ordered ZnO pillar template.

4. Conclusion

Based on cathodoluminescence mapping along the coaxial GaN /InGaN/GaN nanoheterostructures, we assume that the In incorporation along the nanotubes is different along the sides and the top ring facets, respectively. Moreover, low temperature photoluminescence for the more ordered and less dense structures revealed the disappearance of an InGaN peak at 3.16 eV and the appearance of a more intense and wide blue luminescence peak. This could indicate that for the more ordered structures, a gradient of In incorporation along different facets exists which would be attributed to higher diffusivity of TMIn and TEGa.

5. Acknowledgments

A very special thanks to Dipl. Physik. Manfred Madel for the growth of all the ZnO pillar templates and his scientific support with his experience in the field. Similarly, a great appreciation for the following persons: Dipl. Physik. Kim Fujan for the CL measurements, M.Sc. Yong Xie, Dr. Martin Feneberg, Prof. Klaus Thonke, Sarad B. Thapa and Prof. Ferdinand Scholz.

References

- [1] Y. Huang, X. Duan, Y. Cui, and C.M. Lieber, “Gallium nitride nanowire nanodevices”, *Nano Lett.*, vol. 2, pp. 101–104, 2002.
- [2] X. Duan, Y. Cui, and C.M. Lieber, “Laser-assisted catalytic growth of single crystal GaN nanowires”, *Journal of the American Physical Society*, vol. 122, no. 1, pp. 188–189, 2000.
- [3] T. Kuykendall, P. Pauzauskie, S. Lee, Y. Zhang, J. Goldberger, and P. Yang, “Metalorganic chemical vapor deposition route to GaN nanowires with triangular cross sections”, *Nano Lett.*, vol. 3, no. 8, pp. 1063–1066, 2003.
- [4] H. Kim, T. Kang, and K. Chung, “Nanoscale ultraviolet-light-emitting diodes using wide-bandgap gallium nitride nanorods”, *Adv. Mater.*, vol. 15, pp. 567–569, 2003.
- [5] J.Y. Park, Y.S. Yun, Y.S. Hong, H. Oh, J.J. Kim, and S.S. Kim, “Synthesis, electrical and photoresponse properties of vertically well-aligned and epitaxial ZnO nanorods on GaN-buffered sapphire substrates”, *Appl. Phys. Lett.* 87, p. 123108, 2003.
- [6] S.B. Thapa, J. Hertkorn, T. Wunderer, F. Lipski, F. Scholz, A. Reiser, Y. Xie, M. Feneberg, K. Thonke, R. Sauer, M. Durrschnabel, L.D. Yao, D. Gerthsen, H. Hochmuth, M. Lorenz, and M. Grundmann, “MOVPE growth of GaN around ZnO nanopillars”, *J. Crystal Growth*, vol. 310, pp. 5139–5142, 2008.
- [7] E. Angelopoulos, *Heteroepitaxial Growth of GaN on ZnO by MOVPE*, Master Thesis, Ulm University, 2007.
- [8] F. Scholz, S.B. Thapa, M. Fikry, J. Hertkorn, T. Wunderer, F. Lipski, A. Reiser, Y. Xie, M. Feneberg, K. Thonke, R. Sauer, M. Durrschnabel, L.D. Yao, and D. Gerthsen, “Epitaxial growth of coaxial GaInN-GaN hetero-nanotubes”, *IOP Conf. Ser.: Mater. Sci. Eng.* 6, p. 12002, 2009.
- [9] A. Reiser, V. Raeesi, G.M. Prinz, M. Schirra, M. Feneberg, U. Röder, R. Sauer, and K. Thonke, “Growth of high-quality, uniform c-axis-oriented zinc oxide nano-wires on a-plane sapphire substrate with zinc oxide templates”, *Microelectronics Journal*, vol. 40, no. 2, pp. 306–308, 2007.
- [10] M. Madel, *ZnO-Nanostruktur-Wachstum auf Substraten mit Kolloid-Vorstrukturierung*, Diploma thesis, Ulm University, 2009.
- [11] G.T. Wang, A.A. Talin, D.J. Werder, J.R. Creighton, E. Lai, R.J. Anderson, and I. Arslan, “Highly aligned, template-free growth and characterization of vertical GaN nanowires on sapphire by metalorganic chemical vapour deposition”, *Nanotechnology* 17, pp. 5773–5780, 2006.

Processing of Semipolar and Nonpolar InGaN Based Laser Diodes

Robert A.R. Leute

We studied a fabrication process suitable for laser diodes based on both nonpolar and semipolar AlGaInN structures. The simplicity of the designated device architecture of an oxide stripe laser is well suited as a test structure. We investigate the crucial process of resonator formation for nonpolar material and describe the response of nonpolar material to dry etching.

1. Introduction

Laser diodes (LDs) based on InGaN quantum well (QW) structures emitting in the blue to green spectral region are of great interest for applications ranging from spectroscopy to laser projectors for mobile devices. Whereas LDs in the blue spectral region are available commercially, the so-called “green gap” is just at the point of being bridged. The necessity of creating InGaN QWs with high indium content in order to achieve longer wavelengths leads to an aggravation of epitaxial challenges. Optimal growth conditions for the active region become increasingly different from the surrounding GaN layers with increasing In content. Furthermore, the lattice mismatch between GaN and InGaN induces strong polarization fields along the commonly used polar directions, thus resulting in a reduced recombination rate, due to the quantum confined Stark effect (QCSE). The QCSE draws the wave functions of electrons and holes apart, thereby decreasing the wave function overlap. This inherent issue can be avoided or alleviated by the growth of the active region on nonpolar or semipolar planes [1].

There is no consensus nor clear scientific indication about the most opportune crystal plane yet. The longest wavelengths (520-531 nm) have been achieved on the semipolar $\{20\bar{2}1\}$ plane [2,3] while LDs on the conventional c-plane have been pushed as far as 515 nm [4, 5]. The essential issues of increasing the indium incorporation and reducing defect densities are still unsolved. Additionally, differently oriented samples pose new challenges for device processing, too. Especially the alignment of laser mirrors in respect to crystal planes is drastically changed when growing devices with alternate crystal orientations. We investigate the subsequent material response in respect of differences between polar and nonpolar samples.

1.1 Fabrication process for an oxide-stripe laser

There are numerous device architectures for laser diodes. Aim of our investigations is the application of an oxide stripe laser diode fabrication process on nonpolar and semipolar

samples. The edge emitting design of an oxide-stripe laser is well established and was already applied successfully to conventional c-plane samples, producing a laser diode with a threshold current density of 6 kA/cm^2 [6]. Fig. 1 shows the LD schematically.

Vertical optical confinement is achieved by sandwiching the active layer between two AlGaN layers with lower refractive indices. Laterally, the current injection along a small opening in the insulating oxide layer pumps just a narrow region leading to gain guiding. Lateral optical confinement is achieved by isolating the top metal contact from the laser structure except for a small stripe opening.

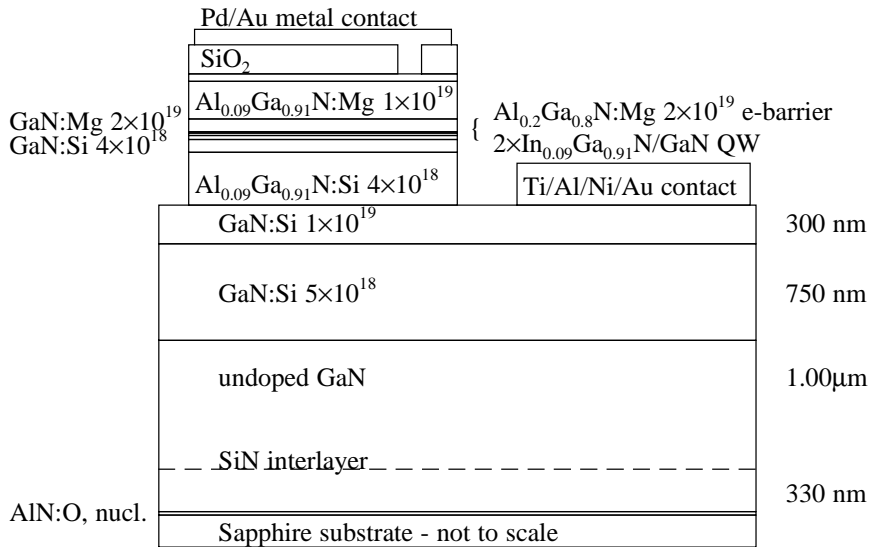


Fig. 1: Epitaxial structure and layout of laser device.

2. Experimental

The processing steps were investigated using test samples that were *not* laser structures. The efficiency of the laser diodes is reliant on the reflectivity and orientation of the resonator mirrors. Conventional LDs based on polar AlInGaN samples have typically resonator facets formed by m and a oriented crystal planes. Thus they are well aligned and very smooth. For homoepitaxially grown samples (e.g. [3]) as well as samples grown on SiC this can be achieved by cleaving. For heteroepitaxial growth on sapphire, the crystal orientation between substrate and the grown layers is rotated and cleaving of the substrate will not result in equally cleft layers.

Therefore etching is used for resonator formation. In order to get steep and smooth sidewalls, we need both an etching mask material with high selectivity as well as an etching method with high anisotropy. The former is fulfilled by nickel (cf. [7]). For the latter, solely dry etching methods such as reactive ion etching (RIE) are utilized. Especially the possibility to balance physical and chemical etching gives control of the etching profile in contrast to wet etching. The high anisotropy is especially needed for

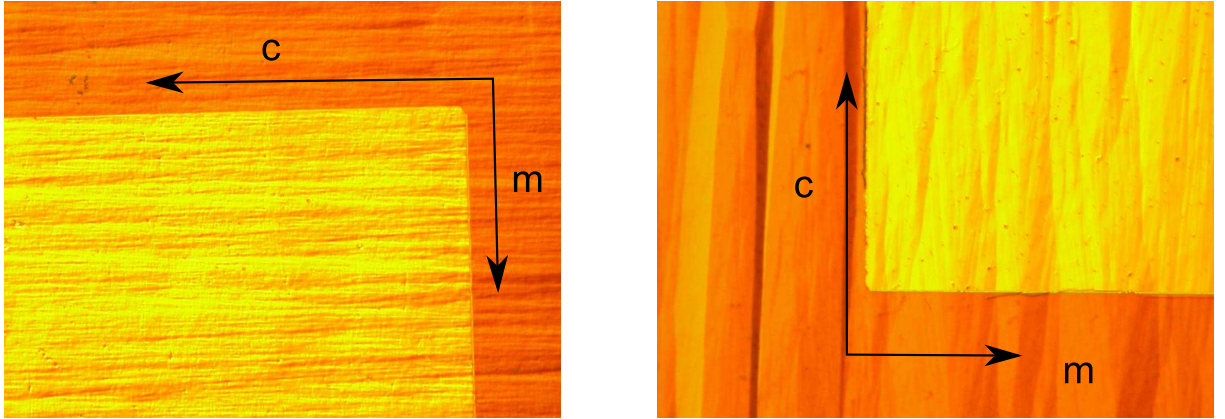


Fig. 2: Optical microscope image (200 \times) of Ni mask aligned along c-axis for HVPE (left) and MOVPE (right) grown samples.

semipolar samples where aspired resonator facets no longer coincide with low index crystal facets.

The alignment of the resonators has great influence on the gain of the diode, especially for semipolar and nonpolar samples. Scheibenzuber et al. [8] calculated gain and optical eigenmodes in InGaN laser diodes and found substantially higher gain values for laser ridges oriented parallel to the c-axis (or its projection) compared to an orientation perpendicular to it. Thus, it is necessary to fabricate resonators along the c-axis. Resonator sidewalls will then be formed by c-planes and m-planes for a-plane oriented samples. As mentioned before, prospective samples will be grown heteroepitaxially on sapphire substrates and thence will be unsuited to create mirrors by means of cleaving.

For testing, two samples were prepared. The first sample S9456aGSr consists of $\approx 5.46 \mu\text{m}$ nominally undoped a-plane oriented GaN grown by MOVPE. The second sample V9081_7 consists of a MOVPE grown a-plane oriented GaN template, overgrown inside a hydride vapor phase epitaxy (HVPE) reactor creating an approximately $20 \mu\text{m}$ thick a-plane oriented nominally undoped GaN layer. Both samples were grown on r-plane sapphire and show typical grooves (cf. [9]) along c-direction. 300 nm nickel was evaporated as etch-

Table 1: RIE conditions used for dry etching of a-plane GaN.

Electrode RF power	50W
Pressure	15 mTorr
Cl ₂	1.7 sccm
BCl ₃	10.2 sccm
Ar	5.1 sccm
Etch rate	$\approx 40 \text{ nm/min}$

mask using 15 nm titanium as an adhesion layer. A mesa pattern was transferred by photolithography. The alignment of the stripes along the c-direction can be seen in Fig. 2. Under the optical microscope, the grooves and the overall roughness are clearly visible.

For a-plane samples, the resonator edges are aligned parallel to $\{0001\}$ and $\{10\bar{1}0\}$ crystal planes, we therefore expect smooth and steep sidewalls. On both samples mesa structures were etched with an Oxford Plasmalab 100 RIE system using the parameters given in table 1. The parameters were chosen from previous experiences with c-plane samples [6] where sidewalls with an inclination angle of 80° were achieved.

After dry etching the mask was removed with a wet etching solution of H_2O , HCl and H_2O_2 . The samples were then investigated with a scanning electron microscope (SEM).

3. Results

The aforementioned roughness of heteroepitaxially grown nonpolar samples complicated the deposition of the nickel etch mask. The 300 nm thick Ni layer is highly strained and even with a Ti adhesion layer, the reduced contact to the GaN surface lead to flaking and self separation of the mask from the sample. In order to improve adhesion and reduce the strain, we increased the thickness of the Ti layer from 15 nm to 20 nm and introduced two 1 nm thick gold interlayers each after 100 nm of nickel for strain relaxation. Thusly evaporated etch masks showed flawless adhesion and allowed smooth structuring. The etch time (RIE) was chosen for an etching depth of approximately $1.2\ \mu\text{m}$ based on previous experiences with c-plane GaN. We found no noticeable difference in etch rate for the a-plane samples. Figure 3 shows the SEM picture of a mesa flank of the HVPE grown sample with included height measurement. The etching depth of the MOVPE grown sample was found to be the same within the accuracy of the measurement (not shown). Both samples show a humpy roughening of the upper half of the flank but are smooth below (Fig. 5). Whether these bulges are related to material properties or caused by the processing is unclear, yet.

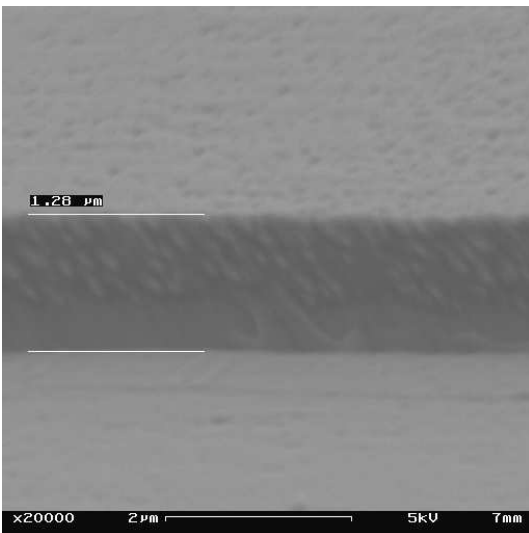


Fig. 3: SEM picture of mesa side flank (HVPE sample), height $\approx (1.2 \pm 0.1)\ \mu\text{m}$.

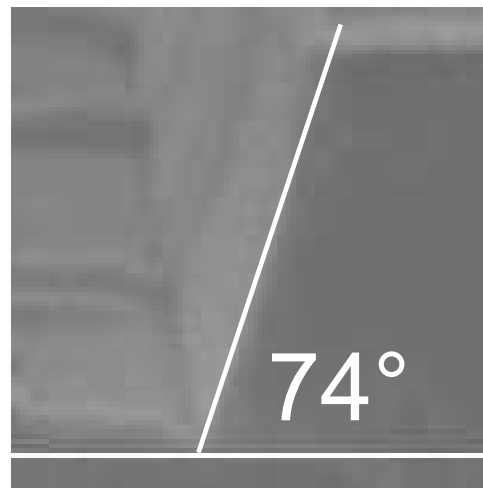


Fig. 4: SEM picture (detail) of cleft mesa, considering the viewpoint the inclination angle is $\approx (74 \pm 2)^\circ$ (MOVPE sample).

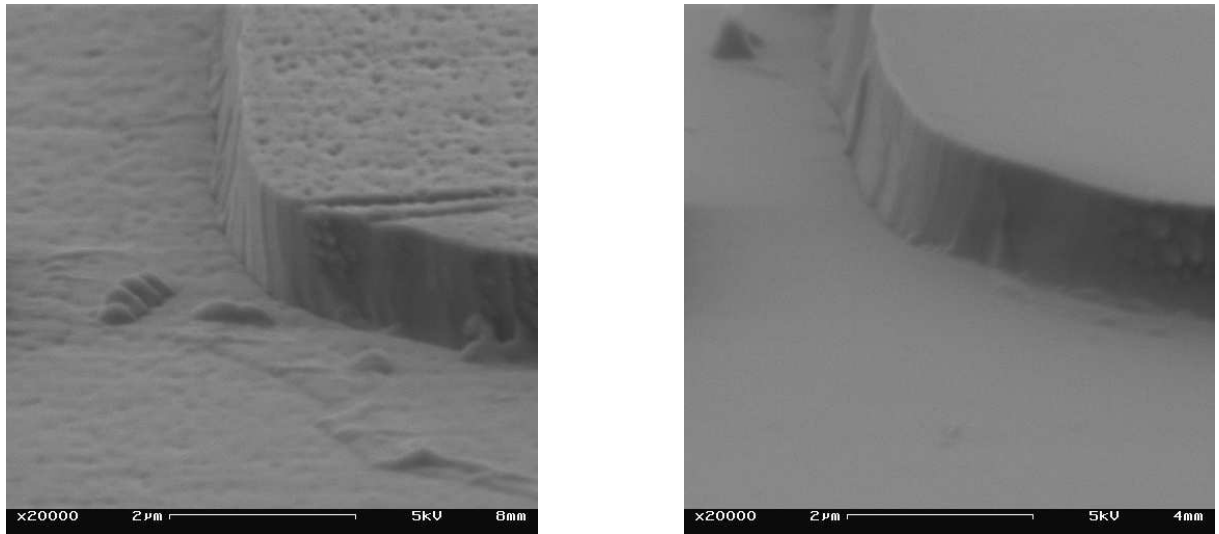


Fig. 5: SEM images of the mesa edge for HVPE (left) and MOVPE (right) grown a-plane GaN after removal of the Ni mask.

Measurement on a mesa cleft (Fig. 4) shows an inclination of only 72° to 75° . Further optimization of the anisotropy of the etching process deems necessary, before they can be used as resonator mirrors.

The etching seemed to have only marginally deleterious effects on the etched surface. They still show a typical respective smoothness for HVPE and MOVPE grown a-plane GaN (Fig. 6) and hence appear well suited for further processing steps.

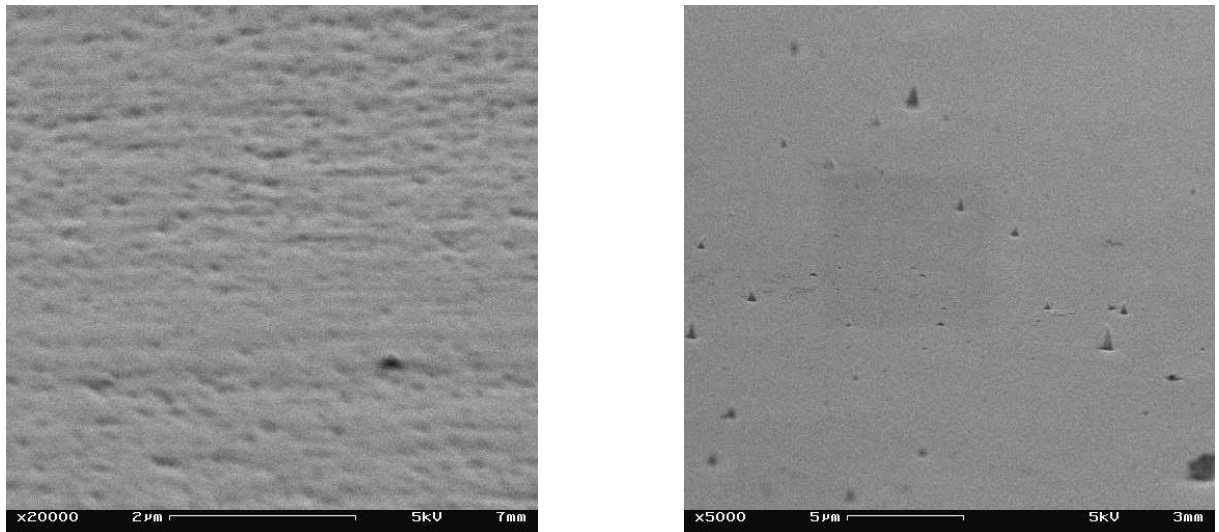


Fig. 6: SEM images of etched surface for HVPE (left) and MOVPE (right) grown a-plane GaN.

4. Conclusion & Outlook

The response of nonpolar GaN to RIE dry etching was investigated. The etching mask was optimized by introducing gold interlayers for a high reproducibility and reliability. While

etching depth and profile are very promising further investigations for a-plane samples are needed to increase the inclination angle of the etched resonator mirrors as well as further experiments on samples with semipolar surfaces.

Acknowledgments

Much valued technical support was given by Ilona Argut, Rudolf Rösch and Rainer Blood.

References

- [1] P. Waltereit, O. Brandt, A. Trampert, H.T. Grahn, J. Menniger, M. Ramsteiner, M. Reiche, and K.H. Ploog, “Nitride semiconductors free of electrostatic fields for efficient white light-emitting diodes”, *Nature*, vol. 406, pp. 865–868, 2000.
- [2] Y. Enya, Y. Yoshizumi, T. Kyono, K. Akita, M. Ueno, M. Adachi, T. Sumitomo, S. Tokuyama, T. Ikegami, K. Katayama and T. Nakamura, “531 nm green lasing of InGa_N based laser diodes on semi-polar {20 $\bar{2}$ 1} free-standing GaN substrates”, *Appl. Phys. Express*, vol. 2, p. 082101, 2009.
- [3] Y. Yoshizumi, M. Adachi, Y. Enya, T. Kyono, S. Tokuyama, T. Sumitomo, K. Akita, T. Ikegami, M. Ueno, K. Katayama, and T. Nakamura, “continuous-wave operation of 520 nm green InGa_N-based laser diodes on semi-polar {20 $\bar{2}$ 1} GaN substrates”, *Appl. Phys. Express*, vol. 2, p. 092101, 2009.
- [4] T. Miyoshi, S. Masui, T. Okada, T. Yanamoto, T. Kozaki, S. Nagahama, and T. Mukai, “510–515 nm InGa_N-based green laser diodes on c-plane GaN substrate”, *Appl. Phys. Express*, vol. 2, p. 062201, 2009.
- [5] A. Avramescu, T. Lerner, J. Müller, S. Tautz, D. Queren, S. Lutgen, and U. Strauss, “InGa_N laser diodes with 50 mW output power emitting at 515 nm”, *Appl. Phys. Lett.*, vol. 95, p. 071103, 2009.
- [6] M. Fikry, *Epitaxy and Processing of AlGaInN Heterostructures for Light Emitting Diode Applications*, Master Thesis, Ulm University, Ulm, Germany, 2008.
- [7] S.A. Smith, C.A. Wolden, M.D. Bremser, A.D. Hanser, R.F. Davis, and W.V. Lampert, “High rate and selective etching of GaN, AlGa_N, and AlN using an inductively coupled plasma”, *Appl. Phys. Lett.*, vol. 71, pp. 3631–3633, 1997.
- [8] W.G. Scheibenzuber, U.T. Schwarz, R.G. Veprek, B. Witzigmann and A. Hangleiter, “Calculation of optical eigenmodes and gain in semipolar and nonpolar InGa_N/Ga_N laser diodes”, *Phys. Rev. B*, vol. 80, p. 115320, 2009.
- [9] T. Detchprohm, M. Zhu, Y. Li, Y. Xia, L. Liu, D. Hanser, C. Wetzel, “Growth and characterization of green GaIn_N-based light emitting diodes on free-standing non-polar GaN templates”, *J. Crystal Growth*, vol. 311, pp. 2937–2941, 2009.

MOVPE Growth of High Quality AlGa_N Using In-Situ Deposited Si_N Nano-Masks

Kamran Forghani [†]

Growth optimization of AlGa_N epilayers — with 20% and 30% Al content — directly grown on sapphire by MOVPE was investigated. Quality of the AlGa_N epilayers was improved by an in-situ nano-masking employing ultra-thin Si_N interlayer(s), confirmed by high intensity luminescence of quantum wells grown on top of these high quality AlGa_N layers.

1. Introduction

AlGa_N layers grown directly on sapphire typically experience fairly strong biaxial compressive strain [1] which leads to a large number of threading dislocations (TDs) — mainly misfit TDs. These mainly occur in the form of edge/mixed type TDs. They cause very broad asymmetric high resolution X-ray diffraction (HRXRD) reflections, e.g. (102)-reflexes [2]. On the other hand, screw/mixed type dislocations are mainly responsible for the broadening of the symmetric (002) HRXRD peaks. They do not hamper the device performance as strongly as edge type TDs [3]. Therefore, our main interest in this work is to grow AlGa_N epilayers with as narrow as possible asymmetric XRD reflections corresponding to a low density of edge type TDs.

Nowadays, epitaxial lateral overgrowth (ELO) [4] techniques are widely used to grow high quality Ga_N layers using metalorganic vapor phase epitaxy (MOVPE). On the other hand, long *ex-situ* masking procedure and the presence of localized TDs in the window regions are typical drawbacks of ELO. Moreover, a thick overgrowth of the mask necessary to coalesce wing areas can lead to cracking of epilayers.

In-situ ELO techniques, especially in small scales, are of general interest due to the possibility to overcome the drawbacks of ELO while keeping its advantages. It has been shown by Tanaka *et al* [5] that Si_N intermediate layers are an effective tool to grow high quality Ga_N epilayers. However, Engl *et al.* [6] observed that Si_N interlayers do not reveal any visible improvement in crystal quality of AlGa_N layers. In other words, these techniques seem to be less promising concerning the AlGa_N material system, since AlGa_N does not grow as selective as Ga_N [7]. Nevertheless, we report a successful implementation of Si_N interlayers being deposited *in-situ* which could lead to facet-initiated ELO (FIELO) [8] in the nano-scale (nano-FIELO).

[†]in cooperation with M. Klein, F. Lipski, S. Schwaiger, J. Hertkorn, F. Scholz (Institute of Optoelectronics, Ulm University), M. Feneberg, B. Neuschl, K. Thonke, R. A. R. Leute, K. Fujan, I. Tischer (Institute of Quantum Matter, Ulm University), O. Klein, U. Kaiser (Transmission Electron Microscopy Group, Ulm University)

2. Experimental

All samples investigated in this study were grown on (0001) sapphire substrates in a low-pressure horizontal reactor (Aixtron AIX-200/4 RF-S). Trimethylgallium (TMGa) and trimethylaluminum (TMAI) were used as group-III precursors, and ammonia as group-V precursor. The Al incorporation in our samples was typically about 20 % and 30 % as confirmed by photoluminescence (PL) and HRXRD. The standard growth temperature was set to 1120 °C. Similar as for our high quality GaN layers, we used a nucleation layer (NL) of oxygen doped AlN with a thickness of about 25 nm [9]. Silane was used for the deposition of the SiN layers.

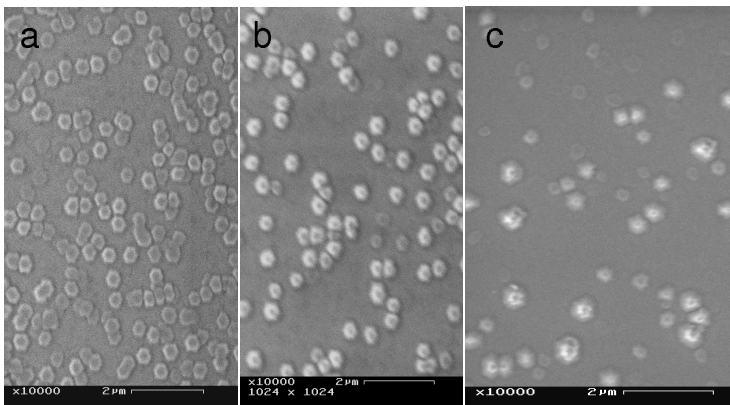


Fig. 1: 4 min AlGaN overgrowth on SiN mask with different deposition time leading to different surface morphologies with micro-islands: SiN deposition for (a) 3 min, (b) 4 min and (c) 6 min.

The thickness of the SiN interlayer must be less than a monolayer to obtain the best growth results [5]. An important factor in implementing an in-situ mask is the surface coverage, varied by the deposition time (Fig. 1).

In order to find the optimal coverage of the SiN mask, we deposited the mask after almost 150 nm of AlGaN growth on the NL and grew nominally 1 μm above the mask. Also the effect of overgrowth thickness on the crystal quality has been investigated. A series of GaN-AlGaN multi quantum wells were grown on samples with different SiN modifications, taking their CL signal as a figure of merit in order to investigate the influence of the AlGaN layer improvements obtained by the SiN interlayers on device-relevant structures. These experiments were carried out similarly for samples with 20 % and 30 % aluminium.

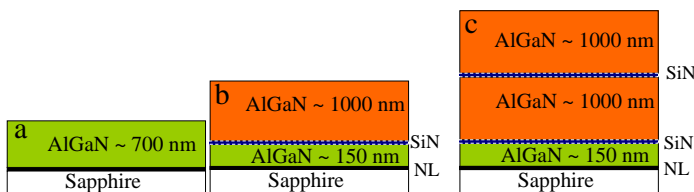


Fig. 2: Typical structures grown in this work, (a) reference sample, (b) layers with a single SiN interlayer and (c) a structure with double-SiN interlayer

As a reference for the following investigations, an AlGaN epilayer with 20 % Al content was grown with a thickness of 0.7 μm (Fig. 2-a). The X-ray rocking curves (XRC) showed a very narrow symmetric (002) reflection — FWHM of 57'' — and a very broad (102) asymmetric reflection — FWHM of 2350''. The reference sample with 30 % Al-content had a thickness of 0.6 μm showing 53'' and 2590'' XRC peak broadening for (002) and (102) reflections, respectively.

Phase-separation (inhomogeneous incorporation of Al in AlGa_N epilayers) has a high probability to occur during AlGa_N growth. The different surface migration lengths of the Ga and Al adatoms [1] play an important role in the phase-separation appearance, i.e. whenever growth occurs on an uneven surface, this phenomenon takes place more severely [10]. Since during AlGa_N post-growth of SiN, pyramidal islands are initiated, we have investigated phase-separation as side effect by means of PL followed with locally resolved cathodoluminescence (CL), shortly called SEM-CL.

3. Results and Discussion

3.1 AlGa_N layers with 20% Al

AlGa_N epilayers were grown as schematized in Fig. 2-b, with a SiN interlayer deposited after 150 nm growth of AlGa_N on a NL followed by 1 μm overgrowth of SiN.

The deposition time of the SiN-layer was varied between 3 min and 8 min. The best results within the series could be obtained for a deposition time of 6 min revealing huge crystal improvement — XRC (102)-FWHM of 571'' — due to SiN nano-masking, see table. 1. However, the more SiN coverage is, the rougher the surface, being evident from atomic force microscope (AFM) roughness evaluations in 10 μm × 10 μm. Whenever mask coverage is higher, consequently, more overgrowth thickness is essential in order to coalesce the initiated facets (submicro-islands), see Fig. 1. The surface roughness is also correlating with (002)-FWHM XRCs.

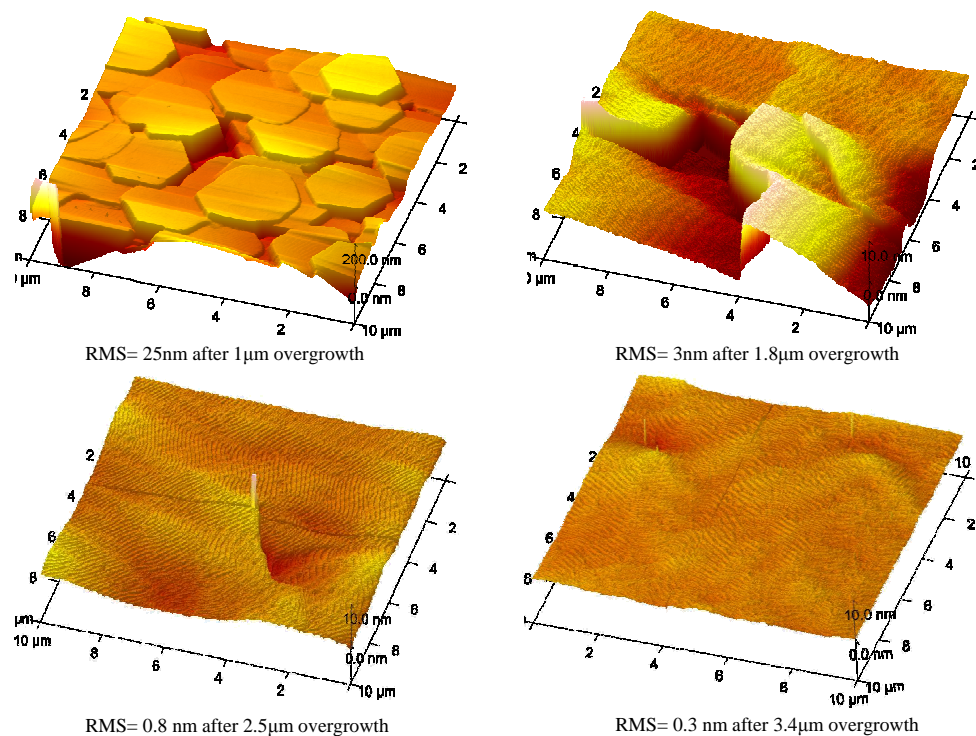
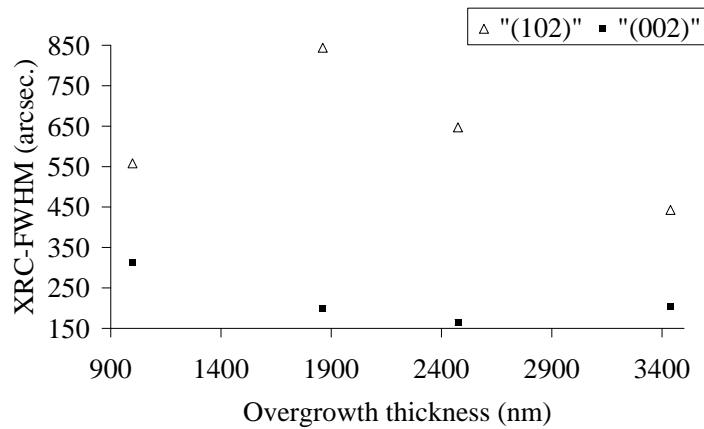


Fig. 3: Surface topography evaluations after different overgrowth of SiN mask (6 min deposited) with AlGa_N.

Table 1: Effect of SiN deposition time on XRC (102), (002) reflections and surface roughness in AFM for the samples with 20% Al.

SiN deposition	(102)-FWHM	(002)-FWHM	RMS-AFM
0 min	2347''	57''	1 nm
3:30 min	1789''	115''	2 nm
4 min	1212''	160''	6 nm
4:30 min	999''	183''	8 nm
5 min	645''	321''	15 nm
6 min	571''	343''	25 nm
7 min	645''	308''	23 nm
8 min	818''	301''	58 nm

Therefore, we carried out a series of investigations concerning the effect of overgrown layer thickness after the SiN mask on crystal quality together with evolution of surface topography. The sample with a SiN deposition time of 6 min was chosen. Fig. 3 shows the surface topography and roughness evaluations done by AFM. After 2.5 μm overgrowth, we achieved sub-nm roughness values which was even less than our reference sample with 1 nm roughness. The asymmetric peak FWHM decreased with increasing thickness down to a value of 443'' for the sample with 3.4 μm overgrowth (Fig. 4).

**Fig. 4:** Effect of SiN mask overgrowth on XRC of (102) and (002) reflections in AlGaIn (20%) epilayers — with SiN deposition time of 6 min.

A multi quantum well (MQW) structure ($8 \times \text{GaIn:}3 \text{ nm}/\text{AlGaIn:}7 \text{ nm}$) was grown on these high quality layers to take their luminescence as a probe for the improvement of the epilayer quality due to the SiN interlayer. On the reference sample (AlGaIn epilayer without SiN interlayer) the MQW-PL intensity at about 3.6 eV is weaker than that of the buffer layer — 700 nm thick AlGaIn — at about 3.85 eV with PL-FWHM of 67 meV (Fig. 5). However, MQW grown on layers with a SiN interlayer at 150 nm and 1 μm overgrowth as buffer showed much more intense PL from MQW (PL-FWHM of 58 meV) compared to that of the barrier. The PL-FWHM of the MQW even became narrower when the SiN interlayer was directly deposited on the NL.

More complicated structures like deposition of two SiN interlayers with a distance of

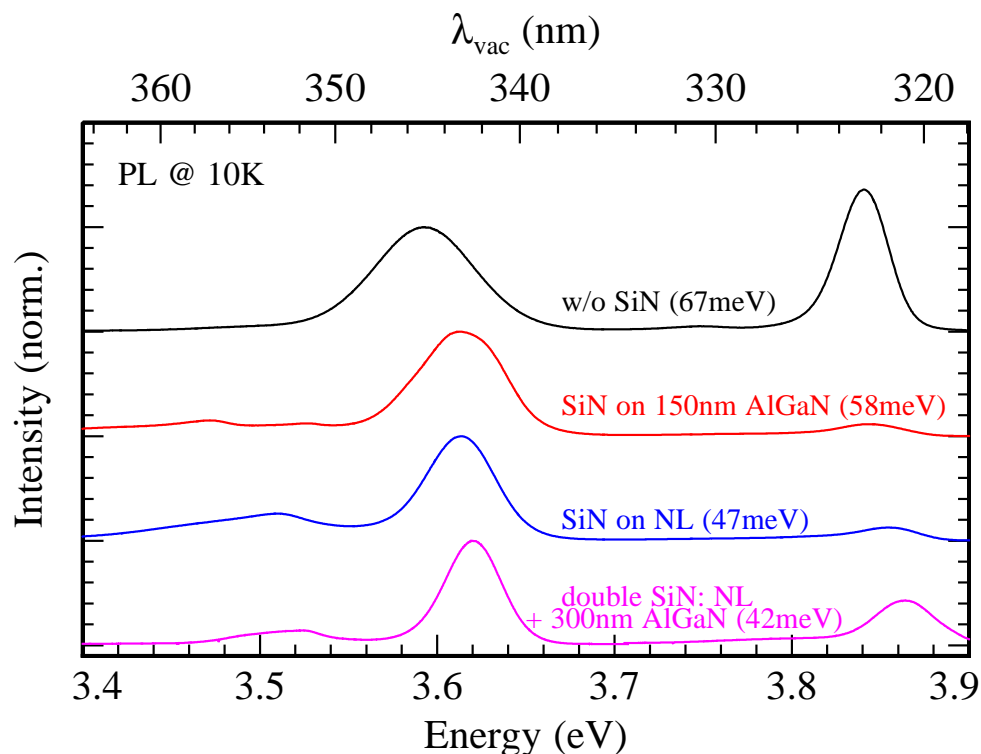


Fig. 5: Normalized PL for reference sample (without SiN interlayer) and some high quality AlGa_N layers with SiN interlayer. PL-FWHM of every layer is written on the respective graph.

300 nm — the first one on the NL — even experienced narrower luminescence spectra with a FWHM of 42 meV.

According to weak beam dark field transmission electron microscopy (WBDF-TEM) investigations, edge-type TDs (the main existing TDs) are stopped generally by the SiN interlayer (Fig. 6-a). TDs in some regions are merged or bent, creating a bundle of dislocations reaching the surface. TDs can reach the surface but in the form of a bundle of dislocations, rarely separately. Thus, this bundling increases the dislocation free surface effectively, in addition to dislocations annihilated by the SiN. Fairly large defect-free areas with diameters in the range of few micrometers in lateral size could be observed (Fig. 6-a).

We interrupted the growth after nominally overgrowing about 290 nm AlGa_N on the SiN interlayer in order to study TDs' behavior due to SiN deposition. Scanning electron microscopy (SEM) of the surface topography reveals that some pyramidal islands are formed with $\{1\bar{1}03\}$ -facets (Fig. 6-b). The islands look as if there is pure selective area grow of AlGa_N on SiN nano-mask.

TEM cross sectional images from the same sample show that growth also occurs even between the formed islands (Fig. 6-c). The AlGa_N grown on the wing area between the islands has a high density of TDs contrary to the pyramidal islands being almost TD free. The initiation of facets affect the TDs behavior as well. Due to the fact that growth in $\langle 11\bar{2}0 \rangle$ direction is faster than other in-plane directions the pyramidal islands have higher lateral growth rate. On the one hand, this leads to bending of TDs and even formation of dislocation loops, consequently dislocation termination. On the other hand, these high

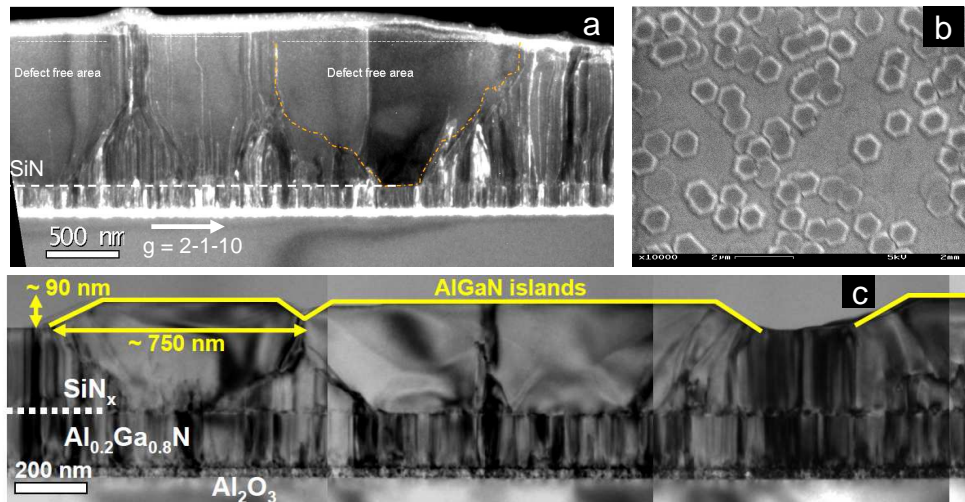


Fig. 6: (a): TEM from cross section of a sample with 4 min SiN deposited at 150 nm above NL with 1 μm overgrowth, (b): SEM image from top view of a sample with very same structure but only 4 min. overgrowth, (c): Cross sectional TEM from sample shown in (b).

quality pyramidal islands grow laterally in size and then dominate the low quality areas of AlGaN grown between them (on the wing area).

3.2 Phase separation investigations

The overgrowth of the SiN nano-mask was interrupted in order to record luminescence spectra of the topmost overgrown layers in different steps of the nano-FIELO (Fig. 7). PL spectra (Fig. 8) confirm that phase-separation phenomena occur, being evident from several visible luminescence peaks for each sample. At the very early stages of SiN-overgrowth, there are several peaks visible mainly in low Al-content regions. As the surface evolves - from sample 'i' to sample 'v' - two merging peaks are basically visible. With more overgrowth, consequently, there is just one main peak with a side peak, lower in energy as well as intensity.

In order to disclose how the Al (Ga) concentration is distributed over the surface, SEM-CL investigations were performed on the first sample within this series. The sample has 4 min AlGaN overgrown on the SiN mask deposited for 4 min.

In the CL spectrum of the sample (Fig. 9-a), several peaks are visible. The highest Al contents are incorporated on the top facets of the hillocks — c-plane facets evident from the 3.83 eV emission line (Fig. 9-e and Fig. 9-f). That is similar to findings of Zhoua *et al.* [11] that Al incorporated more into c-plane facets as compared to tilted m-plane facets. Together with the lower surface mobility of the Al-adatoms, there is another reason promoting phase segregation. Incorporation efficiency of Al and Ga adatoms depend also on crystallographic growth direction. The (001)-plane has a higher number of coordinated surface atom bonds than these tilted facets [12]. This means incorporation of adatoms on c-plane facets is energetically more favorable. In other words, Al-adatoms have stronger incorporation efficiency into c-plane facets due to lower surface diffusion length. This

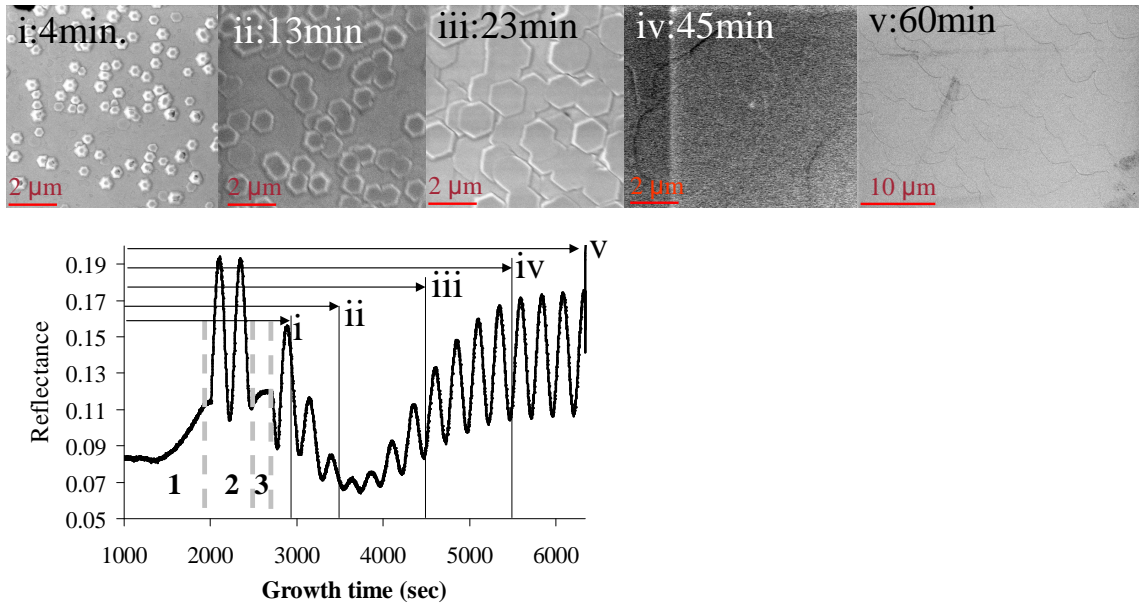


Fig. 7: Top: Surface topography of samples with different AlGaN (20%) overgrowth time after SiN deposition; ‘i’, ‘ii’, ‘iii’, ‘iv’ and ‘v’ correspond to overgrowth thickness of 90 nm, 290 nm, 510 nm, 1000 nm and 1300 nm, respectively. Bottom: respective in-situ reflectometry graphs of such samples. Steps 1, 2 and 3 show NL growth, 150 nm AlGaN growth before SiN interlayer, followed by 4 min SiN deposition, respectively.

results in a higher Al concentration on top of the hillocks and slightly less Al concentration in the side facets.

However, it is clear from SEM-CL mapping of the 3.46 eV emission line (Fig. 9-c) that pure GaN is also incorporated very much in the hillock areas. This can be attributed to the fact that in the beginning of the growth, as mentioned earlier, Ga has higher selectivity — less sticking coefficient — than Al. That results in diffusion of Ga adatoms to window area of the SiN mask at the very beginning of the AlGaN overgrowth while this is not the case for Al adatoms. Thus, it can be expected to observe GaN luminescence from the bottom layers of the hillocks. On the masked area, however, AlGaN growth is taking place (Fig. 6-c) but since it has mainly very poor crystal quality and less thickness than hillocks, it does not luminesce visibly.

3.3 AlGaN layers with 30% Al

Similar to our AlGaN (20%) layers, finding out the optimum coverage of SiN in AlGaN (30%) is our first step. Layer structures have been grown similar as described in Fig. 2-b with 1 μm overgrowth (OG) after SiN deposition. Obviously 8 min SiN-deposition time led to the best results (table 2), in the series with regard to the XRC (102)-FWHM being down to 1406'' compared to that of the reference sample with 2591''. The same MQWs as in the previous part (AlGaN layer with 20% Al) were grown on these layers. We observed a huge improvement due to the SiN implementation into such layers with a PL-FWHM of 95.9 meV while that of the sample without SiN is 212.6 meV.

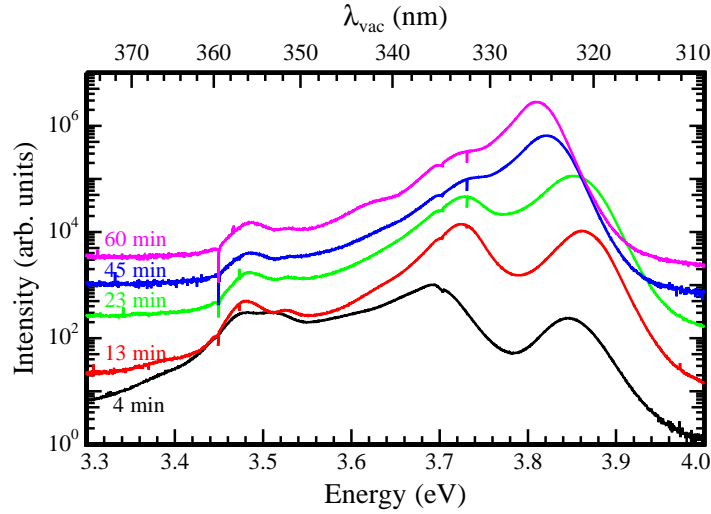


Fig. 8: PL spectra from the samples with different overgrowth times shown in Fig. 7.

Table 2: Effect of SiN-deposition time on XRD (102)- and (002)-reflections as well as on PL of MQW — emitting at 340 nm — grown on some of these buffer layers as a probe to enhancement of crystal quality in AlGaIn (30 %) layers.

Structure	SiN	(102)-FWHM	(002)-FWHM	MQW PL-FWHM
i: SiN+1 μ m OG	0 min	2591''	53''	212.6 meV
i: SiN+1 μ m OG	6 min	1814''	172''	—
i: SiN+1 μ m OG	7 min	1652''	228''	—
i: SiN+1 μ m OG	8 min	1406''	285''	95.9 meV
i: SiN+1 μ m OG	9 min	1500''	350''	—
ii: SiN+2 μ m OG	8 min	1086''	217''	88.3 meV
iii: double-SiN	8 min	1087''	233''	74.5 meV

By continuing the AlGaIn overgrowth on the SiN interlayers up to a thickness of 2 μ m, we could further reduce the edge/mixed type TDs being evident from (102)-XRC, (sample ii in table 2). The PL-FWHM of MQW is also further reduced to 88 meV. A third sample (sample: iii in table 2) was grown with the same structure but with a second SiN interlayer with distance of 1 μ m from the first SiN layer (Fig. 2-c). The second SiN did not lead to any change in the (102)-XRC peak width but revealed a slightly broader (002) reflection. Nevertheless, the MQW-PL was 13.5 meV narrower in the sample with double SiN interlayer.

4. Conclusion

In-situ deposited SiN nano-masking is an effective tool to reduce edge/mixed type dislocations in AlGaIn layers. The dislocation reduction mechanism is basically FIELO in nano scale, leading to the realization of high quality layers without necessity of thick overgrowth of the mask. As AlGaIn does not show a strong selectivity during overgrowth of SiN nano-mask, the growth occurs on the masked areas as well but the growth rate is

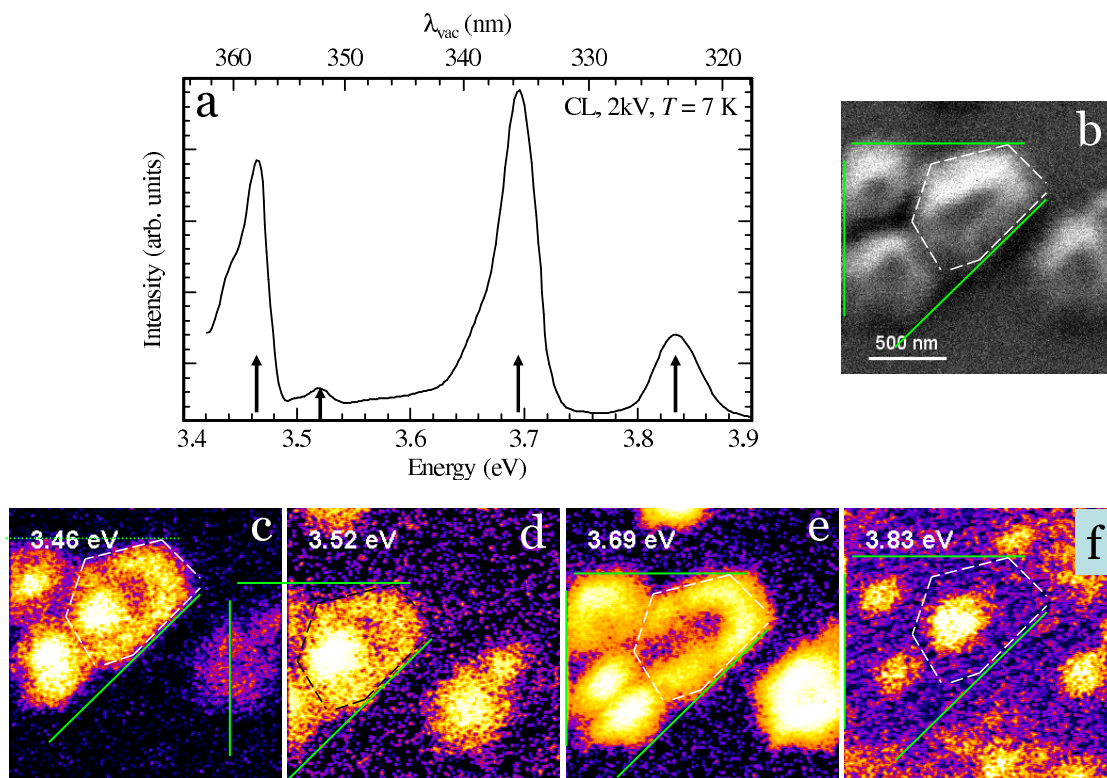


Fig. 9: SEM-CL from sample ‘i’ shown in Fig. 7. The hillocks have regions with different Al concentration distribution.

much lower than on the non-masked areas in the very beginning of the overgrowth of the mask, leading to the initiation of islands (facets) which have very low dislocation density. During the growth, they become larger eventually dominating the high dislocation density areas leading to formation of TDs’ bundle. The bundling effect additionally helps to realize larger dislocation free areas on the surface. However, this technique seems to be less efficient for higher Al concentrations, e.g. 30% Al content.

5. Acknowledgments

The TEM images provided by O. Klein and U. Kaiser from Central Facility of Electron Microscopy at Ulm University and AFM evaluations by R. Xue are gratefully acknowledged. This work was financially supported by the German Federal Ministry of Education and Research (BMBF) within the framework of the “Deep UV-LED” project.

References

- [1] M. Asif Khan, M. Shatalov, H. P. Maruska, H. M. Wang and E. Kuokstis, “III-nitride UV devices”, *Jpn. J. Appl. Phys.*, vol. 44, pp. 17191–17206, 2005.

- [2] S.B. Thapa, J. Hertkorn, F. Scholz, G.M. Prinz, R.A.R. Leute, M. Feneberg, K. Thonke, R. Sauer, O. Klein, J. Biskupek and U. Kaiser, “Growth and studies of Si-doped AlN layers”, *J. Cryst. Growth*, vol. 310, pp. 4939–4941, 2008.
- [3] T. Okimoto, M. Tsukihara, K. Kataoka, A. Kato, K. Nishino, Y. Naoi and S. Sakai, “GaN- and AlGaN-based UV-LEDs on sapphire by metal-organic chemical vapor deposition”, *phys. stat. sol. (c)*, vol. 5, pp. 3066–3068, 2008.
- [4] K. Hiramatsu, K. Nishiyama, M. Onishi, H. Mizutani, M. Narukawa, A. Motogaito, H. Miyake, Y. Iyechika and T. Maeda, “Fabrication and characterization of low defect density GaN using facet-controlled epitaxial lateral overgrowth (FACELO)”, *J. Cryst. Growth*, vol. 221, pp. 316–326, 2000.
- [5] S. Tanaka, M. Takeuchi and Y. Aoyagi, “Anti-surfactant in III-nitride epitaxy — quantum dot formation and dislocation termination—”, *Jpn. J. Appl. Phys.* vol. 39, pp. 831–834, 2000.
- [6] Y. Kato, S. Kitamura, K. Hiramatsu and N. Sawaki, “Selective growth of wurtzite GaN and AlGaN on GaN/sapphire substrates by metalorganic vapor phase epitaxy”, *J. Cryst. Growth*, vol. 144, pp. 133–140, 1994.
- [7] K. Engl, M. Beer, N. Gmeinwieser, U.T. Schwarz, J. Zweck, W. Wegscheider, S. Miller, A. Miler, H.J. Lugauer, G. Brüderl, A. Lell and V. Härle, “Process optimization for the effective reduction of threading dislocations in MOVPE grown GaN using in situ deposited SiN masks”, *J. Cryst. Growth*, vol. 289, pp. 6–13, 2006.
- [8] A. Usui, H. Sunakawa, A. Sakai and A. A. Yamaguchi, “Thick GaN epitaxial growth with low dislocation density by hydride vapor phase epitaxy”, *Jpn. J. Appl. Phys.*, vol. 36, pp. L899–L902, 1997.
- [9] J. Hertkorn, P. Brückner, S.B. Thapa, T. Wunderer, F. Scholz, M. Feneberg, K. Thonke, R. Sauer, M. Beer and J. Zweck, “Optimization of nucleation and buffer layer growth for improved GaN quality”, *J. Cryst. Growth*, vol. 308, pp. 30–36, 2007.
- [10] D.G. Zhao, D.S. Jiang, J.J. Zhu, Z.S. Liu, S.M. Zhang, H. Yang, U. Jahn and K.H. Ploog, “Al composition variations in AlGaN films grown on low- temperature GaN buffer layer by metalorganic chemical vapor deposition”, *J. Cryst. Growth*, vol. 310, pp. 5266–5269, 2008.
- [11] H. Zhoua, S. J. Chuab and C. Peng, “Al incorporation in AlGaN on $(11\bar{2}2)$ and (0001) surface orientation”, *J. Cryst. Growth*, vol. 292, pp. 5–9, 2006.
- [12] P. Ruterana, M. Albercht, J. Neugebauer, *Nitride Semiconductors: Handbook on Materials and Devices*, pp. 310–311, New York: Wiley–VCH, 2003.

Ph.D. Thesis

1. Joachim Hertkorn,
*Verbesserung der lateralen Stromführung in
hocheffizienten Halbleiterlichtquellen,*
March 2009.

Diploma and Master Theses

1. Florian Dreier,
Aufbau einer Anlage zur Herstellung integriert-optischer Wellenleiter,
Diploma Thesis, May 2009.
2. Alexander Hein,
*Optically-Pumped Semiconductor Disk Lasers with Intracavity
Second-Harmonic Generation,*
Diploma Thesis, November 2009.
3. Wenshan Pang,
Investigation on Fe Doping of GaN in Hydride Vapor Phase Epitaxy,
Master Thesis, November 2009.
4. Junjun Wang,
*Investigations of Sub-Micrometer-Sized Three-Dimensional
GaInN/GaN Structures for Light Emitting Applications,*
Master Thesis, November 2009.
5. Martin Klein,
*Untersuchungen zur metallorganischen Gasphasenepitaxie
von AlGaIn-Heterostrukturen mit hohem Al-Gehalt,*
Diploma Thesis, December 2009.

Semester Projects

1. Stefan Jäger,
Untersuchungen zur Optimierung von InGaN/GaN-Vielfach-Quantentopf-Strukturen,
March 2009.
2. Stefan Wabra,
Vergleichsmessungen zur spektralen Reflektivität und Photolumineszenz an Halbleiterscheibenlasern,
May 2009.
3. Johannes Madel,
Entwicklung und Erstellung eines Rechnerprogramms zur Simulation eindimensionaler Wellenausbreitung in Schichtstrukturen,
August 2009.
4. Andreas Strodl,
Herstellung und Charakterisierung von linear polarisierten Vertikallasern zur Verwendung in Atomuhren,
September 2009.

Talks and Conference Contributions

- [1] M. Fikry, S.B. Thapa, J. Hertkorn, T. Wunderer, F. Lipski, F. Scholz, A. Reiser, Y. Xie, M. Feneberg, K. Thonke, R. Sauer, M. Dürschnabel, L.D. Yao, and D. Gerthsen, “Epitaxial growth of coaxial GaInN-GaN hetero-nanotubes”, *EMRS Spring Meeting*, Strasbourg, France, June 2009.
- [2] M. Fikry, S.B. Thapa, J. Hertkorn, T. Wunderer, F. Lipski, F. Scholz, A. Reiser, Y. Xie, M. Feneberg, K. Thonke, R. Sauer, M. Dürschnabel, L.D. Yao, and D. Gerthsen, “Epitaxial growth of coaxial ZnO-GaN hetero-nanorods and InGaN-GaN hetero-nanotubes”, *18th European Workshop on Heterostructure Technology*, Ulm University Conference Centre Schloss Reisingburg, Günzburg, Germany, Nov. 2009.
- [3] M. Fikry, S.B. Thapa, J. Hertkorn, T. Wunderer, F. Lipski, F. Scholz, A. Reiser, Y. Xie, M. Feneberg, K. Thonke, R. Sauer, M. Dürschnabel, L.D. Yao, and D. Gerthsen, “Epitaxial growth of coaxial ZnO-GaN hetero-nanorods and InGaN-GaN hetero-nanotubes”, poster at *5th NTT-BRL school*, NTT Atsugi R & D Center, Atsugi, Kanagawa, Japan, Nov. 2009.
- [4] M. Fikry, S.B. Thapa, J. Hertkorn, T. Wunderer, F. Lipski, F. Scholz, A. Reiser, Y. Xie, M. Feneberg, K. Thonke, R. Sauer, M. Dürschnabel, L.D. Yao, and D. Gerthsen, “Epitaxial growth of coaxial ZnO-GaN hetero-nanorods and InGaN-GaN hetero-nanotubes”, *24th DGKK Workshop “Epitaxy of III/V Semiconductors”*, Berlin, Germany, Dec. 2009.
- [5] K. Forghani, F. Lipski, S. Schwaiger, J. Hertkorn, F. Scholz, M. Feneberg, R.A.R. Leute, I. Tischer, M. Wiedenmann, K. Thonke, O. Klein, and U. Kaiser, “High quality Al_{0.2}Ga_{0.8}N epilayers grown directly on sapphire without GaN buffer layer”, *European Workshop on Metalorganic Vapor Phase Epitaxy XIII*, Ulm, Germany, June 2009.
- [6] K. Forghani, M. Klein, F. Lipski, S. Schwaiger, J. Hertkorn, F. Scholz, M. Feneberg, R.A.R. Leute, K. Fujan, I. Tischer, K. Thonke, O. Klein, and U. Kaiser, “High quality Al_{0.2} Ga_{0.8}N epilayers grown directly on sapphire without GaN buffer layer”, poster at *5th NTT-BRL school*, NTT Atsugi R & D Center, Atsugi, Kanagawa, Japan, Nov. 2009.
- [7] K. Forghani, F. Lipski, M. Klein, S. Schwaiger, J. Hertkorn, F. Scholz, M. Feneberg, B. Neuschl, R.A.R. Leute, I. Tischer, M. Wiedenmann, K. Thonke, O. Klein, and U. Kaiser, “High quality AlGaN epilayers grown directly on sapphire without GaN buffer layer”, *24th DGKK Workshop “Epitaxy of III/V Semiconductors”*, Berlin, Germany, Dec. 2009.
- [8] F. Lipski, T. Wunderer, S. Schwaiger, S.B. Thapa, P. Brückner, and F. Scholz, “Free-standing GaN by hydride vapor phase epitaxy”, Seminar at Osram OS, Regensburg, Germany, Apr. 2009.

-
- [9] F. Lipski, W. Pang, T. Wunderer, S. Schwaiger, and F. Scholz, “Fe doped GaN by hydride vapor phase epitaxy using solid iron as source”, poster at *8th International Conference on Nitride Semiconductors, ICNS-8*, Jeju Island, Korea, Oct. 2009.
- [10] F. Lipski, T. Wunderer, S. Schwaiger, and F. Scholz, “Fabrication of freestanding 2”-GaN wafers by hydride vapour phase epitaxy and selfseparation during cooldown”, *8th International Conference on Nitride Semiconductors*, Jeju Island, Korea, Oct. 2009.
- [11] F. Lipski, W. Pang, and F. Scholz, “Fe-doping of GaN-layers by hydrid vapor phase epitaxy”, *24th DGKK Workshop “Epitaxy of III/V Semiconductors”*, Berlin, Germany, Dec. 2009
- [12] R.A.R. Leute, M. Feneberg, K. Thonke, R. Sauer, S.B. Thapa, F. Scholz, Y. Taniyasu, and M. Kasu, “High excitation photoluminescence studies on epitaxially grown AlN layers”, *DPG Spring Meeting*, Dresden, Germany, March 2009.
- [13] R.A.R. Leute, M. Feneberg, B. Neuschl, K. Thonke, M. Bickermann, and F. Scholz, “High excitation photoluminescence of AlN bulk crystals: biexcitons, exciton-exciton scattering and electron-hole-plasma”, poster at *5th NTT-BRL school*, NTT Atsugi R & D Center, Atsugi, Kanagawa, Japan, Nov. 2009.
- [14] R. Michalzik, “Miniaturized atomic clocks” (in German), Working Group *Optical Communications* within the Photonics BW Association, Stuttgart, Germany, Oct. 2009.
- [15] R. Michalzik, J.M. Ostermann, A. Al-Samaneh, D. Wahl, F. Rinaldi, and P. Debernardi, “Polarization-stable VCSELs for optical sensing and communications” (invited), *The 14th OptoElectronics and Communications Conf., OECC 2009*, Hong Kong, China, July 2009.
- [16] R. Michalzik, “Light-emitting diodes: new light on earth” (in German), Lecture, Ulmer 3-Generationen-Uni, Ulm University, Ulm, Germany, June 2009.
- [17] R. Michalzik, “Current VCSEL research in Ulm: sensing and optical data transmission” (in German), Seminar, Institut für Halbleiteroptik und Funktionelle Grenzflächen, Universität Stuttgart, Stuttgart, Germany, May 2009.
- [18] R. Michalzik, M. Stach, F. Rinaldi, and D. Wahl, “Integrated optoelectronic chips for bidirectional optical interconnection at Gbit/s data rates”, *Fifth Joint Symposium on Opto- and Microelectronic Devices and Cicuits, SODC 2009*, Beijing, China, May 2009.
- [19] R. Michalzik, “Laser diodes” (in German), Photonics BW Working Group *Optics Design and Simulation* and bayern photonics Working Group *Optics Design*, Ulm University, Ulm, Germany, March 2009.

- [20] R. Michalzik, A. Kroner, A. Bergmann, and F. Rinaldi, "VCSEL-based optical trapping for microparticle manipulation" (invited), *SPIE Photonics West 2009, Vertical-Cavity Surface-Emitting Lasers XIII*, San Jose, CA, USA, Jan. 2009.
- [21] R. Michalzik, "Laser technology from Ulm: the art of making mice" (in German), *Forum Market + Knowledge*, Industrie- und Handelskammer Ulm, Ulm, Germany, March 2008.
- [22] F. Scholz, T. Wunderer, M. Feneberg, and K. Thonke, "GaInN-based longer wavelength LEDs on semi-polar facets" (invited), *EMRS Spring Meeting*, Strasbourg, France, June 2009.
- [23] F. Scholz, "GaInN-based LED structures on semi-polar facets", Universität Stuttgart, Stuttgart, Germany, May 2009.
- [24] F. Scholz, T. Wunderer, M. Feneberg, K. Thonke, A. Chuvilin, U. Kaiser, S. Metzner, F. Bertram, and J. Christen, "GaInN-based LED structures on semi-polar crystal facets" (invited), *11th International Conference on Advanced Materials*, Rio de Janeiro, Brazil, Sept. 2009.
- [25] F. Scholz, "GaN research for optoelectronic structures at Ulm University", *Semiconductor Device Lab, SAIT, SAMSUNG*, Seoul, Korea, Oct. 2009.
- [26] F. Scholz, T. Wunderer, M. Feneberg, K. Thonke, A. Chuvilin, U. Kaiser, S. Metzner, F. Bertram, and J. Christen, "GaInN-based LED structures on selectively grown semi-polar crystal facets" (invited), *8th International Conference on Nitride Semiconductors ICNS-8*, Jeju Island, Korea, Oct. 2009.
- [27] S. Schwaiger, T. Wunderer, F. Lipski, and F. Scholz, "Growth of nonpolar a-plane GaN on r-plane sapphire via HVPE", *DPG Spring Meeting*, Dresden, Germany, March 2009.
- [28] S. Schwaiger, F. Lipski, T. Wunderer, and F. Scholz, "Growth of a-plane GaN layers on slightly misoriented r-plane sapphire substrates", poster at *European Workshop on Metalorganic Vapor Phase Epitaxy XIII*, Ulm, Germany, June 2009.
- [29] S. Schwaiger, F. Lipski, T. Wunderer, and F. Scholz, "Influence of slight misorientations of r-plane sapphire substrates on the growth of nonpolar a-plane GaN layers via HVPE", poster at *8th International Conference on Nitride Semiconductors, ICNS-8*, Jeju Island, Korea, Oct. 2009.
- [30] S. Schwaiger and F. Scholz, "Investigations on hydride vapor phase epitaxy of (semi-) nonpolar GaN", *PolarCoN summer school*, Günzburg, Germany, Sept. 2009.
- [31] S. Schwaiger, T. Wunderer, F. Lipski, and F. Scholz, "Non- and semipolar GaN research activities at the Institute of Optoelectronics", *KETI - Korea Electronics Technology Institute*, Suwon, Korea, Oct. 2009.

-
- [32] D. Wahl, A. Al-Samaneh, A. Strodl, S. Renz, and R. Michalzik, “Nah-Infrarot VCSEL zur Anwendung in miniaturisierten Atomuhren”, *Deutscher MBE-Workshop 2009*, Bochum, Germany, Oct. 2009.
- [33] T. Wunderer, F. Lipski, S. Schwaiger, F. Scholz., M. Wiedenmann, M. Feneberg, and K. Thonke, “Fabrication of high quality semipolar GaN on full 2 inch for green light emitters”, *DPG Spring Meeting*, Dresden, Germany, March 2009.
- [34] T. Wunderer, “Properties of 3D GaInN/GaN structures with semipolar surfaces”, Seminar at Osram OS, Regensburg, Germany, April 2009.
- [35] T. Wunderer, F. Lipski, S. Schwaiger, F. Scholz, M. Wiedenmann, M. Feneberg, K. Thonke, S. Metzner, F. Bertram, and J. Christen, “Fabrication of high quality semipolar GaInN/GaN on c-plane sapphire using selective area epitaxy”, poster at *European Workshop on Metalorganic Vapor Phase Epitaxie XIII*, Ulm, Germany, June 2009.
- [36] T. Wunderer, “Properties of 3D GaInN/GaN structures with semipolar surfaces”, *Seminar: Neue Materialien - Halbleiter*, Otto-von-Guericke Universität Magdeburg, Magdeburg, Germany, June 2009.
- [37] T. Wunderer, F. Scholz, M. Feneberg, K. Thonke, A. Chuvilin, U. Kaiser, S. Metzner, F. Bertram, and J. Christen, “GaInN/GaN LEDs on semipolar crystal facets”, (invited), *Workshop Nitrides*, Bremen, Germany, Sep. 2009.
- [38] T. Wunderer, J. Wang, F. Lipski, S. Schwaiger, S.S. Shirokov, A.E. Yunovich, and F. Scholz, “Color tuning using single semipolar GaInN light-emitting diode grown on 3D inverted pyramids”, *8th International Conference on Nitride Semiconductors, ICNS-8*, Jeju Island, Korea, Oct. 2009.
- [39] T. Wunderer, Y. Men, J. Wang, F. Lipski, S. Schwaiger, F. Scholz, M. Feneberg, M. Wiedenmann, and K. Thonke, “Light-matter coupling of semipolar InGaIn quantum wells grown on sub-micrometer sized 3D gratings”, poster at *8th International Conference on Nitride Semiconductors, ICNS-8*, Jeju Island, Korea, Oct. 2009.
- [40] T. Wunderer and S. Schwaiger, “Non- and semipolar GaN research activities at the Institute of Optoelectronics”, *KETI - Korea Electronics Technology Institute*, Suwon, Korea, Oct. 2009.
- [41] T. Wunderer, A. Chuvilin, Y. Men, F. Lipski, S. Schwaiger, J. Wang, E. Kohn, U. Kaiser, and F. Scholz, “Light-matter coupling of semipolar GaInN quantum wells by selective area growth of sub-micrometer sized 3D gratings”, *18th European Workshop on Heterostructure Technology*, Ulm University Conference Centre Schloss Reisingen, Günzburg, Germany, Nov. 2009.
- [42] T. Wunderer, F. Lipski, S. Schwaiger, M. Feneberg, K. Thonke, A. Chuvilin, U. Kaiser, S. Metzner, J. Christen, and F. Scholz, “Properties of selectively grown 3D GaInN/GaN LEDs with semipolar surfaces”, poster at the *5th NTT-BRL school*, NTT Atsugi R & D Center, Atsugi, Kanagawa, Japan, Nov. 2009.

- [43] T. Wunderer, “Research activities at the Institute of Optoelectronics, Ulm University, Germany”, *Kyoto University*, Kyoto, Japan, Nov. 2009.
- [44] F. Bertram, S. Metzner, J. Christen, T. Wunderer, and F. Scholz, “Carrier relaxation in semi-polar InGaN/GaN quantum wells investigated by picosecond-time resolved cathodoluminescence spectroscopy”, *SPIE Photonics West 2009, Vertical-Cavity Surface-Emitting Lasers XIII*, San Jose, CA, USA, Jan. 2009.
- [45] F. Bertram, S. Metzner, J. Christen, F. Scholz, and T. Wunderer, “Nanoscale time resolved carrier relaxation phenomena in highly efficient nitrides LED structures” (invited), *11th International Conference on Advanced Materials*, Rio de Janeiro, Brazil, Sept. 2009.
- [46] F. Bertram, S. Metzner, J. Christen, T. Wunderer, F. Lipski, S. Schwaiger, und F. Scholz, “Microscopic correlation of real structure and recombination kinetics in InGaN quantum well directly imaged using spatio-time-resolved cathodoluminescence spectroscopy”, poster at *8th International Conference on Nitride Semiconductors, ICNS-8*, Jeju Island, Korea, Oct. 2009.
- [47] N.C. Gerhardt, S. Hoevel, M. Li, H. Jaehme, M.R. Hofmann, T. Ackemann, A. Kroner, and R. Michalzick, “Ultrafast spin dynamics in spin-polarized vertical-cavity surface-emitting laser devices”, *Conf. on Lasers and Electro-Optics, CLEO 2009*, Baltimore, MD, USA, May/June 2009.
- [48] C. Karbaum, F. Bertram, S. Metzner, J. Christen, T. Wunderer, and F. Scholz, “Spectrally resolved cathodoluminescence microscopy of InGaN single quantum well on hexagonally inverted GaN pyramids”, *24th DGKK Workshop “Epitaxy of III/V Semiconductors”*, Berlin, Germany, Dec. 2009.
- [49] R. Kirste, A. Hoffmann, F. Bertram, T. Hempel, J. Christen, T. Wunderer, and F. Scholz, “Luminescence and raman spectroscopy on InGaN/GaN prism structures”, poster at *EMRS Spring Meeting*, Strasbourg, France, June 2009.
- [50] O. Klein, J. Biskupek, U. Kaiser, K. Forghani, and F. Scholz, “Simulation supported analysis of the effect of SiN_x interlayers in AlGaIn on the dislocation density reduction”, poster at *Microscopy Conference 2009*, Graz, Austria, Aug. 2009.
- [51] S. Metzner, F. Bertram, J. Christen, T. Wunderer, J. Hertkorn, F. Lipski, S. Schwaiger, and F. Scholz, “Nano-scale luminescence properties of InGaN MQWs on {1 $\bar{1}$ 01} GaN facets”, *SPIE Photonics West 2009, Vertical-Cavity Surface-Emitting Lasers XIII*, San Jose, CA, USA, Jan. 2009.
- [52] S. Metzner, F. Bertram, J. Christen, T. Wunderer, and F. Scholz, “Mikroskopische Lumineszenzuntersuchungen an grünemittierenden InGaIn/GaN MQWs auf semi-polaren 1-101 Facetten”, *DPG Spring Meeting*, Dresden, Germany, March 2009.
- [53] S. Metzner, F. Bertram, C. Hempel, J. Christen, S. Schwaiger, and F. Scholz, “Microscopic luminescence properties of a-plane GaIn MOVPE templates overgrown by HVPE”, *EMRS Spring Meeting*, Strasbourg, France, June 2009.

-
- [54] H.-J. Möstl, C. Vierheilig, U.T. Schwarz, T. Wunderer, S. Schwaiger, F. Lipski, and F. Scholz, “Characterization of photoluminescence (PL) emission from semipolar 1-101 InGaN quantum wells”, *DPG Spring Meeting*, Dresden, Germany, March 2009.
- [55] A. Molitor, M. Blazek, J.M. Ostermann, R. Michalzik, and W. Elsäßer, “Intensity noise of polarisation stabilized VCSELs”, *73rd Annual Meeting of the German Physical Society (DPG)*, Hamburg, Germany, March 2009.
- [56] U.T. Schwarz, L. Schade, F. Bertram, S. Metzner, J. Christen, T. Wunderer, and F. Scholz, “Quantitative comparison of cathodoluminescence and micro-photoluminescence spectroscopy: InGaN quantum wells grown on inverse pyramids”, poster at *8th International Conference on Nitride Semiconductors, ICNS-8*, Jeju Island, Korea, Oct. 2009.
- [57] I. Tischer, M. Schirra, M. Feneberg, R. Sauer, K. Thonke, E. Mueller, D. Gerthsen, T. Wunderer, and F. Scholz, “Defect-related cathodoluminescence features in GaN stripes with semipolar facets”, *EMRS Spring Meeting*, Strasbourg, France, June 2009.
- [58] I. Tischer, M. Schirra, M. Feneberg, R. Sauer, K. Thonke, T. Wunderer, and F. Scholz, “Defect-related cathodoluminescence in ELOG GaN structures”, *DPG Spring Meeting*, Dresden, Germany, March 2009.
- [59] M. Wiedenmann, M. Feneberg, R. Sauer, K. Thonke, T. Wunderer, S. Schwaiger, F. Lipski, and F. Scholz, “Spectral behaviour of semipolar GaInN/GaN on 11-22 and 1-101 semipolar facets”, *DPG Spring Meeting*, Dresden, Germany, March 2009.

Publications

- [1] F. Demaria, S. Lorch, S. Menzel, M.C. Riedl, F. Rinaldi, R. Rösch, and P. Unger, “Design of highly efficient high-power optically pumped semiconductor disk lasers”, *IEEE J. Select. Topics Quantum Electron.*, vol. 15, no. 3, pp. 973–977, 2009.
- [2] J. Hertkorn, S.B. Thapa, T. Wunderer, F. Scholz, Z.H. Wu, Q.Y. Wei, F.A. Ponce, M.A. Moram, C.J. Humphreys, C. Vierheilg, and U.T. Schwarz, “Highly conductive modulation doped composition graded p-AlGa_N/(AlN)/Ga_N multiheterostructures grown by metalorganic vapor phase epitaxy”, *J. Appl. Phys.*, vol. 106, pp. 013720-1–6, 2009.
- [3] R.A.R. Leute, M. Feneberg, R. Sauer, K. Thonke, S.B. Thapa, F. Scholz, Y. Taniyasu, and M. Kasu, “Photoluminescence of highly excited AlN: biexcitons and exciton-exciton scattering”, *Appl. Phys. Lett.*, vol. 95, pp. 031903-1–3, 2009.
- [4] F. Lipski, S.B. Thapa, J. Hertkorn, T. Wunderer, S. Schwaiger, F. Scholz, M. Feneberg, M. Wiedenmann, K. Thonke, H. Hochmuth, M. Lorenz, and M. Grundmann, “Studies towards freestanding Ga_N in hydride vapor phase epitaxy by in-situ etching of a sacrificial ZnO buffer layer”, *phys. stat. sol. (c)*, vol. 6, pp. (S2):S352–S355, 2009.
- [5] R. Michalzik, J.M. Ostermann, A. Al-Samaneh, D. Wahl, F. Rinaldi, and P. Debernardi, “Polarization-stable VCSELs for optical sensing and communications” (invited), in Proc. (CD ROM) *The 14th OptoElectronics and Communications Conf., OECC 2009*, paper TuC2, two pages. Hong Kong, China, July 2009.
- [6] R. Michalzik, M. Stach, F. Rinaldi, and D. Wahl, “Integrated optoelectronic chips for bidirectional optical interconnection at Gbit/s data rates”, in Proc. *Fifth Joint Symposium on Opto- and Microelectronic Devices and Circuits, SODC 2009*, pp. 132–135. Beijing, China, May 2009.
- [7] R. Michalzik, A. Kroner, A. Bergmann, and F. Rinaldi, “VCSEL-based optical trapping for microparticle manipulation” (invited), in *Vertical-Cavity Surface-Emitting Lasers XIII*, K.D. Choquette, C. Lei (Eds.), Proc. SPIE 7229, pp. 722908-1–13, 2009.
- [8] F. Scholz, S.B. Thapa, M. Fikry, J. Hertkorn, T. Wunderer, F. Lipski, A. Reiser, Y. Xie, M. Feneberg, K. Thonke, R. Sauer, M. Dürrschnabel, L.D. Yao, and D. Gerthsen, “Epitaxial growth of coaxial GaInN-GaN hetero-nanotubes”, *IOP Conf. Ser.: Mater. Sci. Eng.*, vol. 6, pp. 012002-1–4, 2009.
- [9] F. Scholz, T. Wunderer, B. Neubert, M. Feneberg, K. Thonke, “Ga_N-based light-emitting diodes on selectively grown semipolar crystal facets”, *MRS Bull.*, vol. 34, pp. 328–333, 2009.
- [10] T. Wunderer, F. Lipski, S. Schwaiger, J. Hertkorn, M. Wiedenmann, M. Feneberg, K. Thonke, and F. Scholz, “Properties of blue and green InGa_N/Ga_N quantum well emission on structured semipolar surfaces”, *Jpn. J. Appl. Phys.*, vol. 48, pp. 060201-1–3, 2009.

-
- [11] T. Wunderer, F. Lipski, J. Hertkorn, S. Schwaiger, and F. Scholz, “Fabrication of 3D InGaN/GaN structures providing semipolar GaN planes for efficient green light emission”, *phys. stat. sol. (c)*, vol. 6, pp. (S2):S490–S493, 2009.
- [12] J. Bläsing, A. Krost, J. Hertkorn, F. Scholz, L. Kirste, A. Chuvilin, and U. Kaiser, “Oxygen induced strain field homogenization in AlN nucleation layers and its impact on GaN grown by metal organic vapor phase epitaxy on sapphire: an x-ray diffraction study”, *J. Appl. Phys.*, vol. 105, pp. 033504-1–9, 2009.
- [13] P. Debernardi, A. Kroner, F. Rinaldi, and R. Michalzik, “Surface relief versus standard VCSELs: a comparison between experimental and hot-cavity model results”, *IEEE J. Select. Topics Quantum Electron.*, vol. 15, pp. 828–837, 2009.
- [14] N.C. Gerhardt, S. Hoevel, M. Li, H. Jaehme, M.R. Hofmann, T. Ackemann, A. Kroner, and R. Michalzik, “Ultrafast spin dynamics in spin-polarized vertical-cavity surface-emitting laser devices”, in *Proc. Conf. on Lasers and Electro-Optics, CLEO 2009*, paper CMRR6, two pages. Baltimore, MD, USA, May/June 2009.
- [15] R. Jabbarov, N. Musayeva, F. Scholz, T. Wunderer, A.N. Turkin, S.S. Shirokov, and A.E. Yunovich, “Preparation and optical properties of Eu^{2+} doped CaGa_2S_4 -CaS composite bicolor phosphor for white LED”, *phys. stat. sol. (a)*, vol. 206, pp. 287–292, 2009.
- [16] Q. Wei, Z. Wu, K. Sun, F.A. Ponce, J. Hertkorn, and F. Scholz, “Evidence of two-dimensional hole gas in p-type AlGaIn/GaN heterostructures”, *Appl. Phys. Express*, vol. 2, pp. 121001-1–3, 2009.
- [17] T. Malinauskas, K. Jarasiunas, M. Heuken, F. Scholz, and P. Breckner “Diffusion and recombination of degenerate carrier plasma in GaN”, *physica status solidi (c)*, vol. 6, no. S2, pp. S743–S746, 2009.



ulm university universität
uulm

Ulm University
Institute of Optoelectronics
Albert-Einstein-Allee 45
89081 Ulm | Germany